Atomic layer deposition of TiN films

Growth and electrical behavior down to sub-nanometer scale

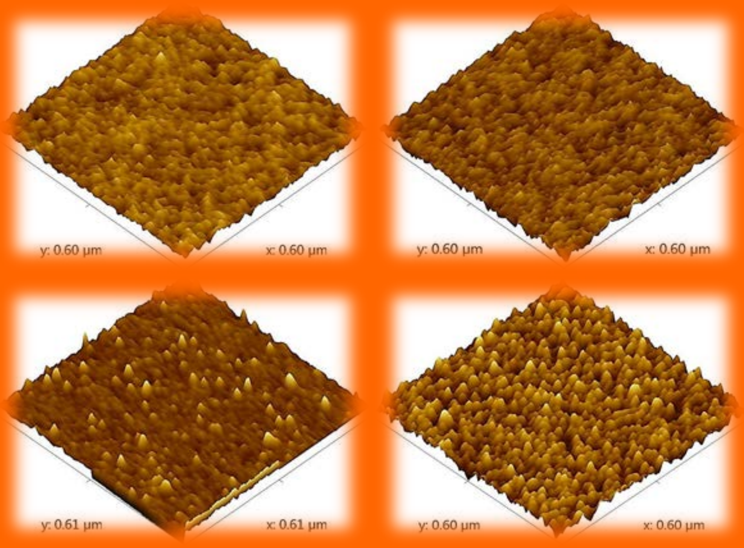

Hao Van Bui

ATOMIC LAYER DEPOSITION OF TiN FILMS

GROWTH AND ELECTRICAL BEHAVIOR DOWN TO SUB-NANOMETER SCALE

Hao Van Bui

The graduation committee:

Chairman:	prof. dr. ir. A. J. Mouthaan	University of Twente
Secretary:	prof. dr. ir. A. J. Mouthaan	University of Twente
Promoter:	prof. dr. ir. R. A. M. Wolters	University of Twente
Assistant promoter:	dr. A. Y. Kovalgin	University of Twente
Referee:	dr. ir. W. F. A. Besling	NXP Semiconductors
Members:	prof. dr. J. Schmitz	University of Twente
	prof. dr. ir. H. Hilgenkamp	University of Twente
	prof. dr. D. J. Gravesteijn	NXP Semiconductors/ University of Twente
	prof. dr. G. C. A. M. Janssen	TU Delft

This research was funded by the Dutch Technology Foundation STW, project "Conductivity control in metallic nanolayers", nr. 10017 and carried out at the Semiconductor Components group, MESA+ Institute for Nanotechnology, University of Twente, the Netherlands.

PhD. Thesis – University of Twente, Enschede, the Netherlands
Title: Atomic layer deposition of TiN films: Growth and electrical behavior down to sub-nanometer scale
ISBN: 978-90-365-3484-0
Author: Hao Van Bui
Email: haovanbui@gmail.com
DOI: 10.3990/1/9789036534840

Front cover: The images show the surface evolution of ALD TiN grown on SiO_2 observed by atomic force microscopy (Chapter 3).

ATOMIC LAYER DEPOSITION OF TiN FILMS

GROWTH AND ELECTRICAL BEHAVIOR DOWN TO SUB-NANOMETER SCALE

DISSERTATION

to obtain
the degree of doctor at the University of Twente,
on the authority of the rector magnificus,
prof. dr. H. Brinksma,
on account of the decision of the graduation committee,
to be publicly defended
on Wednesday, January 16th, 2013 at 16:45

by

Hao Van Bui

born on March 7th, 1980
in Binh Dinh province, Vietnam

This dissertation is approved by
the promoter
prof. dr. ir. R. A. M. Wolters
and the assistant promoter
dr. A. Y. Kovalgin

To my parents and parents in law,

My sisters, sisters and brothers in law,

My nieces and nephews,

My wife and my daughter.

"Có công mài sắt có ngày nên kim"

(Vietnamese proverbs, left untranslated)

Contents

1

Introduction

1.1. The project

The project “*Conductivity Control in Metallic Nanolayers*” is funded by the Dutch Technology Foundation (STW) under nr. 10017. This research brings new insights into the relation between properties of ultra-thin metallic films made by atomic layer deposition (ALD) and their possible industrial applications.

The choice of materials includes conductive thin films such as metal nitrides with the perspective of going to pure metals in future. The advantage of conductive nitrides over pure metals is (i) better established ALD processes allowing to deposit high-quality films and (ii) the presence of nitrogen as an extra tool to manipulate the electron transport properties by changing nitrogen-to-metal ratio in these materials (e.g. WN_x [1]). ALD processes of various nitrides have been well-developed [2-5] whereas ALD of pure metals is still in the early stage [6-7].

In this work, we study titanium nitride (TiN) films with the aim to investigate the growth mechanism in combination with physical and electrical properties as a function of the layer thickness. TiN is well-known for its excellent chemical, physical, mechanical and electrical properties, such as high hardness, chemical stability, high thermal conductivity and low electrical resistivity. Hence, TiN films have been widely used as protective coating layers in cutting tools. In microelectronic devices, thin continuous TiN films are commonly used as diffusion barrier and metal gate material [8-11].

In this project, the TiN film thickness ranges from the sub-nanometer range up to tens of nanometers. We further examine the films for several novel potential applications in microelectronic devices. The targeted application areas are:

> *Nano-Crystalline Non-Volatile (NCNV) memories.* –The conventional nonvolatile memories are based on a complementary metal oxide semiconductor (CMOS) structure in combination with a memory element which is commonly a continuous polycrystalline Si floating gate. To achieve nonvolatility, the tunneling oxide must be thick enough (≈7 nm) to prevent floating gate charge loss to contact regions under normal read and retention conditions. Large oxide thicknesses consequently require large voltages for the charge injection to the floating gate which leads to hot-carrier degradation [12].
>
> It has been indicated that by replacing the continuous polycrystalline silicon by discrete silicon nano-crystals, the leakage current can be reduced hence allowing thinner tunneling oxides, lower operating voltage and better performance [13-16].

In addition, nano-crystals allow low-temperature processing based on the use of CVD/ALD gate oxides with a lower quality compared to thermally grown oxide [17].

Physical Unclonable Functions (PUF). –A PUF is a function that is realized by a physical system such that the function is easy to evaluate but the system itself is difficult to characterize, model and duplicate. It was first introduced by Pappu et al [18] as a Physical One-way Function. A typical example of such a system is optical PUF which consists of a sheet of transparent material containing randomly distributed scattering particles. A laser beam directed on a sheet will produce a speckle pattern that can be recorded by an image sensor. For different sheets this pattern will be unique, unpredictable and difficult to reproduce.

An electrically based PUF consists of a set of thin film resistors. A large change in the local impedance of a percolating metallic film can be exploited for this. The local impedance can be recorded and it should change over at least two orders of magnitude for a successful device.

Field effect devices. –The field effect refers to the ability to manipulate the electrical conductivity of a material by applying an external electric field. In semiconductors, the number of carriers (i.e. electrons, and possibly holes) that can respond to the applied field is small and the field can penetrate quite far into the material. This penetration causes the redistribution of carriers and changes the conductivity of the semiconductor near the surface. However, in metals with significantly higher electron density, when an electric field is applied, it creates a surplus of induced charges which screen the penetration of the electric field into the material [19]. Therefore, to observe the field effect in metals, the applied field must be sufficiently high or the film thickness must be comparable to the penetration depth of the field. This research project focuses on the ability to manipulate the conductivity of ultra-thin metallic layers down to sub-nanometer scale.

The applications in NCNV memories require discontinuous films containing discrete islands. Percolated films are favorable for PUF applications. However, the applications in field effect devices require atomically thin continuous films because the electric field is screened at extremely short distances [20, 21]. Therefore, the deposition of the films must be highly controlled to obtain desired film morphology and properties.

Thin TiN films are conventionally deposited by chemical vapor deposition (CVD) and sputtering. However, for these methods, conformality is a concern and it is difficult to control the growth down to sub-nanometer range. Recently, ALD has emerged as a good candidate for growing ultra-thin films in a highly controlled manner. The ALD of TiN can be realized via either a thermally activated process, which is carried out at elevated temperatures, e.g. 350–550 °C, or plasma-assisted ALD, where TiN can be deposited at lower temperatures and higher growth rates can be obtained [4-5, 9, 22].

In this work, we grow ultra-thin TiN films by thermal ALD using $TiCl_4/NH_3$ chemistry. For better understanding of the growth mechanism and to further pave a way for growing pure metals (e.g. Ti, W), we equipped the ALD system with a hot-filament assisted generation of atomic hydrogen. Atomic hydrogen (H) is made by the dissociation of molecular hydrogen upon collision with a tungsten (W) filament kept at high temperatures ($T \approx 1600–1900\ ^{o}C$). Combined with ALD, this can in future result in a novel approach: Hot-filament assisted ALD. The generated atomic hydrogen can be used as a reducing agent in (metal)-ALD processes to replace the plasma-based atomic hydrogen source.

1.2. Atomic layer deposition

Atomic layer deposition is a variant of chemical vapor deposition (CVD) technique which is suitable for manufacturing thin films of various materials with thickness control at Angstrom or monolayer level [23]. In CVD, the reactants are introduced continuously and the chemical reactions may occur on the surface of the substrate or in the gas phase. ALD is based on the sequential exposure of chemical reactants which is commonly divided into four process steps forming an ALD cycle [24]: (i) exposure of the substrate to precursor A to carry out the first surface reaction (1); (ii) removal (purge) of the unused precursor and by-products of reaction (1); (iii) exposure to precursor B to carry out the second surface reaction (2); and (iv) removal of the unused precursor and by-products of reaction (2). These steps are repeated to grow the film. In ALD, the chemical reactions between the precursors occur on the surface of the substrate, reactions in the gas phase are negligible. The most important characteristic of ALD is the self-limiting surface reactions for steps (i) and (iii). Each reaction reaches saturation when all available sites on the surface have reacted with the provided precursor. The self-limiting surface reaction results in ALD’s uniformity, conformality and precise thickness control even for very high aspect ratio structures (Fig. 1.1) [25]. Therefore, ALD has emerged as an important technique for depositing thin films of different materials for various application areas [23, 26-28].

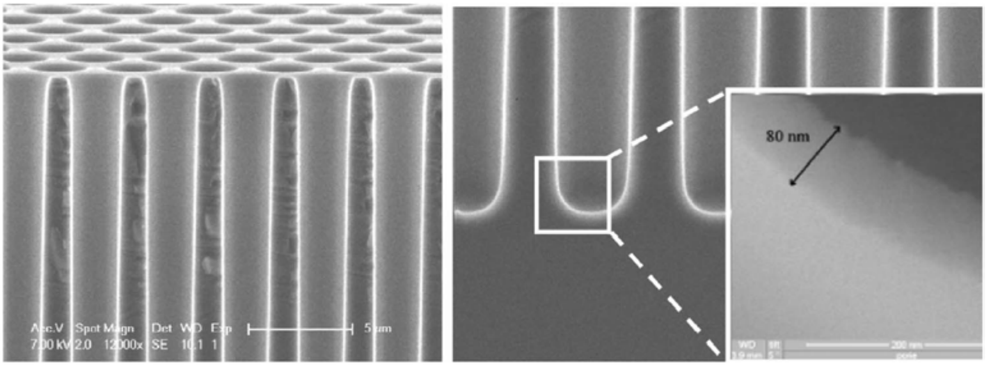

Figure 1.1. High-resolution SEM images of Al_2O_3 deposited by remote plasma ALD in macro-pore structures with an aspect ratio of 8, reprinted from Ref [25].

An example of ideal surface reactions in ALD of TiN using $TiCl_4$ (precursor *A*) and NH_3 (precursor *B*) is schematically shown in Fig. 1.2. Importantly, there must be reactive sites on the surface of the substrate that are available for chemical reactions with $TiCl_4$. In the case of SiO_2 substrate, the surface is usually covered with hydroxyl groups (–OH) which are formed due to the absorption of water during exposure to air (Fig. 1.2 (a)). The OH-surface density (coverage) plays an important role in the nucleation regime.

When $TiCl_4$ is introduced, the first half-reaction between the hydroxyl groups and the $TiCl_4$ molecules (Fig. 1.2 (b)) proceeds as

$$-OH + TiCl_4 \rightarrow -OTiCl_3 + HCl \tag{1.1-a}$$

When all of the available OH-sites have reacted, the reaction stops. HCl gas is released as the by-product and the surface termination changes from –OH to –TiCl groups. These –TiCl groups block any further reaction with $TiCl_4$. The unused $TiCl_4$ and the reaction by-product HCl are removed by the purge (Fig. 1.2 (c)).When NH_3 is introduced, the second half-reaction between –TiCl and NH_3 occurs as

$$-TiCl + NH_3 \rightarrow -TiNH_2 + HCl \tag{1.1-b}$$

This reaction forms Ti-N bonds and terminates the surface by –NH groups (Fig. 1.2 (d)). The H-termination prevents the further reaction with NH_3 and creates sites for the reaction of the next ALD cycle. The HCl by-product and the excess NH_3 precursor are then purged away (Fig. 1.2 (e)).

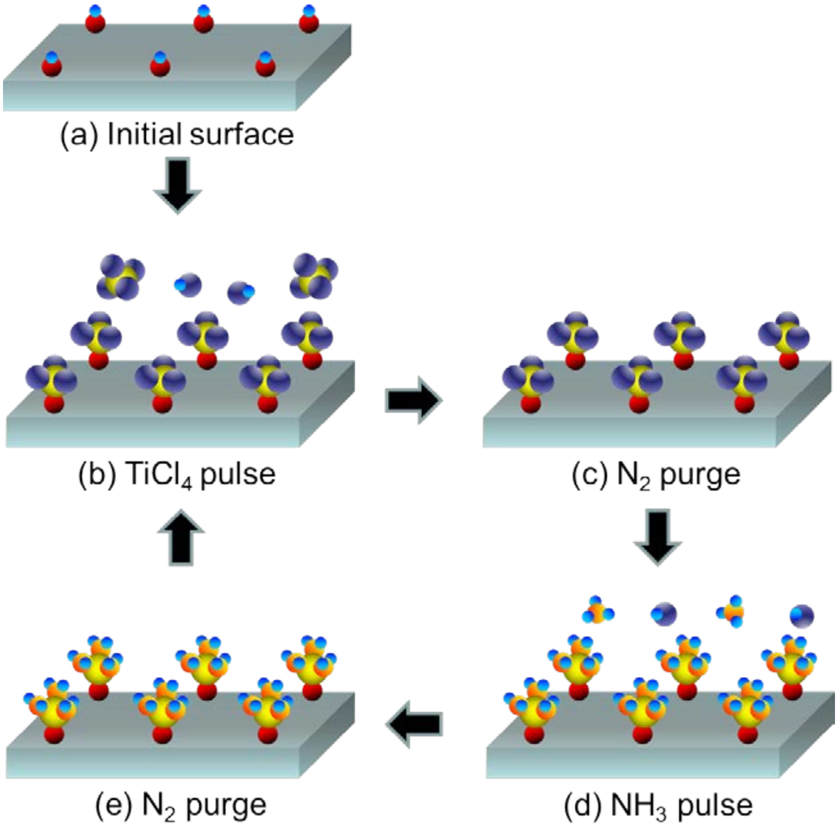

Figure 1.2. Schematic representation of the surface reactions during ALD of TiN using $TiCl_4$ and NH_3 as precursors.

The growth of ALD films (oxides, nitrides) commonly exhibits an incubation stage which is attributed to the chemical states of the initial substrate surface [29-31]. For the thermal ALD of TiN on SiO_2, the incubation can last for a few tens of ALD cycles. Hereafter, the growth continues with the nucleation until a linear growth is achieved. Depending on the deposition condition, the nucleation can occur dominantly in either 2D or 3D mode [5, 32]. In the linear stage, the film thickness increases linearly with the number of ALD cycles. The typical TiN growth rate in this stage for thermal ALD using $TiCl_4$ and NH_3 precursors varies from 0.02 to 0.04 nm/cycle in the temperature range 350–550 ^{o}C [5, 33-34].

It is important to note that to achieve the ALD’s unique features, the ALD precursors must have specific properties. This has been reported in detail in the literature [27-27, 35]. Briefly, the precursors must be sufficiently volatile with a minimum vapor pressure at a temperature not sufficient for their thermal decomposition. A vapor pressure of 0.1 Torr usually suffices and ensures effective precursor-to-surface fluxes. For the self-limiting surface reaction, the precursor must not self-react, including decomposition on the substrate surface or in the gas phase. The precursor must also be highly reactive with the other precursor previously chemisorbed on the surface to enable fast and complete reactions. Furthermore, there should be no etching of the deposited film or substrate by the precursors or the by-products. $TiCl_4$ and NH_3 fulfill these requirements for ALD of TiN.

1.3. Thin film deposition facilities

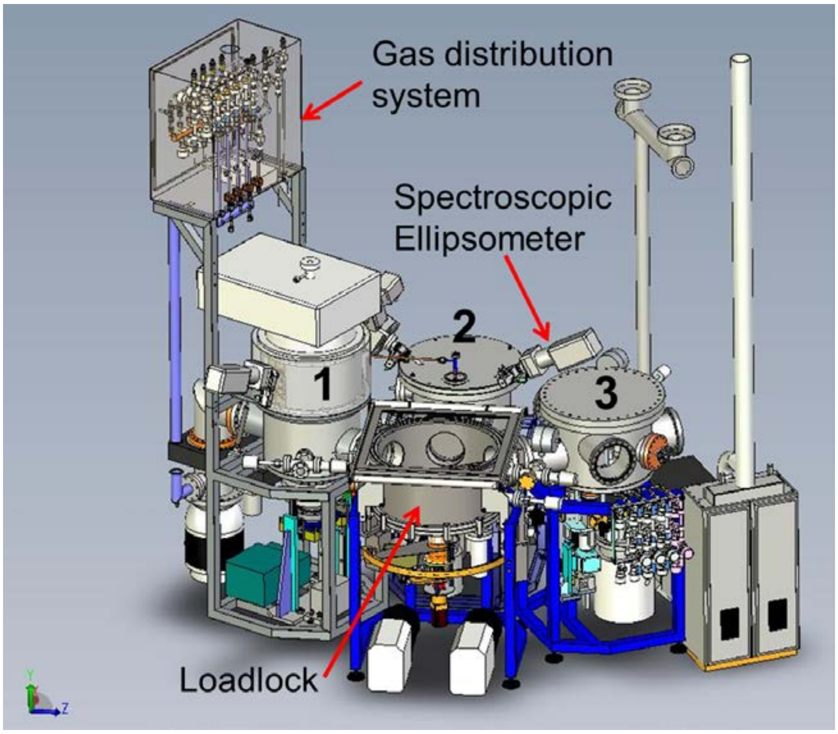

Figure 1.3. A drawing of the home-built cluster system consisting of gas-distribution network and 3 reactors connected to the loadlock. A spectroscopic ellipsometer (Woollam M2000) is mounted on reactors 1 and 2 to *in situ* (real-time) monitor the film growth.

Fig. 1.3 schematically shows the home-built cluster system used in this work to grow a variety of thin films, including ALD TiN. The system consists of the gas-distribution network and 3 reactors connected to loadlock. The plasma reactor (reactor 1) is used for the plasma enhanced CVD of SiO_2 films at temperature as low as 150 ^{o}C [36]. High-K dielectrics (e.g. Al_2O_3) can be deposited in reactor 3 by ALD [37]. The ALD of TiN, CVD of amorphous silicon (a-Si), and ALD of AlN are carried out in reactor 2 [17, 38]. Reactors 1 and 2 are equipped with a spectroscopic ellipsometer, SE (Woollam M2000), for *in situ* (real-time) diagnostics of the film growth. The loadlock allows (i) keeping the reactors under high vacuum during sample loading/unloading steps, and (ii) sample transfer between the reactors to grow multilayer structures without vacuum break. The latter is essential to prevent native oxidation of the layers when exposed to air.

Fig. 1.4 shows the inner chamber of reactor 2 intended for ALD of TiN. The volume of the chamber is approximately 25 cm^3. The small volume reduces the precursor delivery and purge time, to efficiently maintain an ALD mode.

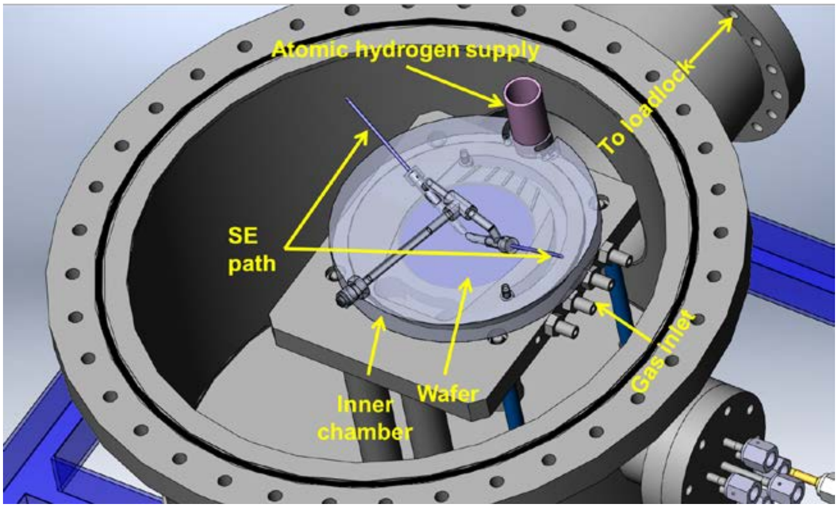

Figure 1.4. Inside ALD reactor 2: inner chamber with a volume of 25 cm^3, SE optical path and the atomic hydrogen supply are indicated.

In addition, we integrated our home-designed hot-filament item into reactor 2, to create atomic hydrogen by dissociation of molecular hydrogen on a hot W filament (see section 1.1 for the purpose).

1.4. Thesis outline

Following this chapter, in **Chapter 2** we discuss on the application of spectroscopic ellipsometry (SE) in studying the optical functions of TiN. We used these optical functions to determine the film thickness, optical and electronic properties of the TiN films. **Chapter 3** reports on the initial nucleation and growth mechanism of ALD TiN thin films at 350 and 425 °C. By combining SE, atomic force microscopy (AFM) and electrical characterization, we demonstrate that the growth obeys Stranski–Krastanov model starting with a 2D mode followed by a 2D-3D transition. The results show that ultra-thin (sub-nanometer thin) continuous TiN films can be deposited by ALD. **Chapter 4** reports on the resistivity, temperature coefficient of resistance and electric field effect in thin TiN films down to sub-nanometer scale in thickness. The resistivity of TiN was determined by both SE and electrical test structures. We extracted the temperature coefficient of resistance (TCR) of TiN for different film thicknesses from the electrical measurements and found that with decreasing film thickness, the TCR values changed sign from positive to negative (metal-semimetal transition). In the last part of the chapter, we report on the electric field effect in ultra-thin TiN films, in both metallic and semimetallic states. **Chapter 5** reports on the influence of native oxidation on electrical behavior of thin ALD TiN films and on their oxidation kinetics at elevated temperatures in dry oxygen. In **Chapter 6**, we report on the generation of atomic hydrogen by hot filament and its impact on surface chemistry in $TiCl_4/NH_3$ system. Finally, in **Chapter 7**, the conclusions of this work and recommendations for further research are given.

References

[1] S. Bystrova, A. A. I. Aarnink, J. Holleman, and R. A. M. Wolters, *J. Electrochem. Soc.* **152**, G522 (2005).

[2] J. S. Becker, and R. G. Gordon, *Appl. Phys. Lett.* **82**, 2239 (2003).

[3] E. Langereis, S. B. S. Heil, H. C. M. Knoops, W. Keuning, M. C. M. van de Sanden, and W. M. M. Kessels, *J. Phys. D: Appl. Phys.* **42**, 073001 (2009).

[4] J. W. Elam, M. Schuisky, J. D. Ferguson, and S. M. George, *Thin Solid Films* **436**, 145 (2003).

[5] A. Satta, J. Schuhmacher, C. M. Whelan, W. Vandervorst, S. H. Brongersma, G. P. Beyer, K. Maex, A. Vantomme, M. M. Viitanen, H. H. Brongersma, and W. F. A. Besling, *J. Appl. Phys.* **92**, 7641(2002).

[6] B. S. Lim, A. Rahtu, and R. G. Gordon, *Nat. Mater.* **2**, 749 (2003).

[7] H. Kim, and S. M. Rossnagel, *J. Vacuum Sci. Technol. A* **20**, 802 (2002).

[8] K.-E. Elers, V. Saanila, W.-M. Li, P. J. Soininen, J. T. Kostamo, S. Haukka, J. Juhanoja, and W. F. A. Besling, *Thin Solid Films* **434**, 94 (2003).

[9] F. Fillot, S. Maîtrejean, I. Matko, and B. Chenevier, *Appl. Phys. Lett.* **92**, 023503 (2008).

[10] L. Wu, H. Y. Yu, X. Li, K. L. Pey, J. S. Pan, J. W. Chai, Y. S. Chiu, C. T. Lin, J. H. Xu, H. J. Wann, X. F. Yu, D. Y. Lee, K. Y. Hsu, and H. J. Tao, *Appl. Phys. Lett.* **96**, 113510 (2010).

[11] S. Jeon, and S. Park, *J. Electrochem. Soc.* **157**, H930 (2010).

[12] H. I. Hanafi, S. Tiwari, and I. Khan, *IEEE Trans. Electron Devices* **43**, 1553 (1996).

[13] S. Tiwari, F. Rana, H. Hanafi, A. Hartstein, E. F. Cabbé, and K. Chan, *Appl. Phys. Lett.* **68**, 1377 (1996).

[14] B. de Salvo, C. Gerardi, S. Lombardo et al., *Tech. Dig. - Int. Electron Devices Meet.* 2003, 597.

[15] T. Baron, A. Fernandes, J. F. Damlencourt, B. De Salvo, F. Martin, F. Mazen, and S. Haukka, *Appl. Phys. Lett.* **82**, 4151 (2003).

[16] J. Dufourcq, S. Bodnar, G. Gay et al., *Appl. Phys. Lett.* **92**, 073102 (2008).

[17] I. Brunets, A. A. I. Aarnink, A. Boogaard, A. Y. Kovalgin, R. A. M. Wolters, J. Holleman, and J. Schmitz, *Surf. Coat. Tech.* **201**, 9209 (2007).

[18] R. Pappu, B. Recht, J. Taylor, and N. Gershenfeld, *Science* **20**, 2026 (2002).

[19] R. Enderlein, and N. J. M. Horing, *Fundamentals of Semiconductor Physics and Devices*, World Scientific, Singapore (1997).

[20] C. T. Black, and J. J. Welser, *IEEE Trans. Electron Devices* **46**, 776 (1999).

[21] K. S. Novoselov, A. K. Geim, S. V. Morozov, D. Jiang, Y. Zhang, S. V. Dubonos, I. V. Grigorieva, and A. A. Firsov, *Science* **22**, 666 (2004).

[22] S. B. S. Heil, J. L. van Hemmen, C. J. Hodson, N. Singh, J. H. Klootwijk, F. Roozeboom, M. C. M. van de Sanden, and W. M. M. Kessels, *J. Vac. Sci. Technol. A* **25**, 1357 (2007).

[23] S. M. George, *Chem. Rev.* **110**, 111 (2010).

[24] R. Doering, and Y. Nishi, *Handbook of Semiconductor Manufacturing Technology*, 2nd Ed., CRC Press, Boca Raton, FL (2008).

[25] J. L. van Hemmen, S. B. S. Heil, J. H. Klootwijk, F. Roozeboom, C. J. Hodson, M. C. M. van de Sanden, and W. M. M. Kessels, *J. Electrochem. Soc.* **154**, G165 (2007).

[26] M. Ritala, and M. Leskelä, "Ch. 2: Atomic layer deposition," in *Handbook of thin film materials part 1: Deposition and processing of thin films*, vol. 1, H. S. Nalwa, Ed., Academic Press, (2002).

[27] M. Leskelä, and M. Ritala, *Thin Solid Films* **409**, 138 (2002).

[28] R. L. Puurunen, *J. Appl. Phys.* **97**, 121301 (2005).

[29] S. S. Lee, J. Y. Baik, K.-S. An, Y. D. Suh, J.-H. Oh, and Y. Kim, *J. Phys. Chem. B* **108**, 15128 (2004).

[30] M. Copel, M. Gribelyuk, and E. Gusev, *Appl. Phys. Lett.* **76**, 436 (2000).

[31] R. L. Puurunen, *J. Appl. Phys.* **95**, 4777 (2004).

[32] H. Van Bui, A. Y. Kovalgin, and R. A. M. Wolters, *ECS J. Solid State Sci. Technol.* **1**, P285 (2012).

[33] K. Choi, P. Lysaght, H. Alshareef, C. Huffman, H.-C. Wen, R. Harris, H. Luan, P.-Y. Hung, C. Sparks, M. Cruz, K. Matthews, P. Majhi, and B. H. Lee, *Thin Solid Films* **486**, 141 (2005).

[34] H. Van Bui, A. W. Groenland, A. A. I. Aarnink, R. A. M. Wolters. J. Schmitz, and A. Y. Kovalgin, *J. Electrochem. Soc.* **158**, H214 (2011).

[35] C. Musgrave, and R. G. Gordon, *Future Fab Int.* **18**, 126 (2005).

[36] A. Boogaard, A. Y. Kovalgin, and R. A. M. Wolters, *Microelectron. Eng.* **86**, 1707 (2009).

[37] R. Bankras, J. Holleman, J. Schmitz, J. M, Sturm, A. I. Zinine, H. Wormeester, and B. Poelsema, *Chem. Vap. Deposition* **12**, 275 (2006).

[38] A. W. Groenland, R. A. M. Wolters, A. Y. Kovalgin, and J. Schmitz, *J. Nanosci. Nanotechnol.* **11**, 8368 (2011).

2

Spectroscopic ellipsometry for studying ALD TiN films

This chapter discusses the applications of spectroscopic ellipsometry in studying the optical functions and measuring film thickness of TiN thin films grown by ALD. We employ the Drude–Lorentz model to parameterize the dielectric functions of the films. The film thickness obtained by SE is compared with the results obtained from other thickness measurement techniques such as HR-TEM/SEM and XRF. The results show a good agreement in a wide thickness range, indicating the reliable applicability of the SE technique and the Drude–Lorentz model. We use SE to in situ study the growth (Chapter 3), the resistivity (Chapter 4) and the real-time oxidation of ALD TiN films (Chapter 5).

2.1. Introduction

Spectroscopic ellipsometry (SE) is an optical characterization technique which is commonly used for determination of thickness and optical functions of thin films [1]. With the advantages of a non-destructive and highly sensitive (sufficient to detect changes in thickness down to sub-monolayer [2]) technique, SE has been widely employed to study thin film properties during deposition processes. These include the studies on optical and electronic properties, growth characteristics, and film thicknesses in multilayer structures. The results demonstrate that SE is a reliable tool for studying physical properties and growth mechanism of various materials [3-8].

This chapter reports on the applications of SE in studying the dielectric functions and measuring thickness of thin TiN films grown by ALD. We used the Drude–Lorentz model for modeling the dielectric functions of TiN. The film thickness was measured by SE and compared with the results obtained from other thickness measurement techniques such as SEM, TEM and XRF. We further employed SE to observe the real-time growth of TiN during deposition.

2.2. Experimental

The ALD of TiN was performed in our home-built single-wafer ALD reactor on a 4-inch Si wafer covered with 100 nm thermally grown SiO_2. Prior to the deposition, the wafer was cleaned in a standard cleaning process including successive immersion into fuming and boiling HNO_3. The wafer was then loaded into the ALD reactor via the loadlock which allowed to keep the reactor under high vacuum (base pressure of 2×10^{-7} mbar) continuously. In the next step, the wafer was heated up by a resistive heater in N_2 ambient at a pressure of 10 mbar. The temperature was measured by a thermocouple located in the wafer holder and controlled by a PID controller. The depositions were carried out in the temperature range of 350–425 ^{o}C; the process pressure varied between 2.6 and 3.2 $\times10^{-2}$ mbar. An ALD cycle consisted of a 2 s pulse of $TiCl_4$ precursor, followed by a 2 s pulse of NH_3. An N_2 purge of 4 s was introduced in between the precursor pulses to remove the excess precursors and the reaction by-products.

The ALD reactor is equipped with a Woollam M2000 spectroscopic ellipsometer operating in the wavelength range of 254–1688 nm. The ellipsometer is mounted on the chamber with an angle of incidence of 70^{o}. The *in situ* SE measurements as a function of time were taken at 2.5 s intervals. The film thickness was determined from the *in situ* measurements. This was verified by high resolution transmission/ scanning electron microscopy (HR-TEM/SEM) and X-ray fluorescence (XRF).

2.3. Results and discussion

2.3.1. Spectroscopic ellipsometry and dielectric functions of thin TiN films

In SE, the sample to be analyzed is illuminated with a beam of polarized light. Ellipsometry characterizes the light reflected from (or transmitted through) the sample upon measuring the change in polarization state in terms of ellipsometric parameters Psi (Ψ) and Delta (Δ) defined as [1]

$$\tan \Psi e^{i\Delta} = r = \frac{r_p}{r_s} \tag{2.1}$$

where r is defined as the ratio of the reflectivity for p-polarized light (r_p) to s-polarized light (r_s). Ψ and Δ represent the magnitude of the reflectivity ratio and the phase difference between p- and s-polarized light, respectively.

In order to extract the sample parameters such as film thickness and dielectric functions, an optical model is required. The accuracy of the measurements is mathematically estimated by the mean squared error (MSE), χ, which represents the agreement between the measured data and the data simulated by the optical model. Since the optical constants of materials are usually unknown, modeling dielectric functions, constructing optical models, and fitting data are very important. For TiN, the dielectric functions are parameterized using the Drude–Lorentz model consisting of a Drude term and two Lorentz oscillators described as [3, 5]

$$\varepsilon = \varepsilon_\infty - \frac{\omega_{pu}^2}{\omega^2 - i\Gamma_D \omega} + \sum_{j=1}^{2} \frac{f_j \omega_{0j}^2}{\omega_{0j}^2 - \omega^2 + i\gamma_j \omega} \tag{2.2}$$

The first item, the Drude term, describes the intraband absorption by free electrons in the material and is characterized by the damping factor Γ_D and the plasma frequency ω_pu which is related to the electron density N by equation

$$\omega_{pu} = \sqrt{\frac{Ne^2}{\varepsilon_0 m^*}} \tag{2.3}$$

where e is the elementary charge, ε_0 is the permittivity of free space, and m^* is the effective electron mass. The damping factor Γ_D is due to the scattering of electrons and determined as the inverse of the mean time between collisions, τ_D.

The interband absorption is described by the Lorentz oscillators (the second term in Eq. (2.2)) located at energy positions ω_{0j} with strength f_j and damping factor γ_j representing the energy loss arising from various scattering mechanisms in the solid. The ε_∞ in Eq. (2.2) is a background constant, which is equal to or larger than unity to compensate for the contribution of higher energy transitions that are not taken into account in the Lorentz term.

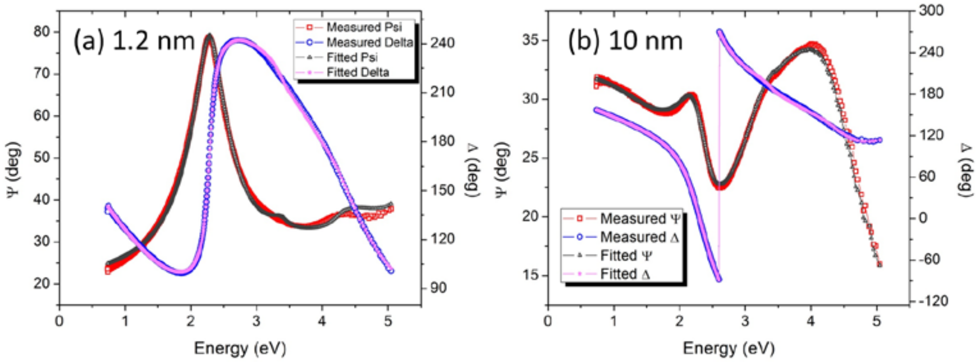

Figure 2.1. Measured and simulated (Ψ,Δ) spectra for TiN films with a thickness of 1.2 nm (a) and 10 nm (b). The Drude–Lorentz model is used to parameterize the dielectric functions from which the simulated data are generated.

Fig. 2.1 shows the measured and the simulated (Ψ, Δ) spectra of a 1.2 nm (a) and a 10 nm (b) thick TiN films. The simulated data are obtained from the Drude–Lorentz model. A rather good fit between the measured and the simulated data was obtained. The real (ε_1) and imaginary (ε_2) parts of the complex dielectric function extracted from the fitting for various thicknesses are shown in Fig. 2.2. The dielectric functions of the 10 nm film show the characteristics of bulk TiN, as reported in the literature [2, 3, 5]. Only a small change was observed for the 7 nm film. However, with decreasing film thickness, the dielectric functions change drastically. For films thinner than 2.5 nm, they are totally different from the functions of bulk TiN. The results indicate a strong thickness dependence of the dielectric functions. To further understand this dependence, we analyzed the individual contributions of the Drude term and the Lorentz oscillators to ε_1 and ε_2.

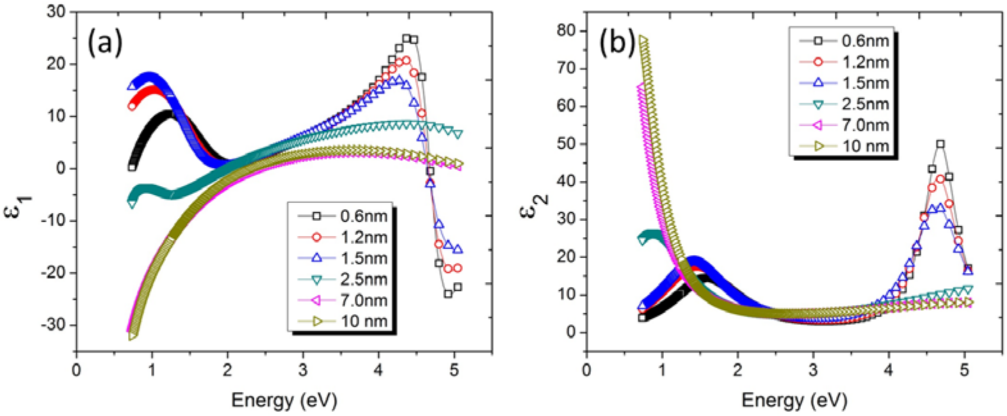

Figure 2.2. Real (a) and imaginary (b) parts of the complex dielectric function of ultra-thin TiN films with various thicknesses.

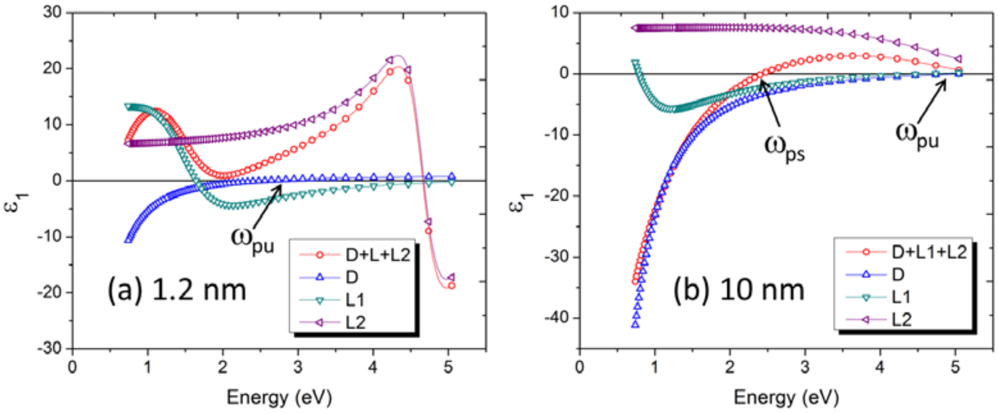

Figure 2.3. Individual contribution of Drude (*D*) and Lorentz (L_1, L_2) terms to the real part ε_1 of the dielectric function of TiN films with a thickness of 1.2 nm (a) and 10 nm (b).

Fig. 2.3 shows the contribution of the Drude and Lorentz term to the real part of the complex dielectric function of a 1.2 nm (a) and a 10 nm (b) TiN film. The Drude term represents the metallic properties of the material and is characterized by the plasma frequency ω_{pu} defined in Eq. 2.3. In an ideal metal, the plasma frequency is defined as the value where the real part of the complex dielectric function is zero ($\varepsilon_1 = 0$).

However, in real metals, the existence of interband transitions at energies lower than ω_{pu} shifts the point where $\varepsilon_1 = 0$ to a lower energy, which corresponds to a so-called screened plasma frequency, ω_{ps} [3]. Therefore, the ω_{pu} in Eq. 2.3 corresponds to the energy ($\varepsilon_{pu} = \hbar\omega_{pu}$) where the Drude term is zero, as denoted in Fig. 2.3. We performed analyses of the dielectric functions in Fig. 2.2 for all the thicknesses in the same manner as shown in Fig. 2.3. The results showed that the plasma energy increased with increasing film thickness ($\varepsilon_{\mathrm{pu}} \approx 2.52$ eV for 1.2 nm and $\varepsilon_{\mathrm{pu}} \approx 5$ eV for 10 nm TiN layer). According to Eq. 2.3, this increase can be attributed to either the increase of conduction electron concentration, N, or the decrease of effective electron mass, m^*, or both effects.

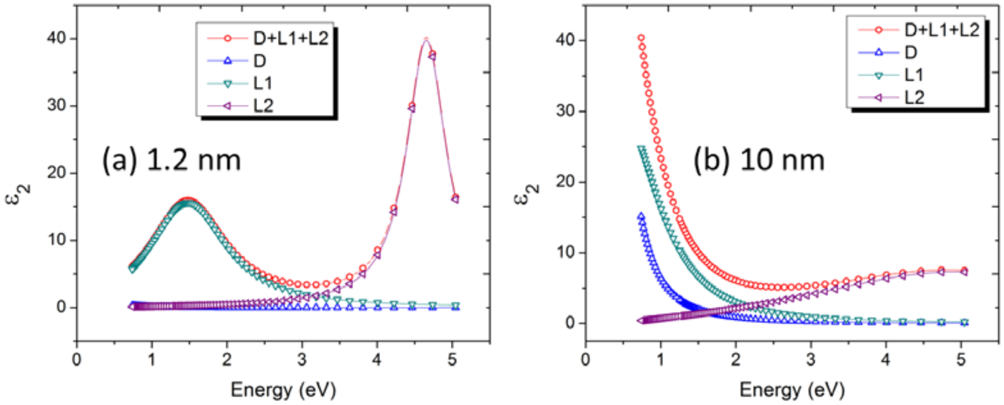

Figure 2.4. Individual contribution of the Drude (D) and Lorentz (L_1, L_2) terms to the imaginary part ε_2 of the dielectric function of TiN films with a thickness of 1.2 nm (a) and 10 nm (b).

The Lorentz oscillators represent the possible interband transitions in TiN. It is reported for bulk TiN that the Lorentz oscillators are located at energies of 3.6–3.7 eV and 5.2–6.2 eV. The former may be attributed to the $\Gamma_{15} \rightarrow \Gamma_{12}$ transition and the latter to the $X_5 \rightarrow X_2$ interband transitions [3] according to the band structure reported by Ern and Switendick [9]. However, in our experiments we found that the locations of the Lorentz oscillators are thickness-dependent. For a 1.2 nm TiN film, the transitions are found at 1.5 eV and 4.7 eV. This is indicated by two strong peaks of ε_2 in Fig. 2.4 (a) and Fig. 2.2 (b). With increasing film thickness, the low-energy transition increases in intensity and shifts to lower energies. In contrast, the intensity of the high-energy transition gradually decreases and the peak position further shifts to higher energies. This is clearly shown in Fig. 2.2 (b): For a 10 nm TiN film, the two Lorentz oscillators are located at 0.7 eV and 5.4 eV. The observed effects can be attributed to a possible change in the electronic properties of TiN such as conduction electron concentration and the energy band diagram as the film thickness is reduced. The former can result in the peak intensity change whereas the latter can shift the peak position. This is consistent with two observations: (i) the evolution of ε_2 as mentioned above and (ii) the metal-semimetal transition which is presented in Chapter 4.

2.3.2. Thickness measurements by SE and other techniques

In order to verify the applicability of the Drude–Lorentz model for parameterization of TiN dielectric functions, we compare the film thickness determined by SE and other *ex situ* characterization techniques. For films thicker than 10 nm, HR-TEM and SEM were used to measure film thickness. Fig. 2.5 shows the HR-SEM and TEM images of 40 nm and 10 nm as-deposited TiN films, respectively. These values are obtained from SE measurements. The additional thickness measurements by SEM and TEM are in very good agreement with the thickness measured by SE. It can be clearly seen in Fig. 2.5 (b) that the TiN made by ALD has a columnar structure containing grains surrounded by amorphous material. The top 2 nm layer in (b) is the native oxide which is formed due to the exposure to air (e.g. during transporting the film to the TEM system). This consequently slightly increases the total thickness of the nominal 10 nm as-deposited TiN (see Chapter 5).

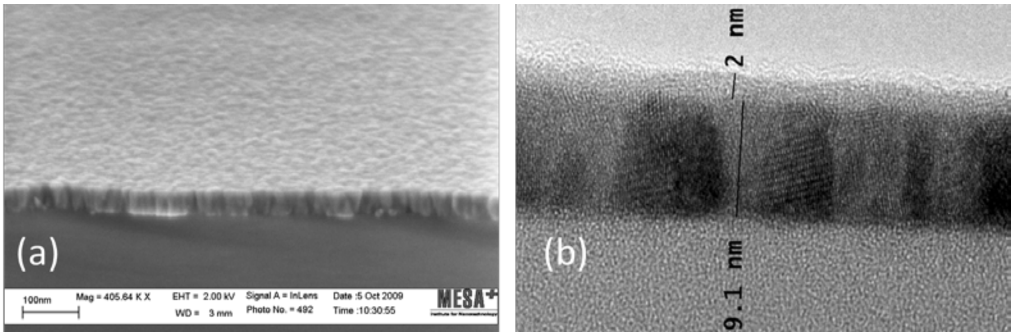

Figure 2.5. HR-SEM image of an as-deposited 40 nm TiN (a) and HR-TEM image of an as-deposited 10 nm TiN film.

For ultra-thin TiN films with thickness in the range from sub-nanometer scale (a few angstroms) to a few nanometers, we use XRF technique to measure the thickness. XRF determines the number of Ti atoms per unit area from which the average film thickness can be calculated. The results are given in Table 2.1. From the number of Ti atoms, the thickness is calculated by using the TiN mass density of 5.21 g/cm^3 [10]. There is agreement between the SE and XRF results.

Table 2.1. A comparison of film thickness determined by XRF and SE for ultra-thin TiN films. TiN mass density of 5.21 g/cm^3 [10] is used.

Number of Ti atoms measured by XRF ($\times 10^{15}$ atoms/cm^2)	TiN film thickness calculated by XRF (nm)	Film thickness measured by SE (nm)
0.21	0.04	0.01
4.7	0.92	0.85
10.7	2.1	1.8
33.2	6.5	5.5

Fig. 2.6 shows the thickness comparison between SE and the other characterization techniques. The comparison shows that the thickness measured by SE is in good agreement with that obtained by the other methods, in a wide thickness range. This verifies the applicability of SE and of the Drude–Lorentz model to characterize thin TiN films.

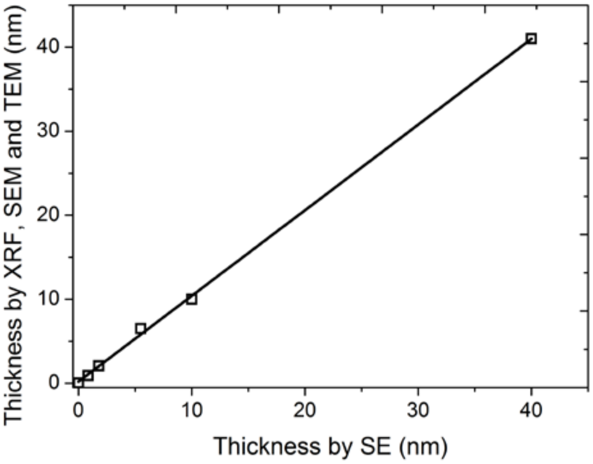

Figure 2.6. Thickness comparison between *in situ* SE and the other *ex situ* characterization techniques (SEM, TEM and XRF).

2.3.3. Monitoring the growth of ALD TiN by *in situ* (real-time) spectroscopic ellipsometry

From the dielectric functions of TiN as discussed, we studied the growth of ALD TiN on SiO_2 using SE. The film thickness was determined as a function of number of cycles during deposition as shown in Fig. 2.7 (a). We observed that the film starts to grow after an incubation period, followed by a transient regime. After approximately 400 cycles, the growth continues in a linear regime where the film thickness increases linearly with number of cycles. Our experimental observation is consistent with the characteristic growth model proposed by Satta et al [11].

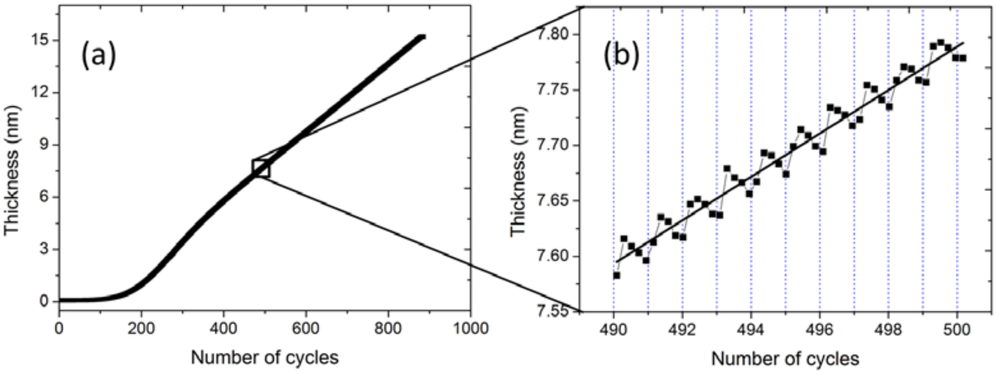

Figure 2.7. (a) The growth of ALD TiN on SiO_2 substrate at 350 ^oC observed by *in situ* SE and (b) the stepwise growth of TiN in the linear regime.

Two half-reactions in the ALD of TiN using $TiCl_4/NH_3$ chemistry are described in Chapter 1. In the first half-reaction, each coming $TiCl_4$ molecule reacts with a preformed $–NH_2$ terminated surface. This reaction replaces the $–NH_2$ groups by the $–TiCl_3$ groups and releases HCl as the by-product. The replacement increases the film thickness since the $–TiCl_3$ is bigger in size [10, 12-13]. The second half-reaction between the $–TiCl_3$ group and the NH_3 precursor switches the surface species from $–TiCl_3$ to $–NH_2$ which consequently decreases the film thickness. The increase and decrease of thickness in every ALD cycle are observed in Fig. 2.7 (b), where the growth during 10 ALD cycles in the linear regime is shown. Each cycle is represented by one step in the growth separated by the vertical dotted grid lines. The stepwise structure of the growth corresponds to the precursor exposures in the $TiCl_4/N_2/NH_3/N_2$ sequences. Since the SE measurements are taken in 2.5 s intervals whereas the ALD pulse sequences are 2/4/2/4 seconds, the measured points in every ALD cycle in Fig. 2.7 (b) are not synchronized with the ALD pulse time. Nevertheless, Fig. 2.7 (b) is sufficient to qualitatively illustrate the surface reactions during TiN ALD using $TiCl_4/NH_3$ chemistry. The solid line shows the trend of the growth. In this regime, a growth rate of 0.02 nm/cycle was obtained.

The results demonstrate that SE can provide highly sensitive (sub-monolayer detection) and reliable diagnostics of the real-time growth of TiN. Therefore, throughout this work we employ SE as the main technique to measure film thickness and properties. In Chapter 3, we use SE for real-time experiments on the initial growth of ALD TiN films on SiO_2. In combination with the Drude–Lorentz model, SE is used to determine the resistivity of thin TiN films. This is reported in Chapter 4. In Chapter 5, SE is employed to measure film thickness of TiN/TiO_2 stacks during the dry oxidation of TiN in oxygen.

2.4. Conclusions

We present the dielectric functions of ALD TiN thin films studied by SE in combination with the Drude–Lorentz model. The results show that for films thicker than 5 nm, the dielectric functions resemble those of the bulk material. Below 5 nm, the dielectric functions are thickness-dependent and change drastically for films thinner than 2.5 nm. We compared the film thickness obtained by SE with other characterization techniques such as TEM, SEM and XRF in a wide thickness range. The results demonstrate good agreement, indicating reliable applicability of the Drude–Lorentz model to describe the optical and electronic properties of (ultra) thin TiN films. We used SE to observe the growth of TiN in real-time. This method can provide further understanding of the growth mechanism, which is discussed in detail in Chapter 3.

References

[1] H. G. Tompkins, and E. A. Irene, *Handbook of Ellipsometry*, William Andrew, New York (2005).

[2] E. Langereis, S. B. S. Heil, H. C. M. Knoops, W. Keuning, M. C. M. van de Sanden, and W. M. M. Kessels, *J. Phys. D: Appl. Phys.* **42**, 073001 (2009).

[3] P. Patsalas, and S. Logothetidis, *J. Appl. Phys.* **90**, 4725 (2001).

[4] S. B. S. Heil, J. L. van Hemmen, M. C. M. van de Sanden, and W. M. M. Kessels, *J. Appl. Phys.* **103**, 103302 (2008).

[5] P. Patsalas, and S. Logothetidis, *J. Appl. Phys.* **93**, 989 (2003).

[6] H. T. Beyene, J. W. Weber, M. A. Verheijen, M. C. M. van de Sanden, and M. Creatore, *Nano Res.* **5**, 513 (2012).

[7] K. Kouda, Y. Hijikata, S. Yagi, H. Yaguchi, and S. Yoshida, *J. Appl. Phys.* **112**, 024502 (2012).

[8] C. Toccafondi, M. Prato, G. Maidecchi, A. Penco, F. Bisio, O. Cavalleri, and M. Canepa, *J. Colloid Interf. Sci.* **364**, 125 (2011).

[9] V. Ern and A. C. Switendick, *Phys. Rev.* **137**, A1927(1965).

[10] D. R. Lide, and W. M. Haynes, *CRC Handbook of Chemistry and Physics,* 90th Ed., CRC Press, Boca Raton, FL (2010).

[11] A. Satta, J. Schuhmacher, C. M. Whelan, W. Vandervorst, S. H. Brongersma, A. Vantomme, M. M. Viitanen, H. H. Brongersma, and W. F. A. Besling, *J. Appl. Phys.* **92**, 7641 (2002).

[12] H. Tiznado, and F. Zaera, *J. Phys. Chem. B* **110**, 13491 (2006).

[13] H.-L. Lu, W. Chen, S.-J. Ding, M. Xu, D. W. Zhang, and L.-K. Wang, *J. Phys.: Condens. Matter.* **18**, 5937 (2006).

3 Growth of sub-nanometer thin continuous TiN films by atomic layer deposition

This chapter reports on the growth mechanism of TiN thin films by atomic layer deposition at 350 °C and 425 °C. We observe that the growth obeys the Stranski–Krastanov model starting with a 2D mode (continuous layers) followed by a 2D-3D transition (onset of islanding). This transition is temperature independent and takes place as the film thickness reaches 0.7 nm, which is equivalent to 3 monolayers of TiN. The growth of the 3D islands (on the continuous layers) eventually leads to their coalescence which occurs at 2.5 nm and 3.5 nm for the growth at 350 °C and 425 °C, respectively. Before the coalescence, new nuclei are constantly formed during the growth. Hereafter, the film grows with a constant growth rate of 0.02 nm/cycle at both temperatures.

3.1. Introduction

During last several decades, thin films of titanium nitride (TiN) have gained much interest because of their low resistivity and compatibility with complementary metal-oxide-semiconductor (CMOS) processes. Thin TiN films made by atomic layer deposition (ALD) are commonly used as diffusion barrier and gate material for CMOS devices [1-6]. In these applications, formation of a continuous film is crucial since this strongly affects its barrier and electrical properties. However, for specific applications, formation of layers at thicknesses before their closure point can be preferred. For example, discontinuous TiN films are utilized for nonvolatile memory devices [7-9]. These various application areas state different and sometimes opposite demands to the initial film nucleation and growth. Making very thin but continuous films implies a better pronounced lateral two-dimensional (2D) growth in comparison to their vertical growth. In contrast, formation of discontinuous granular films requires a preferential three-dimensional (3D) growth. Therefore, both reliable monitoring and understanding of the initial film growth are needed to achieve the desired film properties and to further explore the ultimate potential of ultra-thin films.

The initial growth and continuity of ALD TiN on SiO_2 were previously studied by Satta et al. using low energy ion scattering (LEIS) and Rutherford backscattering spectroscopy (RBS) techniques [10-11]. The ALD of TiN was carried out at temperatures of 350 ^{o}C and 400 ^{o}C with a maximum gas pressure of 2 Torr in the chamber. The authors reported that the initial growth of the film was dominated by Volmer-Weber mechanism (3D growth) as the reactant chemisorption preferentially took place on the already deposited TiN islands rather than on the remaining uncovered SiO_2 surface. A similar observation was reported by Patsalas et al. where the TiN was prepared by sputtering technique [12].

However, the initial growth of a film is strongly influenced by kinetic processes which include the adsorption and desorption, capture by surface steps and clusters, and renucleation [13]. These processes are affected by various deposition conditions such as temperature, pressure, and substrate parameters. For example, a lower precursor pressure will elongate the migration path of the adsorbed species until they find the most energetically favorable sites to form stable nuclei. Enhancing the surface migration can cause a preferentially lateral growth. Therefore, by changing the deposition conditions, one can expect to be able to manipulate the growth mechanism.

This chapter presents the growth of ALD TiN films on SiO_2 substrate at low process pressure (i.e. $2.6–3.2 \times 10^{-2}$ mbar). We used spectroscopic ellipsometry (SE) for *in situ* real-time monitoring the growth. We further employed atomic force microscopy (AFM) and electrical measurements to characterize the films. We conclude that the initial growth of this ALD TiN obeys the Stranski–Krastanov model in which the TiN starts growing in a 2D mode followed by a 2D-3D transition when the film reaches a critical thickness of about 0.7 nm.

3.2. Experimental

The thermal ALD of TiN was performed in our home-built single-wafer ALD reactor described in Chapter 1. The depositions were carried out at temperatures of 350 °C and 425 °C; the process pressure varied between 2.6 and 3.2 $\times 10^{-2}$ mbar. The growth of the film was monitored in real time by *in situ* spectroscopic ellipsometry. The thickness verification was done by high-resolution transmission/scanning electron microscopy (HR-TEM/SEM) and X-ray fluorescence (XRF) spectroscopy (Chapter 2). The surface morphology of the films was characterized by AFM using a Dimension D3100 Nanoscope IVa Controller, Veeco Instruments.

For electrical measurements, we fabricated test structures to characterize electrical properties of ultra-thin TiN films. Details of the fabrication are described in Chapter 4. The TiN layers were deposited on prepatterned Pt electrodes. To prevent TiN oxidation when exposed to air, an amorphous silicon (a-Si) layer was *in situ* deposited onto the TiN (without vacuum break) [14]. The TiN/a-Si stack was patterned to realize different measurement structures. Coating a primer layer on the surface prior to the measurements ensured a negligible surface leakage current. The electrical measurements were carried out using a Karl-Suss PM8 and a Cascade Microtech low-leakage manual probe station.

3.3. Results and discussion

The dielectric functions of TiN and the optical SE model are presented in Chapter 2. The film thickness as a function of the number of ALD cycles at 350 °C and 425 °C is depicted in Fig. 3.1 (see squares and triangles, respectively). The growth rate is determined as the first derivative of the growth curve. The analyses of the growth and growth rate curves are presented in the next section of this chapter.

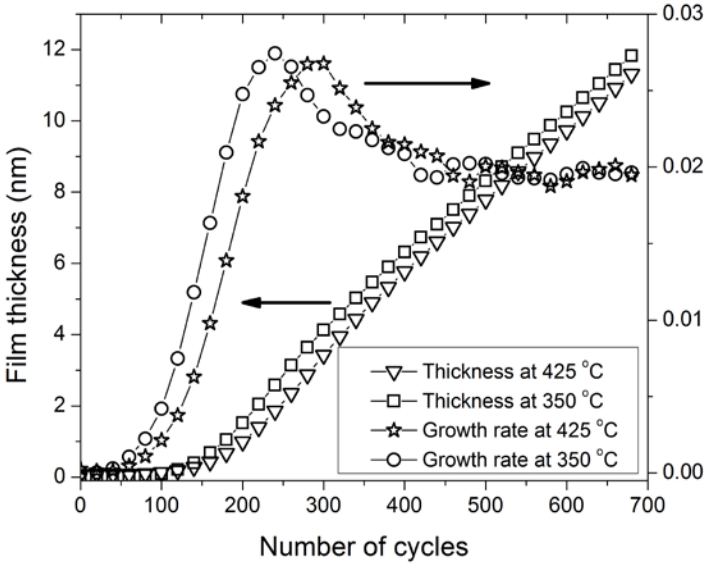

Figure 3.1. Growth and growth rate curves of TiN at 350 °C and 425 °C monitored by *in situ* SE. The growth rate is determined as the first derivative of the growth.

As spectroscopic ellipsometry measures the average film thickness, the actual surface morphology (e.g. continuity, granularity) cannot be determined. Therefore, we extensively used AFM technique for further investigation.

The surface morphology of a 3.5 nm (grown at 425 °C) and a 2.5 nm (grown at 350 °C) TiN film is shown in Fig. 3.2. One can see a granular structure consisting of islands connected to each other. The thicknesses in the figure correspond to the maxima of the growth rate curves shown in Fig. 3.1. This will be discussed in the following part. The height variations (from the lowest to the highest point on the surface) of the islands are 3.4 ± 0.1 nm and 2.4 ± 0.1 nm at 425 °C and 350 °C, respectively. However, the lateral grain dimensions are 10–15 times larger than the vertical sizes (Fig. 3.2). The results suggest the preferential lateral growth of the islands. Since thin TiN films are quickly oxidized when exposed to air even at room temperature [15], the initial TiN islands can be partially oxidized (e.g. during transportation to the AFM system). This oxidation can consequently cause a volume expansion of the islands. However, this effect is negligible in comparison with the average lateral island size.

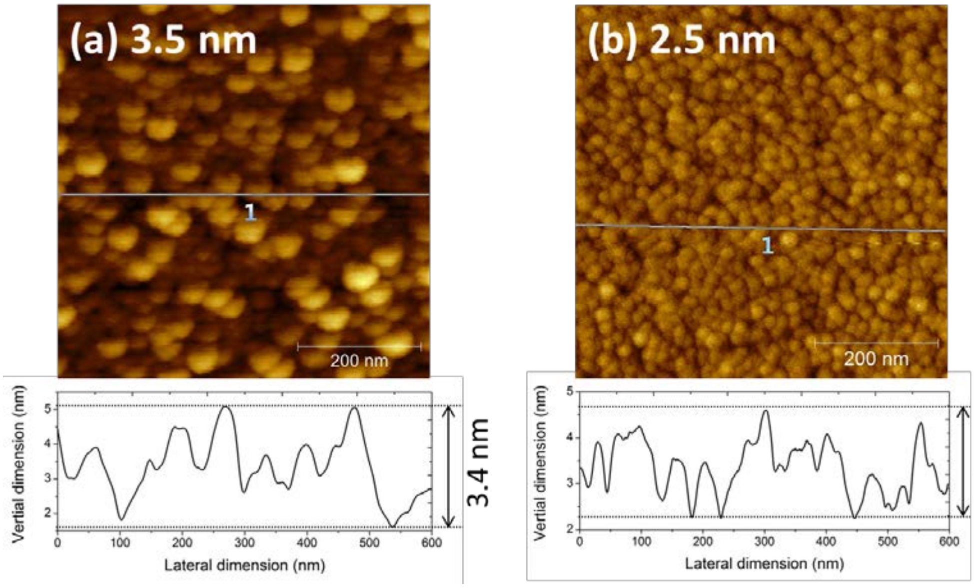

Figure 3.2. 2D AFM images showing the surface of the initial 3.5 nm thin TiN film grown at 425 °C (a) and 2.5 nm thin TiN film grown at 350 °C (b). The bottom graphs show the cross sections along the lines drawn in the AFM images (marked with “1”) from which the height variation and the lateral island size can be estimated.

Fig. 3.3 shows the surface morphologies and profiles of TiN films with as-deposited thickness of 1.8 nm, 1.5 nm, 0.8 nm and the initial SiO_2 surface. For the 1.8 nm TiN (Fig. 3.3 (a)), the AFM image shows a high-density islanded surface with the lateral diameter distributed in the range of 20–30 nm (see Table 3.1). For the film with a thickness of 1.5 nm, the islands are separated in space (Fig. 3.3 (b)). No islands are seen for a 0.8 nm thin TiN film. The surface height variation of this layer (i.e. 0.5 ± 0.1 nm) is comparable to that of the initial SiO_2 surface (Fig. 3.3 (c)-(d)). The results indicate that with decreasing film thickness to below 2 nm, the granularity decreases and the island size becomes smaller. Finally the surface flattens out. From the AFM images, the island dimensions of TiN with various film thicknesses are estimated and given in Table 3.1.

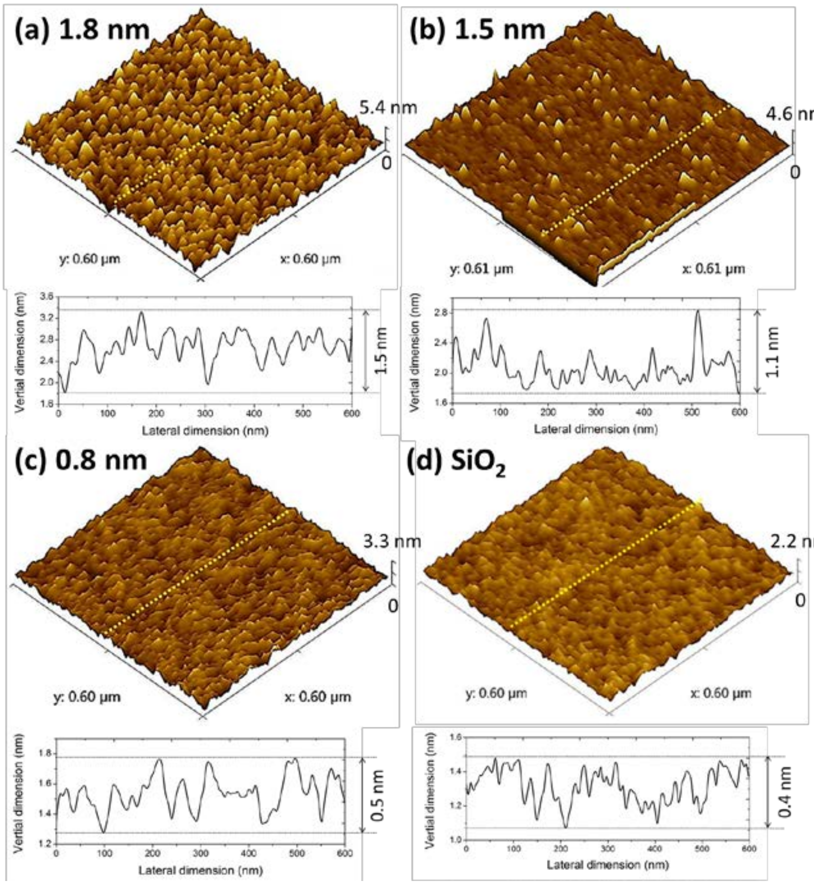

Figure 3.3. 3D AFM images and surface profiles of the films with various initial thicknesses: 1.8 nm (a), 1.5 nm (b), 0.8 nm (c), and initial SiO_2 surface (d). See Table 3.1 for further information.

Table 3.1. AFM measurements of the films with different thickness. The initial SiO_2 film is included for reference.

Film thickness (nm)	Growth temperature (°C)	Height variation (nm)	Average lateral island size (nm)
0.8	350	0.5 ± 0.1	No islands
1.5	425	1.1 ± 0.1	10–20, separated islands (see Fig. 3.3 (b))
1.8	350	1.5 ± 0.1	20–30
2.5	350	2.4 ± 0.1	30–40
3.5	425	3.4 ± 0.1	50–60
SiO_2	-	0.4 ± 0.1	No islands

From the AFM measurements, no difference in surface morphology between the initial SiO_2 layer and the 0.8 nm TiN film can be observed. However, the existence of the TiN is confirmed by SE and XRF. Finding the answers for the questions regarding the morphology of the TiN layers led us to the further study on electrical properties of the films. We employed the test structures shown in Fig. 3.4 (see Chapter 4 for more details). In these structures, an a-Si layer was *in situ* deposited onto the TiN layer to prevent the native oxidation of the TiN. The electrical measurements were carried out at room temperature for TiN films grown at 350 °C with thicknesses of 0.65 nm, 0.85 nm, 1.2 nm, 1.8 nm, 2.5 nm, and 4.5 nm.

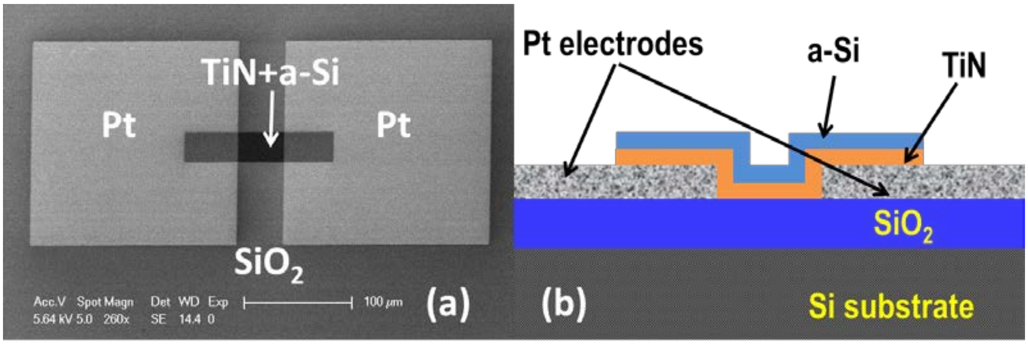

Figure 3.4. Top view SEM image (a) of a fabricated structure for *I-V* measurements of TiN ultra-thin films and (b) schematically drawn cross-sectional view of the structure.

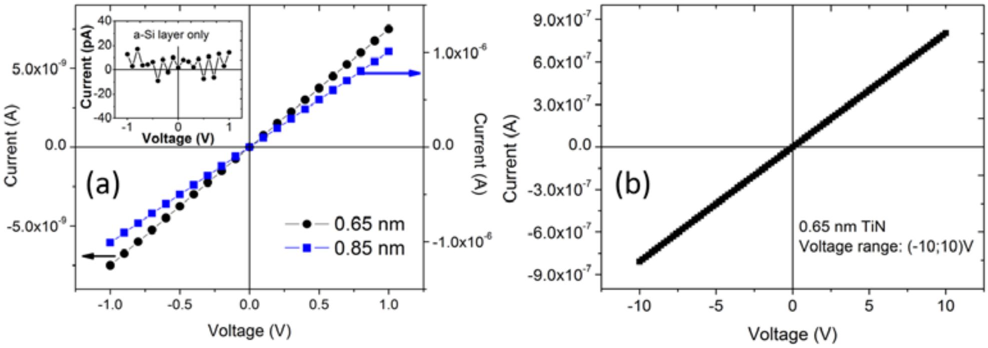

Figure 3.5. (a) The *I-V* characteristics measured on 0.65 nm (circles) and 0.85 nm (squares) TiN films. The inset shows *I-V* curve of the a-Si-only layer measured in the same voltage range (note that the measured current is in the pA range). (b) The *I-V* characteristic of 0.65 nm TiN film measured in the voltage range (-10, 10) V. All measurements were performed at room temperature.

The results show that all these films exhibited linear current-voltage (*I*-*V*) characteristics. Results of the 0.65 nm and 0.85 nm films are plotted in Fig. 3.5 (a); the measurements were performed in a wide voltage range on a number of devices located at different positions of the wafer and resulted in linear *I*-*V* curves (see Chapter 4 for more *I*-*V* characteristics). Measurements on the a-Si-only layer (i.e. without TiN) resulted in a very high resistance which is many orders of magnitude higher than that of the TiN layers (see the inset in Fig. 3.5 (a)). Therefore, a negligible current through the a-Si layer placed on top of TiN can be expected.

Let us assume that the separate islands visible in Fig. 3.3 (b) consist of TiN, and the space in between entirely corresponds to the uncovered SiO_2 substrate. In other words, the films with a thickness of 1.5 nm and below are not yet percolated. Therefore, one can expect tunneling conduction mechanism in such films which would lead to nonlinear *I*-*V* characteristics [16-19]. However, the linear and reproducible *I*-*V* curves obtained for thin films down to 0.65 nm rule out such a possibility. In our experiments, we increased the applied voltage up to ± 10 V still without a noticeable deviation from the linearity (Fig. 3.5 (b)). The results indicate that the 0.65 nm layer is already a continuous film.

Based on the evolution of surface morphology observed by AFM shown in Fig. 3.3, and the *I*-*V* characteristics obtained for ultra-thin TiN films, we propose that the initial growth of ALD TiN on SiO_2 obeys the Stranski–Krastanov model [19]. In this case, the initial growth of a TiN film can be divided into 2 stages. The first stage takes place in a layer-by-layer (2D) mode up to a critical thickness containing one or a few monolayers. This "*intermediate*" layer is known as the wetting layer and the structure is strongly influenced by the underlying substrate [20-23]. As reported, due to the minimum surface energy requirements, the initial 2D growth occurs if the equilibrium concentration of adsorbed atoms on a foreign substrate is higher than that on the same type of substrate [24]. During the growth, the wetting layer is accumulated up to a critical thickness. Beyond this critical thickness, in the second stage, the influence of the underlying SiO_2 gradually vanishes, and the system is thermodynamically favorable for nucleation of islands [19-25]. The 3D growth of the islands eventually leads to coalescence. After that, the growth continues with a constant growth rate. In this regime, the film thickness increases linearly with the number of cycles and the growth rate is constant as observed in Fig. 3.1.

To further understand the evolution of the growth according to the Stranski–Krastanov model, we calculated the first and the second derivatives of the growth curves from Fig. 3.1. Fig. 3.6 shows the first derivative (a), which represents growth rate, and the second derivative (b) ("*acceleration*" of the growth) plotted versus film thickness. On one hand, the growth rate curves (Fig. 3.6 (a)) show a steep increase from 0 to the maximum ~0.027 nm/cycle for both temperatures. The obtained maximum rate corresponds to a film thickness of 2.5± 0.1 nm and 3.5± 0.1 nm for films grown at 350 ^{o}C and 425 ^{o}C, respectively. These are indicated by the vertical dotted lines in the graph. After a slight decrease from the maximum, the growth rate stabilizes at a constant value of ~0.02 nm/cycle. The same growth rate is obtained for both temperatures. They fall in the ALD window of our experiments where the deposition rate is independent of temperature [26]. In addition, according to the characteristic growth model suggested by Satta et al. [11] the peak of the growth rate represents the coalescence point of the 3D islands. At this point, the effective surface area that is exposed to reactants starts to decrease. This consequently results in a slight decrease of the growth rate.

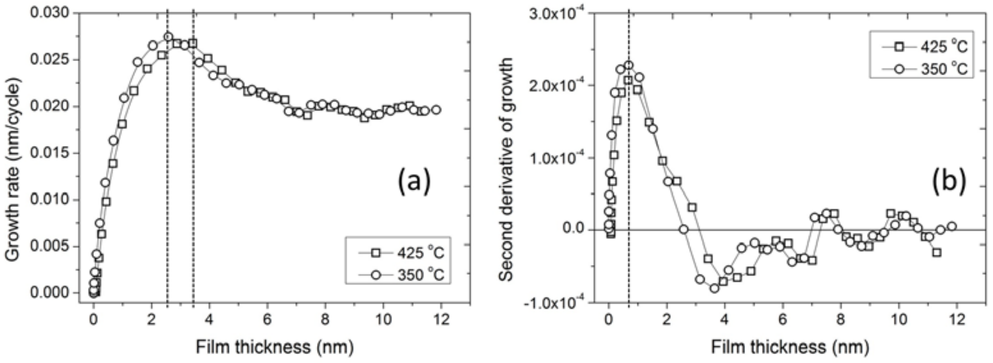

Figure 3.6. First derivative (growth rate) (a) and second derivative (b) of the growth curves from Fig. 3.1 as a function of the film thickness.

On the other hand, the second derivative curves (Fig. 3.6 (b)) exhibit the convex-concave transition at the same peak position corresponding to a film thickness of 0.69 ± 0.1 nm for both temperatures. This is indicated by the vertical dotted line in Fig. 3.6 (b). The thickness of 0.69 nm corresponds to 3 monolayers of TiN (the thickness of one TiN monolayer is approximately 0.23 nm), which is calculated based on the TiN density of 5.21 g/cm^3 [27] The convex-concave transition represents the change of the growth rate. For a thickness less than 0.69 nm, the growth rate increases rapidly, probably due to the increasing nucleation rate. When the thickness exceeds 0.69 nm, the increase of growth rate slows down because the nuclei-formation rate decreases and approaches a constant value. The decrease of the nucleation rate occurs as a result of the transition from 2D to 3D growth.

The *growth rate – time* curves in Fig. 3.1 have a sigmoidal shape, which also indicates a nucleation– and growth-based mechanism. We additionally applied the

Avrami theory [28-30] to study the nucleation and growth aspects of TiN. The Avrami equation is described as [31]

$$Y(t) = 1 - e^{-kt^n} \tag{3.1}$$

where k is the reaction rate constant, t is the time, and n is the Avrami exponent. The value of n reflects the dimensionality of the growth. $Y(t)$ is the fraction of surface coverage at time t. The initial time t_0 is defined as the moment at which the film starts growing. At t_0, there are no nuclei of TiN on the surface. The nucleation is completed at t_T when the growth rate reaches its maximum. To determine the Avrami exponent, Eq. (3.1) can be written as

$$\ln\{\ln[1 - Y(t)]\} = n\ln(t) - \ln k \tag{3.2}$$

The left part of Eq. 3.2 depends linearly on *ln(t)*. The slope gives the Avrami exponent *n* which represents the nucleation mechanism of the growth.

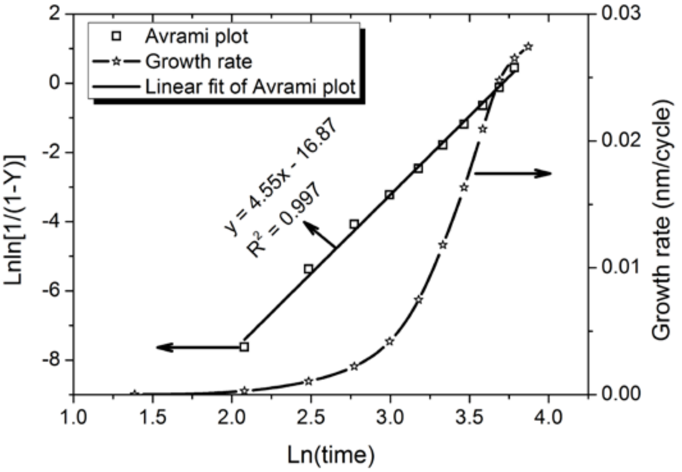

Figure 3.7. Avrami plot (squares) and its linear fit calculated for the growth rate (stars) at 350 ^{o}C according to Eq. 3.2.

Fig. 3.7 shows the Avrami plot (squares) of the film grown at 350 ^{o}C based on the corresponding growth rate curve shown in Fig. 3.1. The linear fit of this plot gives an Avrami exponent *n* of 4.55. Similarly, a value of 4.2 was obtained for the film grown at 425 ^{o}C. According to the Avrami theory, $3 < n < 5$ suggests the formation of new nuclei during the film growth [31]. This is consistent with our interpretation of the SE and AFM measurements discussed above.

In summary, in our case the growth of TiN can be divided into 3 stages. In the first stage, the film grows in a 2D mode up to about 0.69 nm of thickness, which is equivalent to 3 monolayers of TiN. At this thickness, the transition from 2D to 3D growth occurs. The second stage continues with the nucleation and growth of 3D islands. The coalescence of the 3D islands occurs when the growth rates reach their maxima (i.e. at a film thickness of 2.5 nm for 350 ^{o}C and 3.5 nm for 425 ^{o}C). The 2D-3D growth transition is independent of temperature, whereas the coalescence of the islands is temperature dependent. This can be interpreted by the fact that the 2D growth is dominantly affected by the underlying substrate. However, the surface island density in the 3D growth is temperature dependent [28]. At lower temperatures, the island density is higher which consequently results in a faster coalescence. After the coalescence, in the third stage, the film thickness increases linearly with the number of ALD cycles.

3.4. Conclusions

We observed the real-time growth of ALD TiN at 350 ^{o}C and 425 ^{o}C by using *in situ* spectroscopic ellipsometry. AFM and electrical test structures were used to characterize the films. We demonstrate that the initial growth of ALD TiN follows the Stranski–Krastanov model. Accordingly, the entire growth can be divided into 3 stages: (i) 2D growth of a continuous wetting layer; (ii) 2D-3D transition at a thickness of about 0.69 nm followed by the formation and coalescence of 3D islands; (iii) constant rate ALD growth. Stage (i) is dominantly influenced by the underlying substrate and is temperature-independent. Stage (ii), including the coalescence, is strongly affected by temperature. For the films grown at 350 ^{o}C, the coalescence occurs at a thickness of about 2.5 nm, whereas that for the films grown at 425 ^{o}C is 3.5 nm. This difference is due to the influence of temperature on the nucleation of the 3D islands on the wetting layer. Before coalescence, new nuclei are formed during the growth. This is supported by the Avrami theory. Hereafter, in stage (iii), the growth stabilizes at a constant growth rate of 0.02 nm/cycle for both temperatures. This rate is typical for thermal ALD of TiN. The results of our study indicate that atomically thin continuous TiN films are formed by ALD on thermal- SiO_2 from the very beginning of the growth. This conclusion is supported by our intensive study on electric field effect in ultra-thin TiN films further reported in Chapter 4.

References

[1] K.-E. Elers, V. Saanila, W.-M. Li, P. J. Soininen, J. T. Kostamo, S. Haukka, J. Juhanoja, and W. F. A. Besling, *Thin Solid Films* **434**, 94 (2003).

[2] F. Fillot, S. Maîtrejean, I. Matko, and B. Chenevier, *Appl. Phys. Lett.* **92**, 023503 (2008).

[3] L. Wu, H. Y. Yu, X. Li, K. L. Pey, J. S. Pan, J. W. Chai, Y. S. Chiu, C. T. Lin, J. H. Xu, H. J. Wann, X. F. Yu, D. Y. Lee, K. Y. Hsu, and H. J. Tao, *Appl. Phys. Lett.* **96**, 113510 (2010).

[4] S. Jeon, and S. Park, *J. Electrochem. Soc.* **157**, H930 (2010).

[5] F. Fillot, T. Morel, S. Minoret, I. Matko, S. Maîtrejean, B. Guillaumot, B. Chenevier, and T. Billon, *Microelectron. Eng.* **82**, 248 (2005).

[6] D.-G. Park, K.-Y. Lim, H.-J. Cho, T.-H. Cha, I.-S. Yeo, J.-S. Roh, and J. W. Park, *Appl. Phys. Lett.* **80**, 2514 (2002).

[7] S. Choi, S.-S. Kim, M. Chang, H. Hwang, S. Jeon, and C. Kim, *Appl. Phys. Lett.* **86**, 123110 (2005).

[8] S. Maikap, P. J. Tzeng, H. Y. Lee, C. C. Wang, T. C. Tien, L. S. Lee, and M.-J. Tsai, *Appl. Phys. Lett.* **91**, 043114 (2007).

[9] G. Gay, D. Belhachemi, J. P. Colonna, S. Minoret, P. Brianceau, D. Lafond, T. Baron, G. Molas, E. Jalaguier, A. Beaurain, B. Pelissier, V. Vidal, and B. De Salvo, *Appl. Phys. Lett.* **97**, 152112 (2010).

[10] A. Satta, A. Vantomme, J. Schuhmacher, C. M. Whelan, V. Sutcliffe, and K. Maex, *Appl. Phys. Lett.* **84**, 4571 (2004).

[11] A. Satta, J. Schuhmacher, C. M. Whelan, W. Vandervorst, S. H. Brongersma, G. P. Beyer, K. Maex, A. Vantomme, M. M. Viitanen, H. H. Brongersma, and W. F. A. Besling, *J. Appl. Phys.* **92**, 7641 (2002).

[12] P. Patsalasa, and S. Logothetidis, *J. Appl. Phys.* **93**, 989 (2003).

[13] M. Wuttig, and X. Liu, *Ultrathin Metal Films: Magnetic and Structural Properties*, Springer-Verlag, Berlin (2004).

[14] H. Van Bui, A. A. I. Aarnink, A. Y. Kovalgin, and R. A. M. Wolters, *J. Nanosci. Nanotechnol.* **11**, 8120 (2011).

[15] H. Van Bui, A. W. Groenland, A. A. I. Aarnink, R. A. M. Wolters, J. Schmitz, and A. Y. Kovalgin, *J. Electrochem. Soc.* **158**, H214 (2011).

[16] G. Dittmer, *Thin Solid Films* **9**, 317 (1972).

[17] A. Alkhatib, T. Souier, and M. Chiesa, *Thin Solid Films* **520**, 656 (2011).

[18] J. E. Morris, *Thin Solid Films* **11**, 81 (1972).

[19] J. A. Venables, G. D. T. Spiller, and M. Hanbucken, *Rep. Prog. Phys.* **47**, 399 (1984).

[20] O. G. Schmidt, O. Kienzle, Y. Hao, K. Eberl, and F. Ernst, *Appl. Phys. Lett.* **74**, 1272 (1999).

[21] P. B. Joyce, T. J. Krzyzewski, G. R. Bell, B. A. Joyce, and T. S. Jones, *Phys. Rev. B* **58**, R15981 (1998).

[22] G. S. Solomon, J. A. Trezza, A. F. Marshall, and J. S. Harris, Jr., *Phys. Rev. Lett.* **76**, 952 (1996).

[23] E. Korutcheva, A. M. Turiel, and I. Markov, *Phys. Rev. B* **61**, 16890 (2000).

[24] S. Stoyanov, and I. Markov, *Surf. Sci.* **116**, 313 (1982).

[25] J. A. Venables, *Introduction to Surface and Thin Film Processes*, Cambridge University Press, Cambridge (2000).

[26] R. Doering, and Y. Nishi, *Handbook of Semiconductor Manufacturing Technology*, 2nd Ed., CRC Press, Boca Raton, FL (2008).

[27] D. R. Lide, and W. M. Haynes, *CRC Handbook of Chemistry and Physics*, 90th Ed., CRC Press, Boca Raton, FL (2010).

[28] M. Avrami, *J. Chem. Phys.* **7**, 1103 (1939).

[29] M. Avrami, *J. Chem. Phys.* **8**, 212 (1940).

[30] M. Avrami, *J. Chem. Phys.* **9**, 177 (1941).

[31] J. W. Christian, *Theory of Transformation in Metals and Alloys (Part I + II)*, 2rd Ed., Pergamon, (2002).

4 Electrical properties and electric field effect in ultra-thin TiN films

This chapter reports on the resistivity, temperature coefficient of resistance (TCR) and field effect in thin TiN films down to sub-nanometer scale. The resistivity of TiN is determined by both spectroscopic ellipsometry (SE) and electrical test structures. The latter includes circular transfer length method (CTLM) and linear test structures. We determine the TCR of TiN for different film thicknesses from the electrical measurements in a wide temperature range. The results show that with decreasing film thickness, the TCR values change their sign from positive to negative. This change occurs at a thickness of about 2.5 nm. We attribute this effect to the metal-semimetal transition. In the last part of this chapter, we explore the electric field effect in ultra-thin TiN films in the metallic and the semimetallic states and observe up to 22% change of the conduction current for films in the semimetallic state.

4.1. Resistivity of ultra-thin TiN films

4.1.1. Introduction

The resistivity of thin TiN films can be determined by various methods. Spectroscopic ellipsometry (SE), with the advantages of a non-destructive optical technique, has been used to investigate the electrical properties of TiN [1-3]. SE measures the resistivity on the basis of determining the conduction electron concentration and electron scattering effect caused by the interaction between electrons and electric field of the incident light. However, the behavior of electrons under an applied electric field as well as the physical transport of carriers between crystal grains, and the influence of grain boundaries on the actual current flow cannot be obtained by SE. Therefore, electrical test structures, utilizing the current flow between electrical contacts, are needed to characterize the resistivity [4-5]. In addition, as the optical and electrical methods are based on different physical models, it is important to compare the resistivities obtained optically and electrically.

In this section, we report on the resistivity of thin TiN films in the thickness range 0.65–20 nm, determined by SE and electrical test structures. The optical measurements were carried out in real time during the deposition. We used the Drude–Lorentz model to parameterize the complex dielectric function of TiN, from which the resistivity was extracted. The electrical measurements were performed *ex situ* by using CTLM [6, 7] and linear test structures specially designed to measure resistivity of thin films.

4.1.2. Experimental

Deposition of TiN and a-Si passivation layers. TiN films were grown via thermal ALD at 350 °C on Si wafers covered with 100 nm thermally grown oxide, as presented in Chapter 3. Directly after the deposition of TiN, a 15 nm amorphous silicon (a-Si) layer was deposited without vacuum break to prevent TiN oxidation. This was done in the same reactor at 325 °C by low pressure chemical vapor deposition (LPCVD) using trisilane (Si_3H_8) as the source gas.

Fabrication of CTLM test structures. The circular electrodes for the CTLM structures were fabricated using a metal lift-off process. A standard *p*-type (100) Si wafer covered with 100 nm thermal oxide was used as starting material. After spinning the photoresist layer, the wafer was exposed to UV-light through a CTLM mask. Before and after the exposure, the wafer was annealed (soft bake) at 90 ^{o}C and 120 ^{o}C, respectively, for 60 s.

The exposed photoresist was then dissolved in the developer solution. The wafer was further immersed into a buffered HF (BHF) solution for 20 seconds to etch approx. 25 nm of the SiO_2 before sputtering a 5 nm Ti adhesion layer followed by a 20 nm Pt layer to make electrodes. In the next step, the photoresist and the metals on top of it were removed in acetone (lift-off). The TiN and a-Si layer were deposited on top of the structures without further layer patterning.

Fabrication of linear test structures. The linear test structures (LTS) were realized by a two-mask process flow. The first mask was applied to fabricate the linear electrodes using a metal lift-off process after sputtering the metal (Pt), as described above. This was followed by the deposition of the TiN and a-Si layers. The passivation layer was realized on selected samples only. The second mask was used to pattern the TiN and a-Si layers by a photolithography-etching process in $H_2O:HNO_3:HF$ and $H_2O:NH_4OH:H_2O_2$ solutions, respectively, at room temperature.

Material characterization and electrical measurements. The film thickness was measured by SE and verified by high-resolution transmission/scanning electron microscopy (HR-TEM/SEM), helium ion microscopy (HIM) and X-ray fluorescence (XRF) spectroscopy, as explained in Chapter 2. The electrical measurements were carried out using a Karl-Suss PM8 and a Cascade Microtech low-leakage manual probe station. Coating a primer layer on the surface prior to the measurements ensured a negligible surface leakage current.

4.1.3. Principles of the optical and electrical measurements

4.1.3.1. Spectroscopic ellipsometry measurement principle

In Chapter 2, we presented the parameterization of the complex dielectric function of thin TiN by using the Drude–Lorentz model. For more detail we refer to Eqs. 2.2 and 2.3 in Section 2.3.1. Electrical resistivity, ρ, of the material is related to the mean time between collisions, τ_D (also called the scattering time), by the relation [8]

$$\tau_D = \frac{m^*}{\rho N e^2} \tag{4.1}$$

In combination with Eq. (2.3), the resistivity can be expressed as

$$\rho = \left(\frac{1}{\varepsilon_0 \tau_D}\right)\frac{1}{\omega_{pu}^2} \tag{4.2}$$

The resistivity therefore depends on both plasma frequency ω_{pu} and electron scattering time τ_D (ε_0 is the permittivity of free space). The former is related to conduction electron concentration and electron effective mass (see Eq. 2.3, Chapter 2) and is devoted to intrinsic properties of the material. The latter reflects scattering effects of the conduction electrons. From SE measurements, ω_{pu} and τ_D can be obtained [9] and used to calculate the resistivity from Eq. 4.2.

4.1.3.2. CTLM measurement principle

The HIM image of a fabricated CTLM test structure is shown in Fig. 4.1 (a). The TiN material to be measured (the narrow ring marked by the dark-grey color with a spacing *s*) is confined between two bright Pt-electrodes. Fig. 4.1 (b-c) shows the HIM cross-sectional images at the TiN/Pt contact with 20 nm of TiN measured by SE. The upper image obtained from the ion back-scattered measurement (Fig. 4.1 (b)) depicts a brighter Pt layer (compared to TiN) due to the difference in atomic weight of these elements. Combining Fig. 4.1 (b) with the image from the electron back-scattered detector (Fig. 4.1 (c)), the TiN thickness can be measured. This results in 20 nm and is in good agreement with the SE measurements.

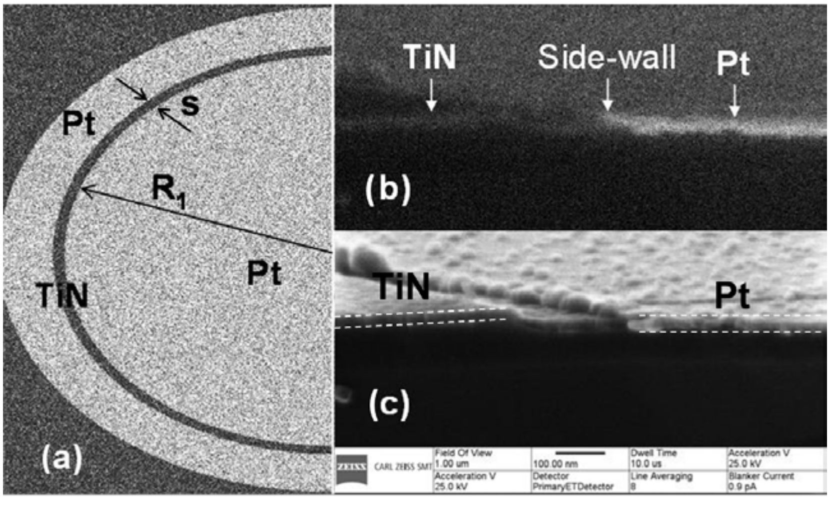

Figure 4.1. A realized CTLM structure with the inner electrode radius R_1 = 250 μm and the gap spacing *s* = 10 μm: (a) –structure layout; (b) and (c) –cross-sectional HIM images of the TiN/Pt contact area obtained from ion- and electron-back scattered analyses, respectively.

A CTLM structure can be transformed into a linear transmission line model (LTLM) structure, as schematically shown in Fig. 4.2, under the condition $R_1 >> s$. To compensate for the difference between the circular and linear layouts, a correction factor is applied. The relation between the resistances in this transformation is described as [6-7]

$$R_L = \frac{R_m}{c} \tag{4.3}$$

where R_m is the resistance measured from the CTLM structures, R_L is the resistance in the linear layout, and c is the correction factor determined as [7]

$$c = \frac{R_1}{s}\ln\left[\frac{R_1 + s}{R_1}\right] \tag{4.4}$$

in which R_1 and s are denoted in Fig. 4.2. With the linear configuration as described in Fig. 4.2, the resistance R_L is determined as

$$R_L = R_{TiN} + 2R_c \tag{4.5}$$

where R_c is the contact resistance between the TiN layer and the Pt-electrode, R_{TiN} is the resistance of the TiN layer calculated by the formula

$$R_{TiN} = \rho\frac{s}{2\pi R_1 t} = \frac{\rho}{t}\frac{1}{2\pi R_1}s = \frac{R_{sh}}{2\pi R_1}s \tag{4.6}$$

where ρ and t are the resistivity and thickness of the TiN layer, respectively. The ratio $\frac{\rho}{t}$ determines the sheet resistance R_{sh}.

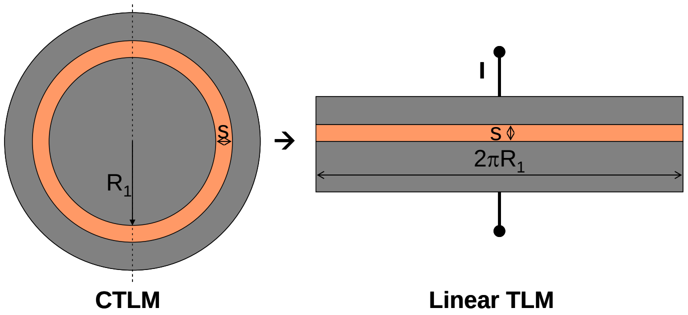

Figure 4.2. The transformation from a circular TLM into a linear TLM under the condition $R_1 >> s$.

Combining Eqs. (4.3), (4.4) and (4.5), the relation between R_m and s is written as

$$\frac{R_m}{c} = \frac{R_{sh}}{2\pi R_1} s + 2R_c \tag{4.7}$$

By plotting R_m/c ratio with a proper correction factor versus gap spacing, a linear fit can be obtained. The slope determines the R_{sh}, and the resistivity can be calculated. The intercept with the vertical axis gives $2R_c$.

4.1.3.3. Linear test structure measurement principle

The layout of a fabricated linear test structure (LTS) is schematically shown in Fig. 4.3. In this structure, current I is forced through the TiN by applying a voltage V between the two Pt electrodes. The total resistance is calculated as

$$R = \frac{V}{I} = \rho \frac{L}{tW} + 2R_c = R_{sh} \frac{1}{W} L + 2R_c \tag{4.8}$$

where L and W are the length and the width of the TiN sheet between the electrodes, respectively. By $2R_c$, two times the contact resistance is expressed. For a given W, by changing the gap spacing L between the two electrodes, the measured resistance R as a linear function of L can be plotted. The R_{sh}, and therefore the ρ can be obtained from the slope of the linear $R(L)$ curve. The intercept with the vertical axis gives $2R_c$.

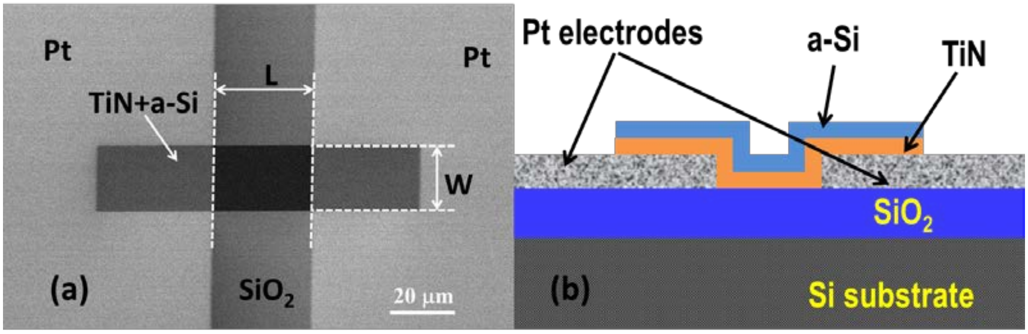

Figure 4.3. (a) SEM image (top-view) and (b) schematically drawn cross-sectional view of a linear structure for electrical resistivity determination of ultra-thin TiN films.

4.1.4. Results and discussion

4.1.4.1. Optical SE measurement results

Using the Drude–Lorentz model, both ω_{pu} and τ_D can be extracted from SE measurements (see section 2.3.1, Figs. 2.1-2.4, Chapter 2 for details). For example, the measurements on a 10 nm TiN resulted in an unscreened plasma energy of 5.0 eV and the scattering time was determined at 1.3 fs. From these data, a resistivity of 160 μΩ·cm was obtained. Similarly, the resistivity as a function of film thickness was obtained for ALD TiN during the deposition, as shown in Fig. 4.4.

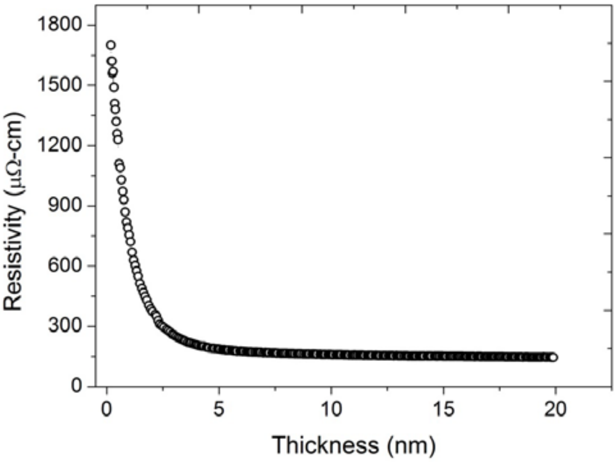

Figure 4.4. Resistivity of TiN obtained by *in situ* spectroscopic ellipsometry during the deposition at 350 ^{o}C.

The electronic properties are strongly influenced by film thickness, especially for ultra-thin films. This is presented in Chapter 2, where the real and the imaginary parts of the complex dielectric function of TiN show a tremendous change with thickness below 5 nm. The dielectric functions coincide with those of the bulk material for films thicker than 7 nm. The change of electronic properties with decreasing film thickness is reflected by the resistivity trend shown in Fig. 4.4. For films thinner than 5 nm, the resistivity increases rapidly with decreasing film thickness. Above 5 nm, the resistivity decreases slowly, flattens out and reaches a value of 145 μΩ·cm for a 20 nm thick film. This value is comparable to resistivity of TiN in the same thickness range obtained by Langereis et al. [3] using SE.

4.1.4.2. Electrical CTLM measurement results

The electrical measurements were carried out by applying and sweeping the voltage between the circular electrodes while measuring the current running through the TiN ring. Figure 4.5 (a) shows the *I-V* characteristics obtained from the measurements on an unpassivated 10 nm TiN layer with different gap spacing. Linear *I-V* curves were obtained, indicating ohmic-contact between TiN and Pt. The measured total resistance R_m plotted versus gap spacing *s* is shown in Figure 4.5 (b) (squares). The linear fit (circles) was obtained after dividing the R_m by the proper correction factor from Table 4.1 for the so-called corrected resistance. From the slope, we obtained a sheet resistance of 163 Ω/□. However, it is important to mention that, during the exposure to air, the surface of the film can be oxidized which reduces the initial TiN thickness (see Chapter 5 for details). For example, we found that the native oxidation of a 10 nm as-deposited TiN layer could result in a 2 nm thick TiO_2 layer on top, thereby reducing the TiN thickness. Therefore, for *ex situ* measurements in air, one should correct for the actual TiN thickness while calculating the resistivity. In this work, thicknesses of the native oxide and the remaining TiN were measured by SE. After the thickness correction, a resistivity of 135 μΩ·cm was obtained. Similarly, the corrected resistivity of 20 nm and 15 nm thick as-deposited TiN films yielded values of 120 μΩ·cm and 125 μΩ·cm, respectively (see Table 5.1 in Chapter 5 for further comparison of the values for corrected and non-corrected thicknesses).

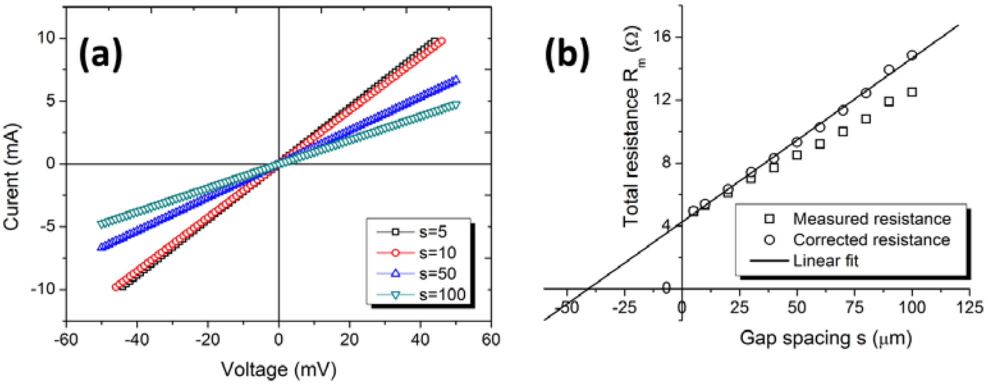

Figure 4.5. (a) *I-V* characteristics measured on an unpassivated 10 nm thick TiN layer with different gap spacing and (b) the linear fit obtained after the transformation of CTLM to linear TLM. The squares show the measured resistance whereas the circles represent the resistance corrected by *c*-factor (Table 4.1).

Measurements on unpassivated ultra-thin TiN films with the thickness in the range between 2.5 nm and 5 nm exhibited non-linear *I-V* curves (Fig. 4.6 (a)), showing high film resistance and its dependence on the applied voltage. The high resistance and the nonlinear behaviour can be attributed to the irreversible change of properties of the TiN as a result of its exposure to air. Firstly, the native oxidation can cause compositional and structural changes. In addition to the formation of surface oxide, the enhanced diffusion of oxygen along grain boundaries to the depth comparable with film thickness can lead to electrical isolation of the grains, and hence increase the resistivity. Secondly, the native oxidation can lead to the formation of Ti-O bonds at the Pt/TiN contacts, resulting in a rectifying (Schottky-like) *I-V* behavior [10].

Table 4.1. Correction factor c for different gap spacing s calculated from Eq. (4.4) for the inner radius R_1 = 250 μm.

Gap spacing (μm)	Correction factor	Gap spacing (μm)	Correction factor
5	0.990	10	0.981
20	0.962	30	0.944
40	0.928	50	0.91
60	0.896	70	0.881
80	0.868	90	0.854
100	0.841		

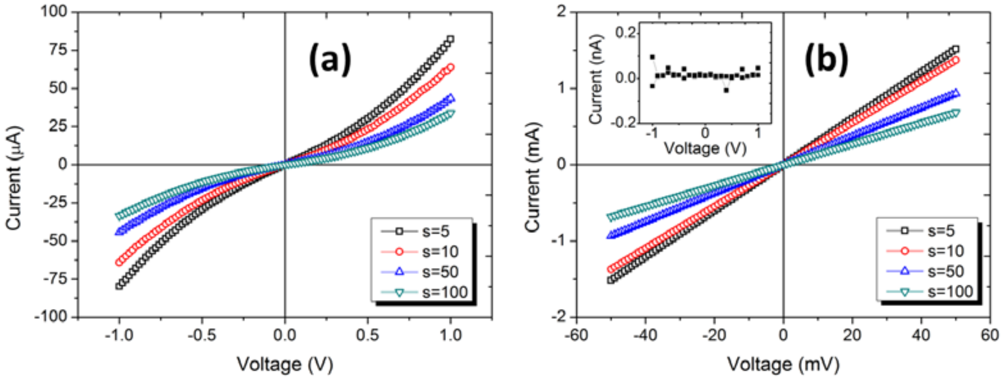

Figure 4.6. *I-V* characteristics of 3.5 nm TiN films without (a) and with (b) a-Si passivation layer (15 nm). The inset in (b) shows *I-V* characteristic of the a-Si-only layer measured in the voltage range (-1; 1) V, with a gap spacing of 10 μm.

To eliminate the native oxidation, an a-Si layer was *in situ* deposited on the thinner TiN films before exposing to air. Measurements on the passivated layers exhibited linear *I-V* curves (Fig. 4.6 (b)). It is important to mention that the electrical measurements on the a-Si-only layer (i.e. without the underlying TiN) resulted in a very high resistance which is many orders of magnitude higher than that of the TiN layers (see the inset of Fig. 4.6 (b)). Therefore, a negligible current through the passivation layer can be expected. From the linear *I-V* characteristics, by following the above calculations, the resistivity of the passivated TiN layers was determined. The values of 400 μΩ·cm and 310 μΩ·cm were obtained for 2.5 nm and 3.5 nm TiN films, respectively.

4.1.4.3. Electrical LTS measurement results

The linear test structures were used for resistivity determination of ultra-thin TiN films in the thickness range 0.65–4.5 nm. Fig. 4.7 (a) shows *I-V* characteristics of a passivated 0.65 nm TiN film. Linear *I-V* curves were obtained, indicating ohmic contact between TiN and Pt and the ohmic behavior of the film. Also for the linear structures, measurements on the a-Si-only layer resulted in a very high resistance, which is many orders of magnitude larger than that of the TiN layers (see the inset in Fig. 4.7 (a)). The measured total resistance *R* versus *L* and the linear fit are shown in Fig. 4.7 (b). From the slope (Eq. 4.7) and for t = 0.65 nm, a resistivity of 7.47×10^5 μΩ·cm was obtained. Similarly, the resistivities of films with thicknesses of 0.85 nm, 1.2 nm, 1.8 nm, 2.5 nm and 4.5 nm were extracted (see Fig. 4.8).

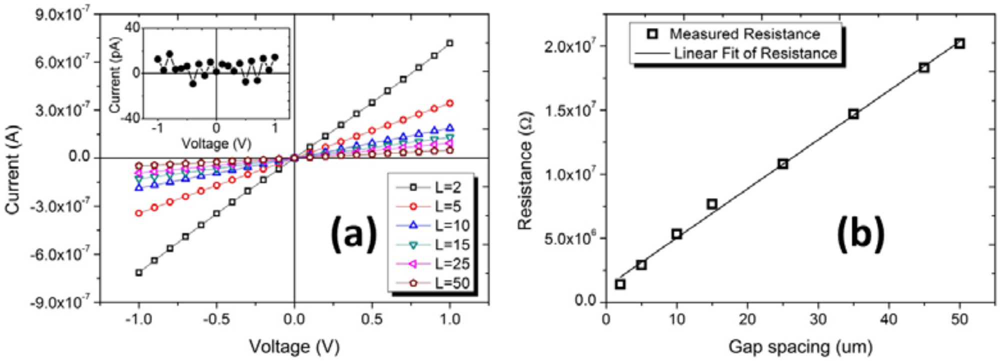

Figure 4.7. (a) *I-V* characteristics measured for a 0.65 nm TiN layer (passivated by 15 nm a-Si) on the structures with *W*=30 μm and *L* varied from 2 μm to 50 μm, and (b) the total measured resistance *R* plotted versus gap spacing *L*. The inset in (a) shows the *I-V* characteristic of the a-Si passivation layer only, measured in the same voltage range.

The resistivities obtained from the linear method are in good agreement with the ones measured by CTLM for the same film thickness. For example, for a 2.5 nm TiN film, the linear structure gives a resistivity of 410 μΩ·cm, which is nearly identical to the value of 400 μΩ·cm obtained by CTLM.

4.1.4.4. Comparison between the optically and electrically obtained resistivity

Fig. 4.8 compares the resistivity values determined by SE (squares) and the electrical test structures (triangles) for TiN films in the thickness range 0.65–20 nm. SE measured the resistivity at the center of the wafer whereas the electrical test structures were located around the center at mm-range distance (see the inset in Fig. 4.8). As ALD offers high thickness uniformity, there is a negligible influence of structure positioning on the layer thickness (see Ref. [11]).

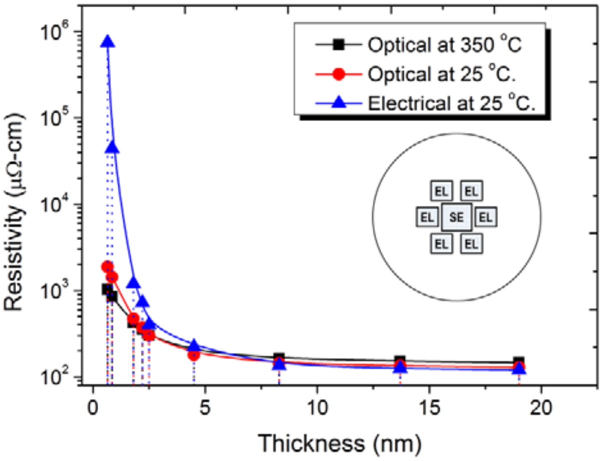

Figure 4.8. A comparison of the resistivity obtained by optical (squares and circles) and electrical (triangles) methods. The inset shows the positions for optical (SE) and electrical (EL) measurements.

Fig. 4.8 shows that, for the films thicker than 4 nm, the resistivity values obtained from the two methods are nearly identical. However, the resistivity diverges markedly for films thinner than 4 nm. The values obtained from the electrical measurements are significantly higher than the corresponding SE results. For the thinnest TiN film, the electrically measured resistivity is hundred times higher than the optically measured value (i.e. 747000 μΩ·cm compared to 1030 μΩ·cm for 0.65 nm TiN film). This considerable divergence can be due to the scattering effects that contribute to the resistivity measured by the two techniques. SE determines the resistivity on the basis of measuring the conduction electron concentration and scattering of the electrons caused by the light-electron interaction. However, electrons can only move locally under the electric field of the incident light. This results in a minor contribution of the scattering effects to the resistivity. In contrast, the resistivity obtained by direct electrical measurements reflects the large-scale scattering of electrons as they travel over a longer distance from one electrode to the other electrode. This consequently increases the scattering effects of electrons and hence the resistivity. The good agreement of the resistivity obtained by both techniques for films thicker than 4 nm indicates that for thick films the contribution of grain boundaries and surface morphology is less significant, and the resistivity is predominantly determined by the inherent properties of the material (conduction electron concentration and bulk carrier mobility). Therefore, we attribute the increasing difference of the resistivity with decreasing film thickness mainly to the increasing role of grain boundary and interface scattering.

To note, the SE measurements were carried out at the deposition temperature (350 °C) whereas the electrical measurements were performed at room temperature. The divergence of the resistivity shown in Fig. 4.10 can be partially attributed to the difference of the measurement temperature, which is, in other words, expressed by the temperature coefficient of resistance (TCR) of the material. We therefore electrically determined the TCR of TiN for different film thicknesses and recalculated the values of the optically measured resistivity at room temperature (the circles in Fig. 4.8). The results show the insignificant impact of measurement temperature on the discrepancy illustrated in Fig. 4.8 (i.e. between the circles and the triangles).

4.1.5. Conclusions

In summary, we determined the resistivity of ultra-thin TiN films in the thickness range 0.65–20 nm by spectroscopic ellipsometry and from electrical test structures. The results show that the resistivity increases significantly with decreasing film thickness. We compared the resistivity values obtained by the optical and electrical techniques. For films thicker than 4 nm, the comparison shows good agreement between the two methods. However, for films thinner than 4 nm, a significant difference is found which increases with decreasing film thickness. We attribute the difference mainly to the scattering effects at interfaces and grain boundaries which cannot be fully taken into account by SE measurements. The difference in measurement temperature has no significant impact on the results.

The electrical characterization shows a strong influence of native oxidation on the electrical properties of unpassivated TiN films. For ultra-thin layers (i.e. $t < 5$ nm), this oxidation can result in non-linear *I-V* characteristics. Measurements on passivated films (using a 15 nm a-Si layer) show linear *I-V* curves and the resistivity is obtained down to 0.65 nm of film thickness. The impact of native oxidation on the electrical properties and the importance of surface passivation is discussed further in Chapter 5.

4.2. Temperature coefficient of resistance of ultra-thin TiN films

4.2.1. Introduction

The resistivity ρ and hence the electric resistance R of a conductor are temperature-dependent [12]:

$$R = R_0\left(1 + \alpha T\right) \tag{4.9}$$

where R_0 is the resistance of the conductor at the temperature T = 0 ^{o}C and α is the temperature coefficient of resistance (TCR). In metals, the values of α are positive: the resistance increases linearly with temperature due to the increasing electron-phonon scattering [8, 13]. However, it is well-known that in semiconductors and semimetals TCR values are commonly negative [13-14] because the carrier concentration increases with temperature.

TiN is commonly known as a metallic material with a positive TCR [3, 4]. In this section we demonstrate that ultra-thin TiN films can exhibit a negative TCR. We found that the TCR changes its sign from positive to negative when the film thickness decreases; this occurs at about 2.5 nm. We attribute the change to the metal-semimetal transition (MST) in ultra-thin TiN films. Above the MST, the films show metallic behavior with resistivity in the range of a few hundred μΩ·cm and a positive TCR. Below the MST, the TCR values are negative, representing semimetallic state accompanied by a steep increase of resistivity.

4.2.2. Experimental

We employed the linear test structures described in Section 4.1 to study the electrical conduction behavior. The electrical measurements were carried out for 0.65–20 nm thick films, in the temperature range 25–150 ^{o}C using a Cascade Microtech low-leakage manual probe station.

4.2.3. Results and discussion

Fig. 4.9 (a) shows *I*-*V* characteristics of a passivated 4.5 nm TiN measured in the temperature range 25–150 °C and the corresponding resistance-temperature (*R*-*T*) graph (Fig. 4.9 (b)). The resistance increases linearly with temperature, meaning a positive TCR. This is well-known for metals and represents the increasing interaction of electrons with phonons (i.e. lattice vibrations) with temperature. From the linear fit of the *R*-*T* graph, a TCR value of 2.37×10^{-4} K^{-1} is obtained.

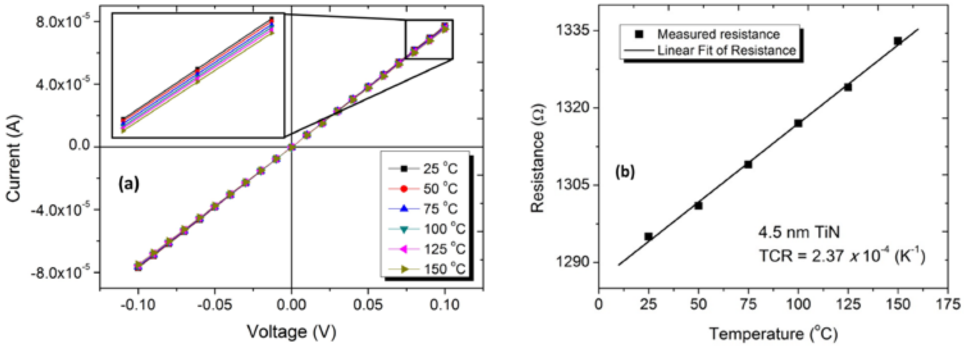

Figure 4.9. *I*-*V* characteristics of a passivated 4.5 nm TiN film measured at different temperatures (a) and the corresponding resistance plotted versus temperature (b). The inset in (a) shows a zoomed-in view.

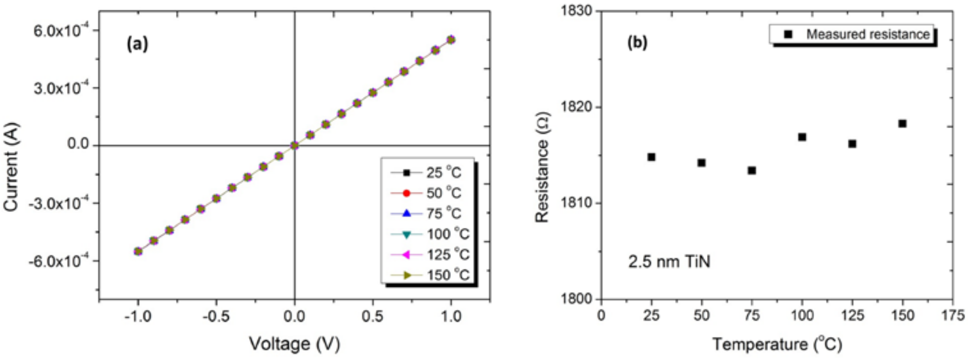

Figure 4.10. *I*-*V* characteristics of a passivated 2.5 nm TiN film measured at different temperatures (a) and the corresponding resistance plotted versus temperature (b).

Measurements on a passivated 2.5 nm thick film show linear *I*-*V* curves (Fig. 4.10 (a)), but the resistance remains nearly unchanged while varying the temperature (Fig. 4.10 (b)).

For a 2.2 nm layer (passivated), the *I-V* characteristics remain linear, but the resistance decreases linearly with increasing temperature (Fig. 4.11 (a), (b)). A negative TCR of -1.33×10^{-4} K^{-1} is obtained for this layer. The negative TCR represents non-metallic properties; the material can be either in a semimetallic or semiconducting state. Our study of the electric field effect (part 4.3 of this chapter) indicates the semimetallic state, where both holes and electrons contribute to the electrical conduction. The carrier density increases with temperature and hence the conductivity increases.

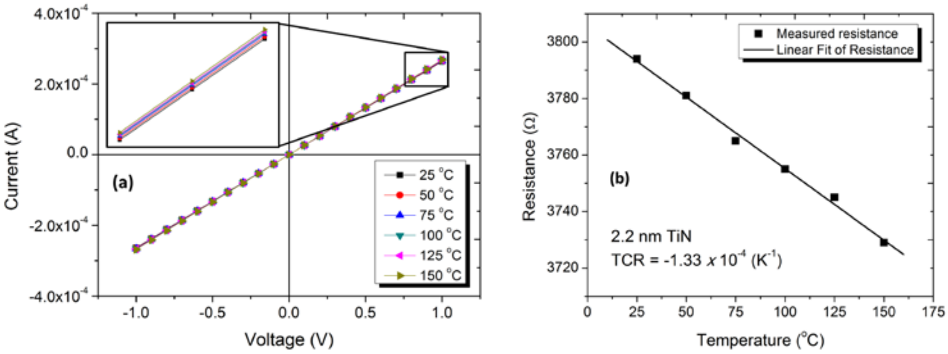

Figure 4.11. *I-V* characteristics of a passivated 2.2 nm TiN film measured at different temperatures (a) and the corresponding resistance plotted versus temperature (b).

Further decrease of the film thickness shifts the TCR to more negative values. For a passivated 0.65 nm TiN film, the *I-V* curves remain linear, and the obtained TCR is more than one order of magnitude larger than that of the 2.2 nm film (i.e. -2.54×10^{-3} K^{-1} compared to -1.33×10^{-4} K^{-1}). The influence of temperature is clearly visible in the *I-V* characteristics (Fig. 4.12 (a)).

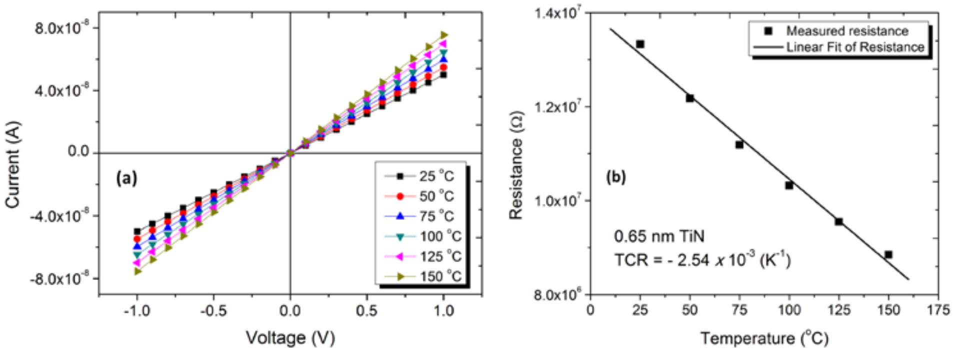

Figure 4.12. *I-V* characteristics of a passivated 0.65 nm TiN film measured at different temperatures (a) and the corresponding resistance plotted versus temperature (b).

The thickness-dependence of TCR of ultra-thin TiN films is shown in Fig. 4.13 (circles). With decreasing film thickness, the TCR changes its sign from positive to negative at a thickness around 2.5 nm. It is important to note that TiN films with a thickness of 0.65 nm and higher already contain at least three continuous monolayers (Chapter 3, [15]). This rules out the possibility of discontinuous-continuous transition at 2.5 nm. In addition, for a discontinuous film, one can expect a tunneling electrical conduction mechanism which would result in non-linear behavior in the *I-V* characteristics. However, in our measurements, we increased the applied voltage up to ±10 V still without noticeable deviation from linearity. We ascribe the films with zero TCR to the metal-semimetal transition (MST) in ultra-thin TiN, which is accompanied by a significant increase of the resistivity (Fig. 4.13, squares).

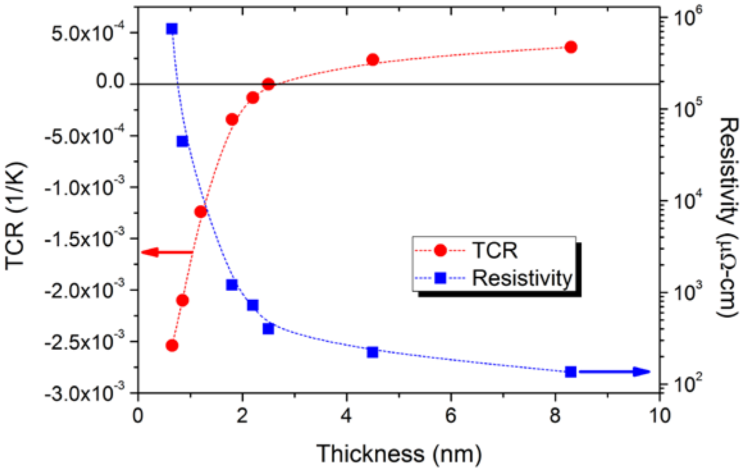

Figure 4.13. Thickness-dependence of TCR (circles) and electrically-measured resistivity (squares; correspond to triangles in Fig. 4.8) of ultra-thin TiN films.

The mechanism of the MST suggested for ultra-thin TiN films is unknown yet. Our interpretation is based on the band structure of TiN reported in the literature with the remark that the band structure can be different for ultra-thin films with respect to the bulk state [16-17]. In the metallic state, the Fermi level is positioned in the conduction band. The semimetallic state appears as the Fermi level is located in the overlap region between the conduction and the valence bands. In general, this can be caused by quantum confinement effects and stress in ultra-thin films. The influence of stress on the MST was for example observed for thin V_2O_3 films [18].

In our case, as one of the possible explanations, we attribute the transition to the increasing influence of oxygen in the material as the film thickness decreases. The oxygen originates from the initial growth of TiN on SiO_2 substrate. In this case, the first adsorbing $TiCl_4$ precursor must react with the OH-groups on the surface. As a consequence, the first monolayer is expected to contain Ti-O bonds. The electron properties in Ti-O groups are different from Ti-N groups since the valence of oxidized Ti can be either IV (in TiO_2) or II (in TiO) whereas it is III in TiN. The percentage of the Ti-O bonds in the film increases with decreasing film thickness and can reach, for example, 30% in a 0.65 nm TiN layer. The 30% represents one Ti-O monolayer of the 3-monolayer structure. The impact of oxygen on the electronic properties should increase as the film thickness decreases. For example, the influence of oxygen on electronic properties (Fermi level position and the energy gap) of GaN has been reported in the literature [19].

4.2.4. Conclusions

In summary, we determined the TCR values of ultra-thin continuous TiN films down to sub-nanometer range by electrical measurements. A TCR of 3.6×10^{-4} K^{-1} is obtained for an 8.3 nm TiN film. The TCR decreases with reducing film thickness. At a thickness of about 2.5 nm, the measurements show a virtually zero TCR. Below 2.5 nm, the TCR becomes negative and a value of -2.54×10^{-3} K^{-1} is obtained for a 0.65 nm TiN film. We preliminarily ascribe this effect to the metal–semimetal transition which occurs at a film thickness of about 2.5 nm and is attributed to the role of oxygen in the films. This preliminary conclusion is supported by the study on the field effect in ultra-thin TiN films to be presented in the next part of this chapter.

4.3. Electric field effect in ultra-thin TiN films

4.3.1. Introduction

The field effect refers to the change of the electrical conductivity of a material by applying an external electric field [20]. In semiconductors, the number of carriers (i.e. electrons and holes) that can respond to the applied field is small and the field can penetrate quite far into the material. This penetration causes the redistribution of carriers and changes the conductivity of the semiconductor along the field penetration depth. However, in metals with significantly higher electron density, when an electric field is applied, it creates a surplus of induced charges screening the penetration and reducing the depth. Therefore, to observe the field effect in metals, the applied field must be sufficiently high and the film thickness must be comparable to the field penetration depth.

The conductivity in a thin metallic film is defined as [21]

$$\sigma_1 = q\mu_1 N_1 \tag{4.10}$$

where q is the elementary charge, N_1 is the conduction electron concentration and μ_1 is the conduction electron mobility. For a film thickness t, the number of electrons per unit area of the film is $n=N_1t$. Therefore, the conductivity as a function of the film thickness can be written as

$$\sigma_1 = q\mu_1 \frac{n}{t} \tag{4.11}$$

where $\mu_1 = k\mu_0$, μ_0 is the conduction electron mobility in the bulk material, the factor k ($0 < k < 1$) accounts for the decrease of electron mobility due to the size effect [21]. From Eq. (4.11), the change of the conductivity can be written as

$$\delta\sigma = \left(\frac{\partial\sigma}{\partial\mu}\right)_{n,t} \delta\mu + \left(\frac{\partial\sigma}{\partial n}\right)_{\mu,t} \delta n + \left(\frac{\partial\sigma}{\partial t}\right)_{\mu,n} \delta t \tag{4.12}$$

where $\delta\sigma$ is the total change of the conductivity due to the influence of the perpendicular electric field. $\left(\frac{\partial\sigma}{\partial\mu}\right)_{n,t} \delta\mu$ and $\left(\frac{\partial\sigma}{\partial n}\right)_{\mu,t} \delta n$ represent the field effect caused by the change of electron mobility $\delta\mu$ and the change of the number of conduction electrons per unit area δn, respectively. As the physical film thickness cannot be affected by the electric field, δt is therefore the change of effective thickness (i.e. the actual *channel* depth for the current to flow) and $\left(\frac{\partial\sigma}{\partial t}\right)_{\mu,n} \delta t$ represents the channel size change. Eq. (4.12) suggests that any observed change in the conductivity due to the perpendicular electric field (electric field effect) should be related to the change of electron mobility, number of conduction electrons, and effective film thickness.

Films above the MST exhibit a metallic behavior since the Fermi level is positioned in the conduction band. However, below the MST threshold, films show semimetallic characteristics due to the overlap between the conduction and the valence bands. Fig. 4.14 shows the band structure of bulk TiN as reported by Allmaier et al. [17]. It is important to note that for ultra-thin films, the band structure can be different due to the quantum confinement effects. However, we adopt this band structure to *qualitatively* describe the electric field effect for thin TiN films in their semimetallic state. In the semimetallic state, the Fermi level is positioned in the region between the top of the valence band at the Γ point and the bottom of the conduction band at the X point. This implies that the current is conducted by both holes and electrons and the field effect is expected to differ from that in the metallic state.

The conductivity in a semimetallic state is described as [22]

$$\sigma = 1/\rho = q\left(n_e\mu_e + n_h\mu_h\right) \tag{4.13}$$

where σ and ρ are the conductivity and resistivity, respectively. n_e, n_h and μ_e, μ_h are the concentrations and the mobilities, respectively; e stands for electrons and h - for holes. Note that n_e and n_h are interdependent parameters related through a common value of the Fermi level ε_F [22].

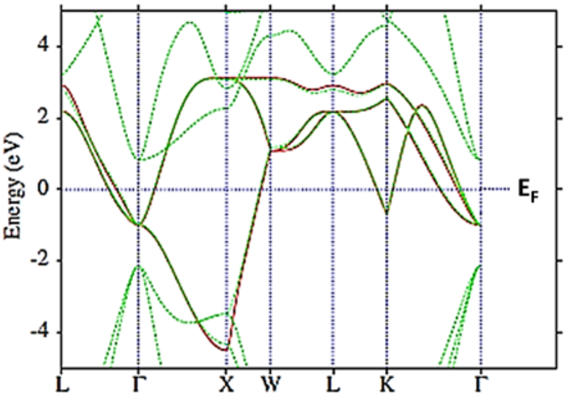

Figure 4.14. Band structure of bulk TiN (Copied from Ref. [17]). The zero energy corresponds to the Fermi level E_f.

In the presence of the perpendicular electric field, extra charges are induced. This consequently shifts the Fermi level position and changes the carrier concentrations. The film conductivity is now written as

$$\sigma_1 = q\left(\left[n_e + \Delta n_e\right]\mu_e + \left[n_h + \Delta n_h\right]\mu_h\right) \tag{4.14}$$

where Δn_e and Δn_h are the changes in concentration of electrons and holes, respectively. Δn_e, $\Delta n_h > 0$ if more carriers are generated. The product $\Delta n_e \cdot \Delta n_h$ is always negative as the increase of electron concentration results in the decrease of hole concentration, and vice versa. Assuming that $\Delta n_e = -\Delta n_h = \Delta n$, the change in conductivity upon changing the carrier concentration can be written as

$$\Delta\sigma = \sigma_1 - \sigma = q\Delta n(\mu_e - \mu_h) \tag{4.15}$$

Since $\mu_e > \mu_h$, the increase of electron concentration (and hence the decrease of hole concentration) would increase the conductivity of the film. Therefore, in this regime, the change of the conductivity is mainly attributed to the difference in the mobility of the carrier types.

The relative shift of the Fermi level can lead to two extremes: it can (i) rise to above the top of the valence band or (ii) lower to below the bottom of the conduction band. Respectively, the major carriers in the film will change from both electrons and holes to either electrons or holes only. This must impact the film conductivity.

4.3.2. Experimental

The used test structures are shown in Fig. 4.15. The fabrication is described in Section 4.1. Importantly, all TiN films were passivated by 15 nm thick a-Si to prevent the native oxidation. It should be mentioned that the substrate is highly doped Si. After the fabrication of the structures on the front side, the back side of the wafer (substrate) was covered with 500 nm Al layer to realize a back gate contact for field effect measurements. Before sputtering Al, the oxide on the back side of the substrate was removed in 1% HF to ensure good contact between Al and Si.

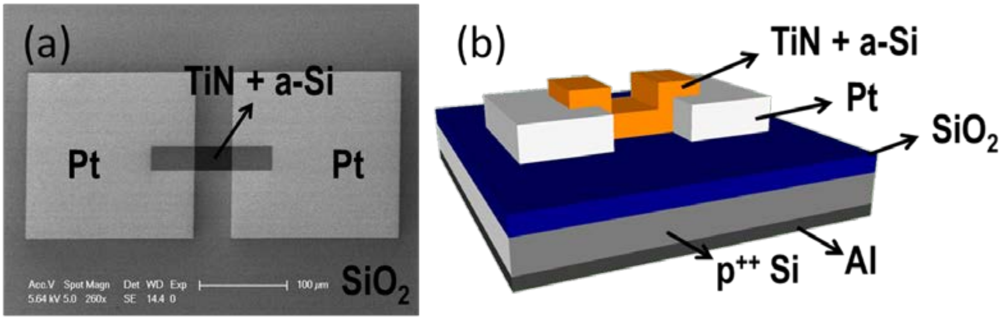

Figure 4.15. Top-view SEM image (a) and 3D drawn view (b) of the test structure for studying field effect. The Al back-side gate is shown.

The electrical measurements were carried out using either a Karl-Suss PM8 or a Cascade Microtech low-leakage manual probe station. Coating a primer layer on the surface prior to the measurements ensured a negligible surface leakage current. The low-temperature measurements down to 4.2 K were carried out using a Janis ST-500-1-(4CX) probe station.

4.3.3. Results and discussion

4.3.3.1. Electric field effect in TiN films thicker than 2.5 nm (metallic state)

The drain current (I_{ds}) and drain voltage (V_{ds}) are defined as the current and the voltage between the two top electrodes, respectively. The applied voltage on the backside gate is denoted as V_{gs}.

The I_{ds}-V_{ds} characteristics of films with thicknesses of 2.5 nm and 4.5 nm are shown in Fig. 4.16. Linear curves were obtained, indicating ohmic contact between TiN and Pt and ohmic behavior of the thin films. The measured resistivity values were 410 μΩ·cm and 220 μΩ·cm, respectively.

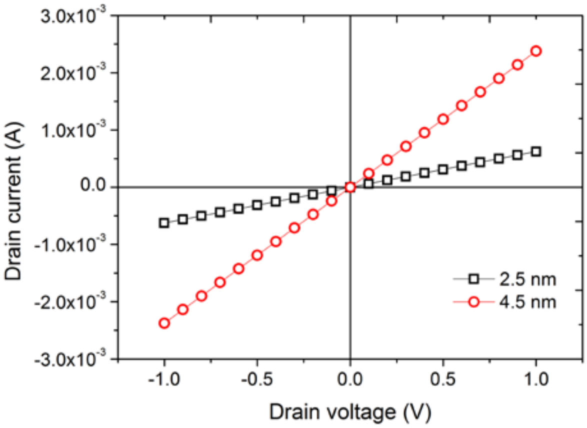

Figure 4.16. I_{ds}-V_{ds} characteristics at V_{gs} = 0 V of TiN films with a thickness of 2.5 nm (squares) and 4.5 nm (circles).

The I_{ds}-V_{gs} characteristics, shown in Fig. 4.17, illustrate the influence of the external perpendicular electric field (created by applying a voltage to the Al gate) on the film conductivity. In these measurements, V_{ds} is set at 1 V and V_{gs} is swept from –50 to +50

V and back. To describe the field effect, we define the ratio $\Delta I/I_0$ reflecting the relative change of current due to the external field

$$\frac{\Delta I}{I_0} = \frac{I_{V+} - I_{V-}}{I_0} \tag{4.16}$$

where I_0 is the current at $V_{gs}= 0$; I_{V+} and I_{V-} are the currents at the maximum values of the positive and negative applied gate voltages, respectively. For a 4.5 nm TiN layer, a ratio $\Delta I/I_0$ of 3.8×10^{-4} is found, which increases to 6.9×10^{-4} for a 2.5 nm layer.

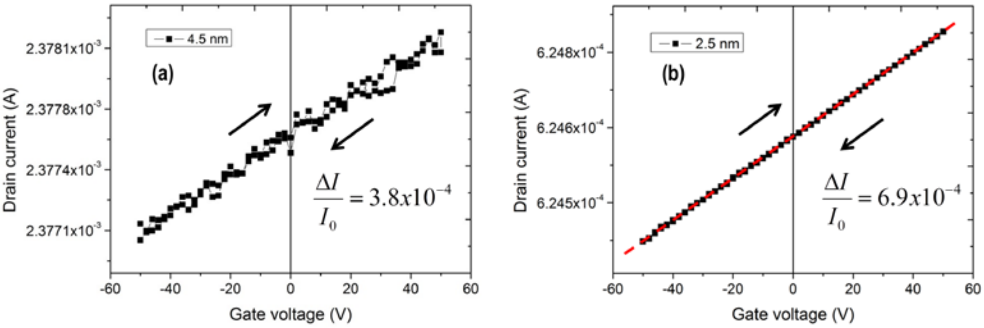

Figure 4.17. I_{ds}-V_{gs} characteristics of TiN films with thickness of 4.5 nm (a) and 2.5 nm (b). The arrows show sweeping directions of the gate voltage. The V_{ds} is fixed at 1 V.

It is important to note that the *I-V* characteristics plotted in Fig. 4.17 show a linear increase of drain current with increasing gate voltage. The change of current caused by the perpendicular field is attributed to the change of (i) conduction electron concentration, (ii) electron mobility, and (iii) effective film thickness. Below we describe the contribution of each component to the total field effect.

The carrier concentration effect. A strong penetration of the external electric field will raise or lower the conduction band edge in the region of the potential minimum [13]. A positive gate voltage will lower the conduction band edge (Fig. 4.18) and therefore relatively shift the Fermi level up with respect to the band edges. This will increase the conduction electron concentration and therefore the conductance. In contrast, a negative gate bias will raise the conduction band edge which decreases the conductance.

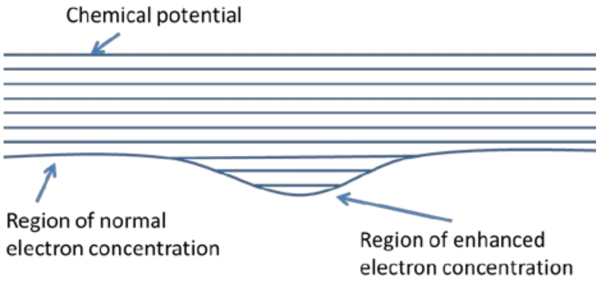

Figure 4.18. A local deformation of the conduction band edge due to a positive applied voltage (redrawn from Ref. [13]).

The mobility change effect. As mentioned above, the field penetration causes the deformation of the conduction band edge. The deformation (schematically depicted in Fig. 4.18) can additionally affect the mobility of electrons as a result of either increase or decrease electron effective mass. As a consequence, the conductivity of the film is influenced.

The effective film thickness effect. The effective film thickness refers to the width (depth) of the channel in which the actual carriers are flowing. The perpendicular external field causes the carrier redistribution along the field lines. This consequently changes the channel size and therefore the conductance.

4.3.3.2. Electric field effect in TiN films thinner than 2.2 nm (semimetallic state)

In the semimetallic state, the Fermi level is positioned in the overlap region between the conduction and the valence bands. In this state, the conduction is maintained by both electrons and holes. Therefore, the field effect below the MST threshold will also depend on the change in the concentration of both types of carriers.

Fig. 4.19 shows the I_{ds}-V_{ds} characteristics of TiN films in semimetallic state. The inset shows the characteristic of the thinnest film (i.e. 0.65 nm). To note, the growth of TiN in our case follows the Stranski–Krastanov model [15] and the film with thickness of 0.65 nm is already continuous (see Chapter 3). As presented above, the I_{ds}-V_{gs} characteristics measured for TiN films in the metallic state ($t \geq 2.5$ nm) showed a linear behavior. However, the I_{ds}-V_{gs} curves obtained for TiN films in the semimetallic state exhibit two different linear regimes (Fig. 4.20). These two linear regimes merge at a gate bias of about +10 V where a kink is observed. The appearance of the kink becomes more pronounced with decreasing film thickness.

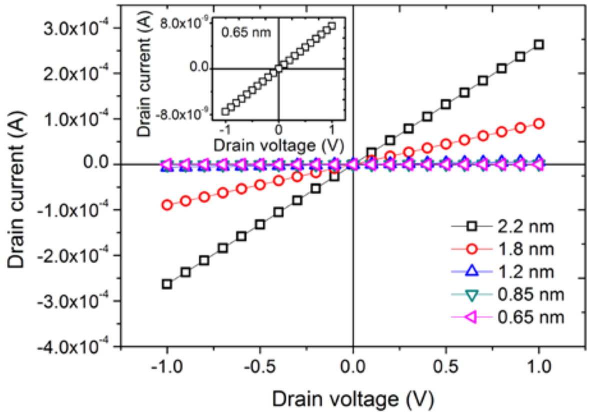

Figure 4.19. I_{ds}-V_{ds} characteristics of TiN films in semimetallic state ($t \leq 2.2$ nm) measured at $V_{gs} = 0$. The inset shows I_{ds}-V_{ds} obtained for a 0.65 nm thick film.

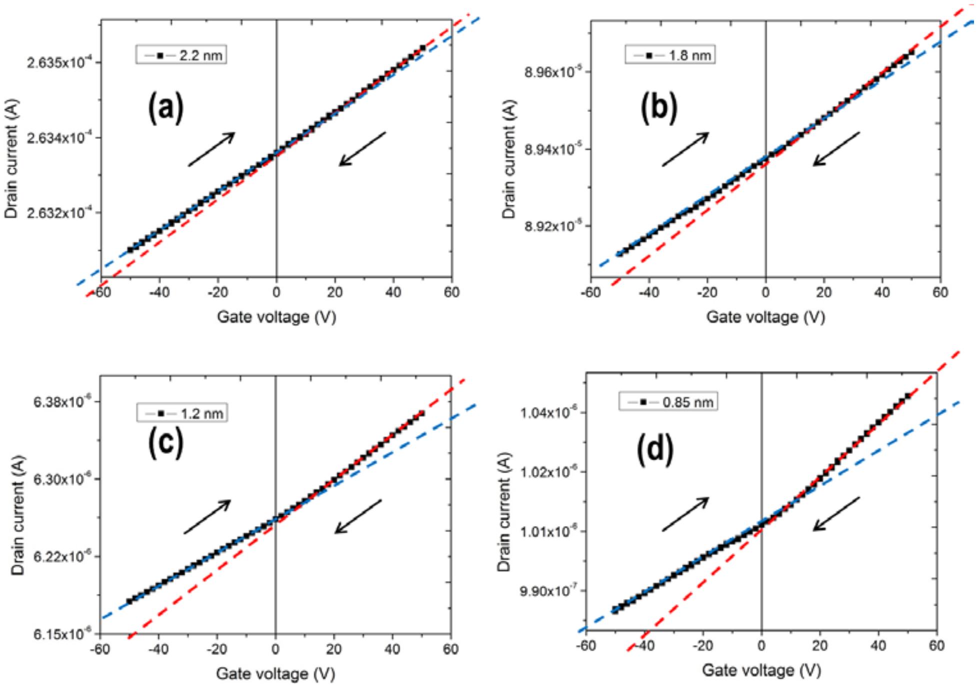

Figure 4.20. I_{ds}-V_{gs} characteristics of TiN films with thicknesses of (a) 2.2 nm, (b) 1.8 (nm), (c) 1.2 nm and (d) 0.85 nm. The dashed lines are drawn to distinguish the two linear regimes.

We use the ratio $\Delta I/I_0$ given by Eq. 4.16 to quantify the field effect. One can see that the field effect increases drastically with decreasing film thickness (Fig. 4.21). A value of 1.7×10^{-3} (0.17%) is obtained for a 2.2 nm TiN; the field effect increases by 2 orders of magnitude (up to 2.2×10^{-1}, i.e. 22%) for a 0.65 nm TiN layer.

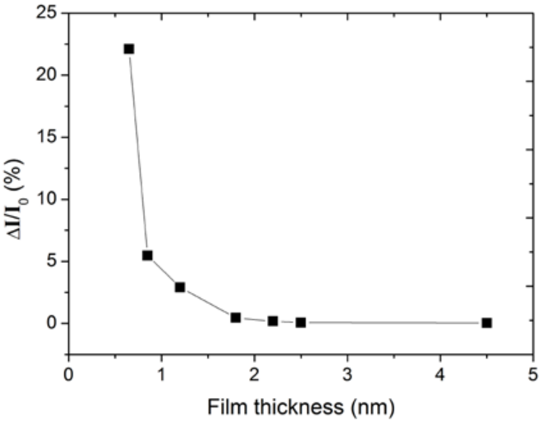

Figure 4.21. Thickness-dependence of the field effect in ultra-thin TiN films. The measurements were carried out in the gate voltage range (–50, 50) V (Fig. 4.20).

In this work, we apply the energy band diagram reported in the literature for thick films (Fig. 4.14) [17] to describe the observed field effect *qualitatively*. We note that the band structure can be different for ultra-thin TiN films. The band diagram around the center of the Brillouin zone is schematically redrawn in Fig. 4.22. In the metallic state (t > 2.5 nm), the Fermi level is positioned entirely in the conduction band (Fig. 4.24 (a)). At the MST threshold ($t \approx$ 2.5 nm), the Fermi level coincides with top of the valence band (Fig. 4.24 (b)). In the semimetallic state (t < 2.5 nm), the Fermi level crosses both valence and conduction bands (Fig. 4.24 (c)).

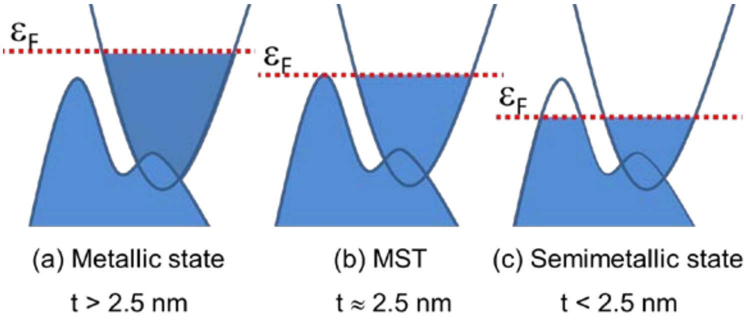

Figure 4.22. Suggested band diagram of ultra-thin TiN in different states: Metallic (a), metal–semimetal transition threshold (b) and semimetallic (c). The band diagram is redrawn from [17] for the center of the Brillouin zone around Γ-X points in Fig. 4.14.

The field effect observed in Fig. 4.20 can be interpreted based on the band diagrams schematically shown in Fig. 4.22. As the film is thinner than 2.5 nm, the band diagram changes to the one shown in Fig. 4.22 (c). At zero gate bias, according to the suggested Fermi level position, both holes and electrons are contributing to the conduction. Applying a positive gate bias will result in the increase of electron concentration and the decrease of hole concentration and, accordingly shifts the Fermi level upwards [22]. According to Eq. 4.15, this should result in the increase of conductivity. The latter is demonstrated by the *I*-*V* characteristics shown in Fig. 4.20 where the positive bias enhances the current. The appearance of the kink at about +10 V can be attributed to the change of the major carrier type. Namely, if the Fermi level relatively shifts upwards with increasing gate voltage, it can eventually reach the top of the valence band. From this point, only electrons can contribute to the conduction. The further increase of gate bias will result in the increase of conduction electron concentration. Moving from hole-electron to only-electron conduction consequently changes the field effect behavior which can be observed by the appearance of the kinks.

Let us now discuss on the negative gate bias effect. Applying a negative gate voltage will lead to the increase of hole concentration and the decrease of conduction electron concentration and therefore lowers the Fermi level. This results in the decrease of conductivity. As the Fermi level continues lowering, there is a possibility that (at a high bias) it can reach the bottom of the conduction band. Accordingly, the carrier types will change from electrons and holes to holes only. In this case, one can expect a change in the field effect characteristics. From this point, further decreasing gate voltage will increase hole concentration which accordingly increases the conductivity of the film.

The electron-only, electron-hole, and hole-only conduction regimes are demonstrated by the I_{ds}-V_{gs} characteristic measured for a 0.65 nm TiN film. The three regimes are indicated in Fig. 4.23. In the first regime (V_{gs} > 10 V), only electrons contribute to the conduction in the film. The conduction electron concentration, and thus the current increase with gate bias. In the second regime (-47.5 V < V_{gs} < 10 V), both holes and electrons contribute to the conduction. The conductance of the film decreases while going to more negative gate bias as electrons are gradually replaced by holes. The interplay between the carrier types is reflected by the non-trivial shape of the curve. In the third regime (V_{gs} < -47.5 V), only holes contribute to the conduction. Further decreasing gate bias increases the hole concentration and hence the conductivity. The latter is clearly seen in the inset.

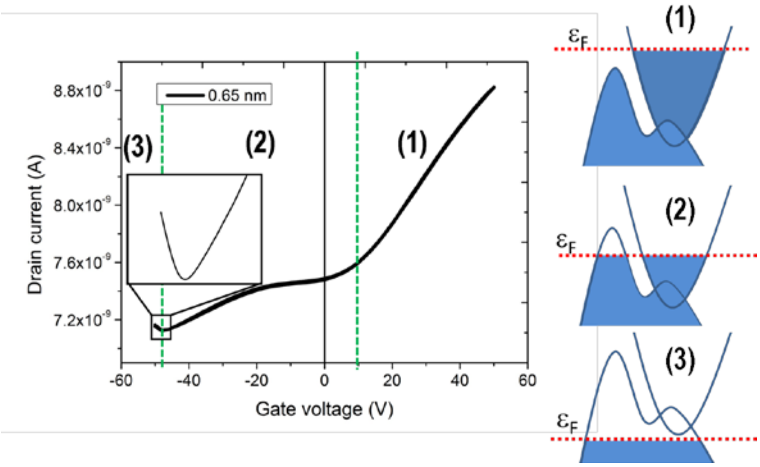

Figure 4.23. Field effect in a 0.65 nm TiN. The I_{ds}-V_{gs} characteristic is divided into three regimes which reflect the corresponding Fermi level position for (1) electron-only, (2) hole-electron, and (3) hole-only conduction. The inset shows the zoomed in transition between the hole-electron and hole-only conduction.

In section 4.2, we report our observation on the positive-negative TCR transition of TiN films as the film thickness decreases. We ascribe this effect to the metal-semimetal transition in TiN occurring at a thickness of about 2.5 nm. This conclusion is now supported by the results of the field effect study. The semimetallic state of ultra-thin TiN films (i.e. $t \leq 2.2$ nm) is additionally indicated by the existence of the hole and electron conduction of the films, especially the hole-only conduction observed for the 0.65 nm TiN film (the third regime in Fig. 4.23). The MST can be attributed to the quantum confinement effects and stress in ultra-thin films, and the increasing role of oxygen which originates from the initial growth of TiN on SiO_2 substrate. This is discussed in Section 4.2.

4.3.3.3. Temperature-independent field effect

The influence of temperature was studied in the temperature range of 4.5–375 K. The results show that the field effect is hardly dependent on temperature (Fig. 4.24). This additionally confirms the film continuity because the electrical conduction is not thermally activated. For a discontinuous film, the field effect is reported to be small above room temperature but becomes of increasing magnitude at lower temperatures [23-24]. This is due to the hopping (tunneling) conductance mechanism between separated parts (grains, islands) of the film. To note, the applied gate voltage range used in Fig. 4.24 was between –30 and 40 V, i.e. lower than the range explored in Fig. 4.23. This results in the lower ΔI/I_0 values.

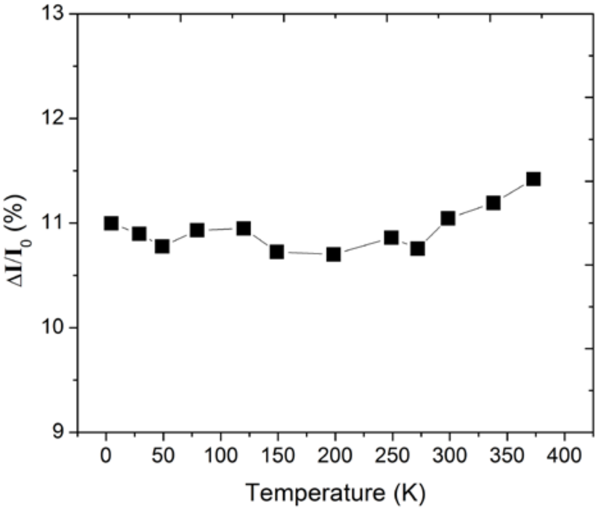

Figure 4.24. Temperature-independence of the field effect measured for a 0.65 nm TiN film. The measurements were carried out in the temperature range of 4.5–375 K under the applied gate voltage range of (–30, 40) V.

An important remark is that, although I_0 increases with temperature (negative TCR), the ratio ΔI/I_0 hardly changes. This indicates that ΔI varies with the same rate as I_0. This observation can be used to further understand the conduction mechanism.

4.3.3.4. Influence of the passivation layer

In order to examine the influence of the a-Si passivation layer on the measured electrical conductance, we replaced this layer by an aluminum nitride (AlN) film. The AlN was grown by ALD technique using TMA and NH_3 precursors at 350 ^{o}C in the same reactor, directly after the TiN ALD and without vacuum break.

Fig. 4.25 (a) shows the I_{ds}-V_{ds} characteristics of a 1.8 nm thick TiN film passivated by an a-Si (squares) or an AlN (circles) layer. At the same voltage, the measured current is slightly higher for TiN with AlN passivation. This is attributed to the thickness variation (reproducibility) of TiN layers from one sample to the other. The TiN layer can be thicker for the AlN-passivated sample. The I_{ds}-V_{gs} characteristic for the AlN-passivation sample is shown in Fig. 4.25 (b). The obtained field effect for this sample is 0.2 %, which is smaller than that of the 1.8 nm TiN film with a-Si passivation (0.43%, Fig. 4.20 (b)). The difference is consistent with the thickness-dependent field effect shown in Fig. 4.21 (i.e. field effect decreases with increasing film thickness).

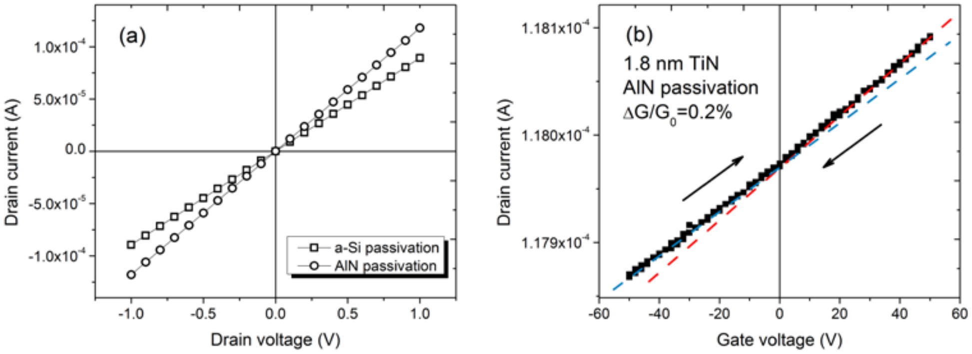

Figure 4.25. (a) I_{ds}-V_{ds} characteristics of 1.8 nm thick TiN films with 15 nm a-Si passivation (squares) and 15 nm AlN passivation (circles) measured at V_{gs} = 0; (b) I_{ds}-V_{gs} characteristic of 1.8 nm TiN with 15 nm AlN passivation. The I_{ds}-V_{gs} characteristic of equally-thick TiN with a-Si passivation is shown in Fig. 4.20 (b).

From obtained results, we conclude that both a-Si and AlN passivation layers have no significant influence on the electrical properties of underlying TiN films. However, our electrical measurements show a degradation of the AlN-passivated sample after a few weeks of exposure to air, as illustrated in Fig. 4.26. In contrast, no degradation is observed for the sample with a-Si passivation even after months (see Section 5.3.1, Chapter 5). This is attributed to the difference in microstructure of a-Si and AlN layers. The XRD characterization shows a polycrystalline texture of the AlN. When exposed to air, the film is oxidized. The grain boundaries of AlN are favorable for the slow-but-steady diffusion of oxidants (e.g. O_2, H_2O) that can eventually reach and oxidize the TiN layer, causing the degradation. This degradation is similar to the effects further demonstrated in Chapter 5, which are caused by the native oxidation of TiN. As a passivation layer, a-Si is a good material because it forms the dense native oxide on top that prevents further penetration of oxidants towards the TiN. Therefore, we emphasize that a-Si is an ideal choice to passivate TiN.

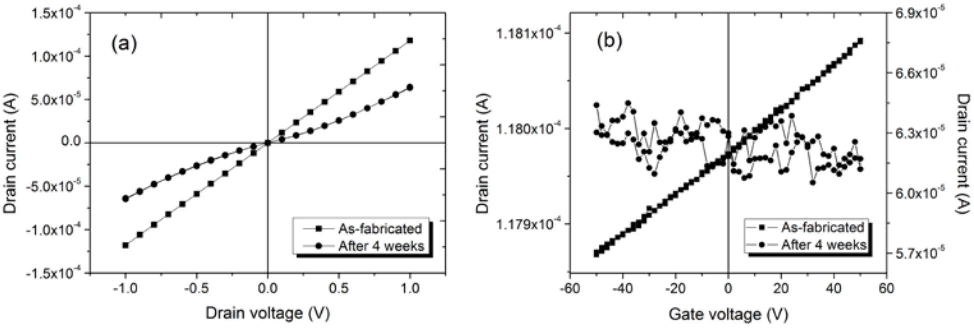

Figure 4.26. I_{ds}-V_{ds} (a) and I_{ds}-V_{gs} (b) characteristics of a 1.8 nm TiN film passivated by a 15 nm AlN layer, measured as-fabricated and after 4 weeks being exposed to air. The results indicate the degradation of the TiN layer after 4 weeks: the I_{ds}-V_{ds} curves become non-linear and no field effect can be observed.

4.3.4. Conclusions

The results of the field effect study indicate that ultra-thin TiN films can appear in a semimetallic state. This confirms our preliminary conclusion based on the positive-negative TCR transition made in Section 4.2.

We have observed the electric field effect in ultra-thin TiN films in their metallic and semimetallic states and possible explanations of the field effect have been given. For films in the metallic state, the field effect is small (in the range of 10^{-4}) and is attributed to possible changes in carrier concentration, effective film thickness, and electron mobility. The changes in carrier concentration and electron mobility might be caused by the deformation of the conduction band edge at the potential minimum under the external electric field. The change in effective film thickness is caused by redistribution of the carriers along the field lines.

In the semimetallic state, a large (and temperature-independent) field effect has been observed. The field effect increases drastically with decreasing film thickness and reaches values up to 22% for a 0.65 nm thick TiN in the gate voltage range of (–50; 50) V. We qualitatively attribute this field effect to the change of carrier concentration and carrier types in the films. According to this model, carrier types in the semimetallic state can vary from both holes and electrons to either electrons only (positive gate bias) or holes only (negative gate bias). The observed temperature-independence of the field effect indicates that the conduction mechanism is not thermally activated. This is an additional confirmation of the formation of continuous TiN films from the very beginning of the ALD process, as reported in Chapter 3.

References

[1] P. Patsalas and S. Logothetidis, *J. Appl. Phys.* **90**, 4725 (2001).

[2] P. Patsalas and S. Logothetidis, *J. Appl. Phys.* **93**, 989 (2003).

[3] E. Langereis, S. B. S. Heil, M. C. M. van de Sanden, and W. M. M. Kessels, *J. Appl. Phys.* **100**, 023534 (2006).

[4] A. W. Groenland, R. A. M. Wolters, A. Y. Kovalgin, and J. Schmitz, *IEEE Trans. Semicond. Manuf.* **25**, 178 (2012).

[5] K. Yokota, K. Nakamura, T. Kasuya, K. Mukai, and M. Ohnishi, *J. Phys. D: Appl. Phys.* **37**, 1095 (2004).

[6] J. H. Klootwijk and C. E. Timmering, *Proc. ICMTS*, **17**, 247 (2004).

[7] G. S. Marlow, and M. B. Das, *Solid State Electron.* **25**, 91 (1982).

[8] N. W. Ashcroft and N. D. Mermin, *Solid State Physics*, Saunders College, Orlando (1976).

[9] P. Patsalas, C. Charitidis, S. Logothetidis, C. A. Dimitriadis, and O. Valassiades, *J. Appl. Phys.* **86** (1999) 5296.

[10] J. J. Yang, M. D. Pickett, X. Li, D. A. A. Ohlberg, D. R. Stewart, and R. S. Williams, *Nature Nanotech.* **3**, 429 (2008).

[11] A. W. Groenland, *Nanolink-Based Thermal Devices: Integration of ALD TiN Thin Films*, PhD. Thesis, University of Twente, (2011).

[12] W. Benenson, J. W. Harris, H. Stocker, and H. Lutz, *Handbook of Physics*, Springer-Verlag, New York (2002).

[13] C. Kittel, *Introduction to Solid State Physics*, 5th ed., Willey, New York (1975).

[14] K. Liu, C. L. Chien, P. C. Searson, and K. Yu-Zhang, *Appl. Phys. Lett.* **73**, 1436 (1998).

[15] H. Van Bui, A. Y. Kovalgin, and R. A. M. Wolters, *ECS J. Solid State Sci. Technol.* **1**, P285 (2012).

[16] V. Ern and A.C. Switendick, *Phys. Rev.* **137**, A1927 (1965).

[17] H. Allmaier, L. Chioncel, and E. Arrigoni, *Phys. Rev. B* **79**, 235126 (2009).

[18] Q. Luo, Q. Guo, and E. G. Wang, *Appl. Phys. Lett.* **84**, 2337 (2004).

[19] K. C. Misha, P. C. Schmidt, S. Laubach, and K. H. Johnson, *Phys. Rev. B* **76**, 035127 (2007).

[20] R. Enderlein, and N. J. M. Horing, *Fundamentals of Semiconductor Physics and Devices*, World Scientific, Singapore (1997).

[21] R. Dimmich, and F. Warkusz, *Thin Solid Films* **79**, 173 (1981).

[22] K. S. Novoselov, A. K. Geim, S. V. Morozov, D. Jiang, Y. Zhang, S. V. Dubonos, I. V. Grigorieva, and A. A. Firsov, *Science* **306**, 666 (2004).

[23] C. A. Neugebauer, and M. B. Webb, *J. Appl. Phys.* **33**, 74 (1962).

[24] A. A. Milgram, and C. Lu, *J. Appl. Phys.* **37**, 4773 (1966).

5

Oxidation of ALD TiN films

This chapter reports on the influence of native oxidation on electrical behavior of thin ALD TiN films. For films thinner than 5 nm, this oxidation changes the I-V behavior from linear to non-linear. This aging effect results in irreversible degradation of TiN. Native oxidation does not influence linearity of the I-V characteristics for films thicker than 5 nm. Nevertheless, it reduces the electrical thickness of TiN.

The kinetics and mechanism of thermal oxidation at elevated temperatures of films with a thickness of 5 and 15 nm are intensively studied. The oxidation in oxygen ambient was carried out directly after the TiN deposition in the same reactor and in situ spectroscopic ellipsometry monitoring was used. We divide the TiN oxidation into four stages and proposed a specific mechanism to describe the behavior.

5.1. Introduction

Although TiN is a hard metallic material with high thermal and chemical stability, TiN films can be oxidized when exposed to oxidizing ambient or air. Sinke et al. [1] found the TiN barrier performance between Si and Al to be improved when TiN was exposed to air prior to Al deposition. However, oxidation is not favorable in CMOS applications where low electrical resistivity of TiN films is required. Most of the studies on the oxidation of TiN were done on sputtered films with a thickness of several tens to hundreds of nanometers [2-5], or more [6-7]. In these studies, air or dry oxygen at atmospheric pressure was used for oxidation. Wet oxidation was also described in the literature [8]. The *ex situ* characterization techniques in the studies on dry oxidation led to different conclusions concerning the oxidation mechanism of TiN. Using X-ray photoelectron spectroscopy, Saha and Tompkins [3] found an intermediate state between TiN and TiO_2 during oxidation. The existence of this intermediate state was also reported in a later study of Hones et al. [5], in which spectroscopic ellipsometry and other complementary analysis techniques were employed. However, the study of Soriano et al. [2] indicated an abrupt interface between TiN and TiO_2 with complete phase separation upon oxidation. Therefore, questions regarding the oxidation mechanism of TiN are still open. To further explore the applications of TiN, the stability and oxidation of TiN films of several nanometers of thickness have to be investigated in detail.

In this chapter, the influence of native oxidation due to exposure to air on electrical properties of thin TiN films is reported in Section 5.3.1. The thermal oxidation behavior of TiN films with a thickness of 5 or 15 nm is intensively studied and presented in Section 5.3.2.

5.2. Experimental

In the dry oxidation of TiN, the temperature of the wafer was adapted (if necessary) after TiN ALD and stabilized in N_2 ambient at a pressure of 10 mbar directly after deposition. Oxygen was introduced at a constant flow of 25 sccm while the total pressure was kept at 10 mbar. The oxidation was performed at various temperatures, i.e. 325 ^{o}C, 350 ^{o}C, 400 ^{o}C and 425 ^{o}C. There was no vacuum break between deposition and oxidation, eliminating the surface oxidation due to exposure of as-deposited TiN films to air.

The oxidation was observed by real-time spectroscopic ellipsometry (SE). Other complementary characterization techniques including X-ray photoelectron spectroscopy (XPS) depth profile, X-ray fluorescence (XRF), X-ray reflectivity (XRR) were employed to characterize the film thickness and composition.

5.3. Results and discussion

5.3.1. Influence of native oxidation on electrical properties of thin TiN films

In Chapter 4, we show the influence of native oxidation on the *I*-*V* characteristics of TiN films. It is found that for ultra-thin TiN films (below 5 nm), the oxidation can significantly increase the resistance of the films and change the *I*-*V* characteristics from their original linearity to non-linearity (Fig. 4.8). We attributed the non-linearity to the oxidation of the film and the TiN/Pt-electrode interfaces. Intrinsically, Pt/TiN contacts are ohmic. However, the native oxidation can lead to the formation of Ti-O bonds at the interfaces which results in a rectifying (Schottky-like) behavior (see Section 4.1.4.2, Chapter 4). Additionally, this oxidation can produce "*aging effect*" which leads to the modification of the *I*-*V* characteristics with time.

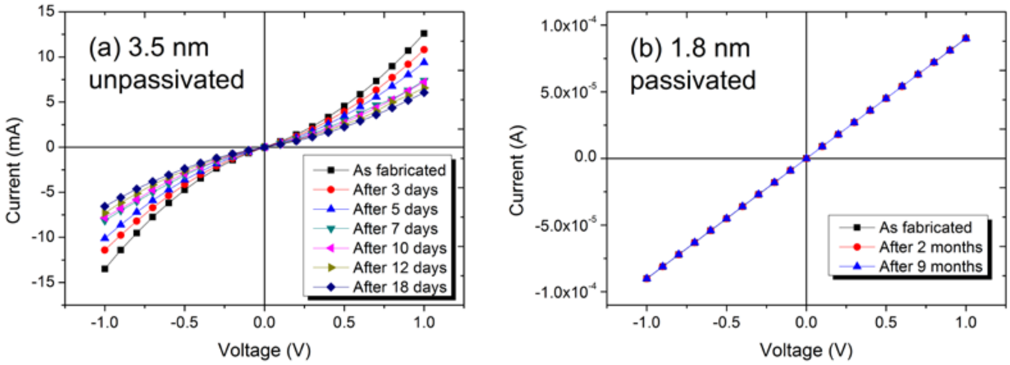

Figure 5.1. *I*-*V* characteristics of an unpassivated 3.5 nm TiN (a) and a 1.8 nm TiN *in situ* passivated by 15 nm a-Si (b); both samples are measured after different aging times in air.

Fig. 5.1 (a) shows the degradation of an unpassivated 3.5 nm TiN film. The resistance of the layer gradually increases with time. This is ascribed to the ongoing oxidation of the film as the oxidants continue their diffusion. No "*aging effect*" is observed for the passivated films. For example, measurements on a passivated 1.8 nm

TiN film using amorphous silicon (a-Si) show that the *I-V* characteristics remain linear and highly reproducible (Fig. 5.1 (b)) even after 9 months. The results indicate that the unprotected thin TiN films degrade upon exposure to air and a suitable passivation layer is needed to prevent the degradation.

For TiN films thicker than 5 nm, the influence of the native oxidation on the linearity of the *I-V* characteristics was not observed. Nevertheless, the oxidation results in a native oxide layer (e.g. with a thickness of about 2 nm for a 10 nm as-deposited TiN film, see Fig. 2.5, Chapter 2). This reduces the initial thickness of TiN layer. In Chapter 4, we present the determination of TiN resistivity using CTLM and linear test structures. Electrical measurements for both structure types provide sheet resistance (R_{sh}) from which the resistivity is calculated ($\rho = R_{sh} \times t$). To accurately extract the resistivity, the influence of native oxidation must be taken into account as the oxidation decreases the initial film thickness.

Table 5.1 compares the resistivity values of TiN with and without considering the native oxidation. The as-deposited thickness t was measured before exposure to air (column 1). After exposure, the TiN was partially oxidized. We used SE to determine the thickness t_1 of the remaining TiN layer (column 2). The R_{sh} values were obtained from the *ex situ* electrical measurements (column 3). The actual resistivity ρ_1 is given by the product $R_{sh} \times t_1$ (column 4). These are the resistivity values after correcting for the native oxidation. Without considering the native oxidation, the resistivity is calculated as $R_{sh} \times t$ (column 5). Comparing the values in columns 4 and 5, one can see the growing discrepancy with decreasing film thickness.

Table 5.1. The comparison of the calculated resistivity values with and without correcting for the native oxidation: ρ_1 is the actual resistivity of TiN ($\rho_1 = R_{sh} \times t_1$), ρ is the resistivity assuming the initial TiN thickness not to decrease ($\rho = R_{sh} \times t$).

Thickness of as deposited TiN, t (nm)	Thickness of TiN after exposure to air, t_1 (nm)	Sheet resistance, R_{sh} (Ω/□)	ρ_1 (μΩ-cm)	ρ (μΩ-cm)
10	8.3	163	135	163
15	13.7	91	125	136
20	19	63	120	126

5.3.2. Optical model for *in situ* spectroscopic ellipsometry

To monitor the oxidation by SE, an optical model must be constructed. A three-layer model was previously used by Hones et al. [5] to determine the oxide thickness by SE for the oxidation of 300–450 nm thick sputtered TiN films. The model included an intermixed layer accounting for a partially oxidized film underneath a pure TiO_2 layer. With the thickness of several hundred nanometers, TiN films were assumed to be opaque; therefore the TiN layer was considered as the substrate in that model. However, within several tens of nanometers of thickness, TiN is transparent and absorbing in the visible and near infrared wavelength range. As a consequence, it cannot be treated as an opaque substrate in the optical model.

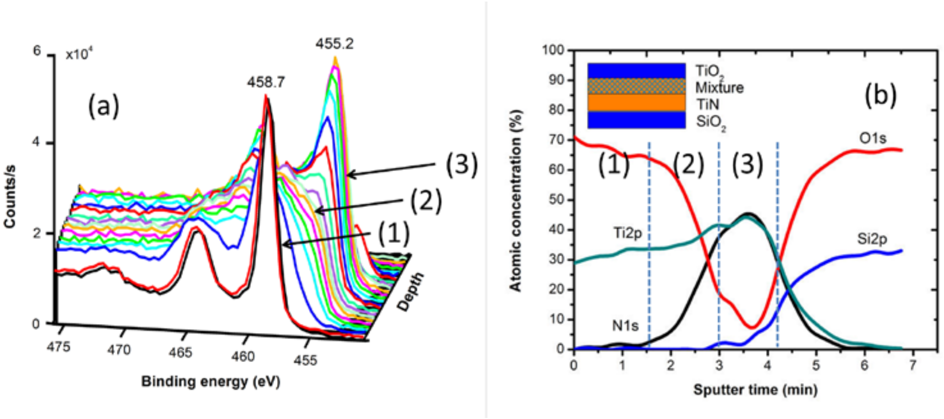

Figure 5.2. XPS spectra (a) and corresponding depth profile (b) of a partially oxidized 15 nm TiN layer grown at 425 °C on Si substrate covered with 108 nm thermal oxide. The TiN layer was exposed to oxidizing ambient for 3.5 hours at 325 ^{o}C (Sample 4, Table 5.4). The inset in (b) shows the optical SE model.

In this study, the construction of the optical model was approached by analyzing the profile of a partially oxidized sample. Starting from a 15 nm TiN film grown at 425 ^{o}C on Si covered with a 108 nm thermal oxide layer, the oxidation was performed for 3.5 hours at 325 ^{o}C. The relatively low oxidation temperature was intentionally chosen to ensure only partial oxidation. The XPS depth profile spectra of the sample after this oxidation are composed of three regions, which are shown in Fig. 5.2 (a). Region (1) represents pure TiO_2 with the binding energy of 458.7 eV which corresponds to the electronic state of Ti_{2p} in amorphous TiO_2 [3]. On the other side, in region (3), the peak at 455.2 eV corresponds to the electronic state of Ti_{2p} in stoichiometric TiN. The broadened spectra in between (region (2)) indicate the existence of a mixture of nitride and oxide. The corresponding elemental depth profile of the film is shown in Fig. 5.2

(b). Region (1) contains pure titanium oxide. In region (2), the oxygen content gradually decreases whereas the nitrogen content increases, ending by a pure TiN layer in region (3) with the Ti:N ≈1:1.

Based on the XPS analyses, the optical model for SE measurements is constructed as schematically shown in the inset of Fig. 5.2 (b). It contains three layers: TiO_2 on top (region (1)), a mixture of TiO_2 and TiN in the middle (region (2)) and a pure TiN layer underneath (region (3)). Properties of the 108 nm SiO_2 are fixed in the model; Si is the substrate. The optical functions of TiO_2 are described below. The intermixed layer is modeled using the Bruggeman effective medium theory as a 0.5/0.5 vol. fraction mixture of the oxide and nitride [9]. For TiN, the dielectric functions are presented in Chapter 2.

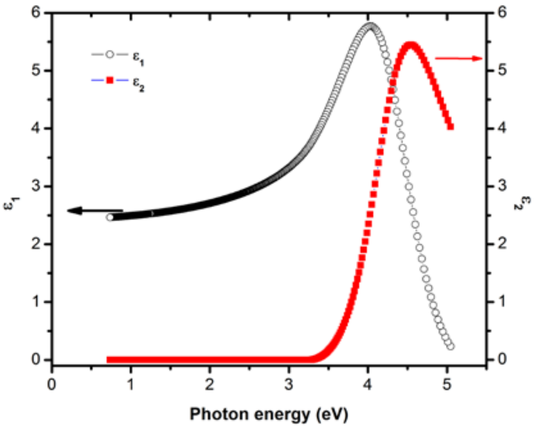

Figure 5.3. Dielectric functions of TiO_2 according to the Tauc–Lorentz model. The ε_2 curve is described by Eqs. 5.1. The optical band gap of the TiO_2 is extracted from this curve as the first point where $\varepsilon_2 > 0$.

The dielectric functions of TiO_2 (shown in Fig. 5.3) are parameterized by using the Tauc–Lorentz formulation [10]. The imaginary part ε_2 of the complex dielectric function is mathematically described by equations [11]

$$\varepsilon_2 = \frac{A E_{n0} C \left(E_n - E_g\right)^2}{\left(E_n^2 - E_{n0}^2\right)^2 + C^2 E_n^2} \frac{1}{E_n} \quad \text{if } E_n > E_g \qquad (5.1\text{-a})$$

$$\varepsilon_2 = 0 \quad \text{if } E_n \le E_g \qquad (5.1\text{-b})$$

where *A* and *C* represent the amplitude and half-width of the ε_2 peak, respectively. The band gap E_g of TiO_2 is thus determined from the imaginary part ε_2. The extracted value of 3.25 eV is very close to the band gap of 3.27 eV reported by Zhang et al. [12].

To qualitatively evaluate the applicability of this model, we compare the film thickness obtained by SE with the results from XRR measurements (see Fig. 5.4).

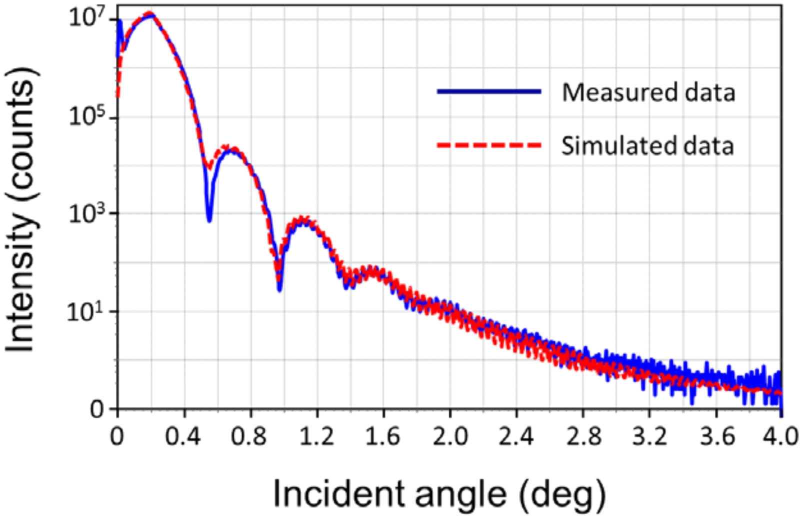

Figure 5.4. XRR measurements on a 5 nm TiN layer after oxidation at 400 °C. The good agreement between measured data (solid line) and simulated data (dash line) was obtained, from which the density and thickness of the layers were determined as given in Table 5.2.

The comparison is done for a completely oxidized 5 nm TiN layer. The results are shown in Table 5.2. It is found that the thickness values obtained from both techniques are in good agreement. The TiO_2 density (determined by XRR) is 3.74 g/cm^3, i.e. much lower than 3.9 g/cm^3 and 4.17 g/cm^3 known for anatase and rutile TiO_2, respectively. However, the obtained density is close to the density of amorphous TiO_2 (3.8 ±0.1 g/cm^3) reported by Nakamura et al. [13]. The amorphous state is supported by the results from the grazing incidence-ray diffraction (GI-XRD) analyses, where no diffraction peaks of either anatase or rutile TiO_2 are found. Therefore, in addition to the XPS analyses for a partially oxidized sample, the good agreement between SE and XRR verifies the applicability of the optical model and the dielectric functions of TiO_2.

Table 5.2. Mass density and film thickness measured by SE and XRR.

Material	Density (g/cm^3)	Thickness (nm)	
	XRR	XRR	SE
SiO_2	1.99	107.5±1	108±0.1
TiO_2	3.74	9.0±1	8.9±0.1

5.3.3. Oxidation of 15 nm thick TiN films

The oxidation of TiN in oxygen was real-time monitored using our optical model. Fig. 5.5 (a) shows the oxidation at 425 °C of a 15 nm thick TiN film grown at 350 °C. During the oxidation, the thicknesses of the oxide, the intermixed nitride and oxide and the nitride layers were monitored. It can be seen from Fig. 5.5 that the oxidation starts immediately after introducing oxygen into the chamber. Oxidation of a material commonly consists of two regimes: a linear kinetic-limited regime at the start is followed by a diffusion-controlled parabolic regime [3-5]. However, in the present case, the curve showing the thickness of the oxide layer indicated in Fig. 5.5 (a) can be divided into four stages. Starting with a steep and very short-in-time growth in stage 1, the thickness increase slows down in stage 2. Hereafter, the oxidation continues with an enhanced rate in stage 3 and finally slows down in stage 4. Similar behavior is observed for the oxidation of a 15 nm TiN film grown at 425 °C shown in Fig. 5.5 (b).

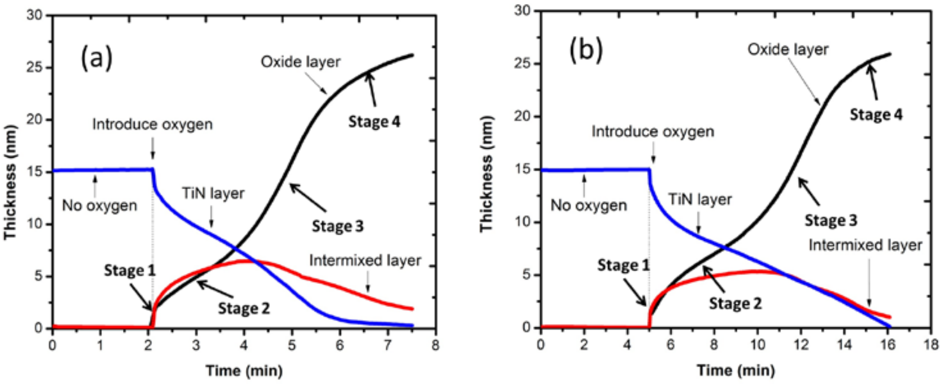

Figure 5.5. The oxidation behavior at 425 °C of 15 nm TiN films grown at 350 °C (a) and 425 °C (b). The films were deposited on Si substrate with a 108 nm thermal SiO_2.

The oxidation of the film grown at 350 °C (Fig. 5.5 (a)) is almost completed within 6 minutes. This is confirmed by the XPS depth profile in Fig. 5.6. The oxide layer with a thickness of approximately 26.2 nm is measured by SE. This thickness is in good agreement with theoretical calculation: 1 nm TiN layer will result in 1.8 nm of TiO_2 after being oxidized. This number is calculated by assuming the density and molecular weights of the materials as listed in Table 5.3.

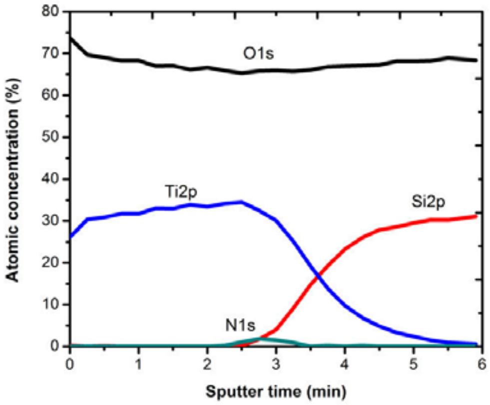

Figure 5.6. XPS depth profile after the oxidation at 350 ^{o}C of a 15 nm TiN grown at 350 ^{o}C. The profile confirms the nearly complete oxidation of the TiN. A negligible N concentration at the interface between SiO_2 and TiO_2 points to only a small amount of remaining TiN.

Table 5.3. Molecular weight and density of TiN and TiO_2.

Material	Mol. Weight (g/mol)	Density (g/cm^3)
TiN	61.874 [14]	5.21 [14]
TiO_2	79.866 [14]	3.74 [this work]

5.3.4. Oxidation of 5 nm thin TiN films

A four-stage oxidation is observed for 15 nm thick TiN films. However, for thinner TiN films, we have found a different behavior. The oxidation at 400 ^{o}C and 350 ^{o}C of a 5 nm thin TiN film grown at 425 ^{o}C (Fig. 5.7) provides the following observations. The oxide and the intermixed layers grows rapidly immediately after introducing oxygen. The TiN layer thickness quickly decreases, resulting in the disappearance of the pure TiN phase long before completing the oxidation. After that, the oxidation occurs for the

TiN phase in the intermixed layer. In comparison with the oxidation of 15 nm films, for 5 nm films there are only two clear stages observed.

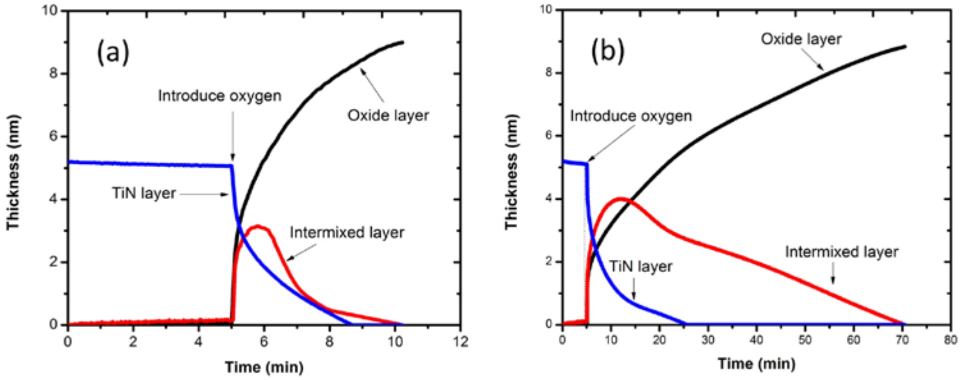

Figure 5.7. Oxidation at 400 ^oC (a) and 350 ^oC (b) of 5 nm thin TiN films grown at 425 ^oC. Oxygen was introduced 5 minutes later after starting the SE data acquisition.

5.3.5. Influence of temperature on oxidation

In order to study the influence of temperature on the oxidation of TiN, a series of oxidation experiments were carried out as given in Table 5.4. We investigate the influence of both oxidation temperature and growth temperature on the oxidation rate of the films.

Table 5.4. Influence of deposition and oxidation temperatures on total oxidation time of thin TiN films.

Sample	Thickness	Growth temperature	Oxidation temperature	Oxidation time
1	15 nm	350 ^oC	425 ^oC	6 min
2	15 nm	350 ^oC	350 ^oC	180 min
3	15 nm	425 ^oC	425 ^oC	11 min
4	15 nm	425 ^oC	325 ^oC	> 210 min
5	5 nm	425 ^oC	400 ^oC	5 min
6	5 nm	425 ^oC	350 ^oC	70 min

On one hand, a higher oxidation temperature significantly reduces the oxidation time. For example, a 15 nm thick TiN layer grown at 350 ^oC can be completely oxidized within 6 min at 425 ^oC (sample 1, Table 5.4). When the oxidation temperature is reduced to 350 ^oC, the oxidation can only be completed in 3 hours (sample 2). A similar trend is seen for the ultra-thin films (samples 5 and 6, Fig. 5.7). On the other hand, the rate of oxidation depends on TiN growth temperature, as illustrated by samples 1 and 3 (see also Fig. 5.5). The oxidation time of the film grown at 350 ^oC is significantly shorter than that of the film grown at 425 ^oC. This is possibly due to a denser film grown at a higher temperature (e.g. larger crystalline grains, less amorphous grain boundary material) which consequently results in a lower oxidation rate.

5.3.6. Proposed four-regime oxidation mechanism

The TiN film microstructure has been revealed by TEM (see Fig. 2.5, Chapter 2). The initial TiN films comprise of columnar grains surrounded by amorphous grain boundary material. This is schematically shown in Fig. 5.8 (a). When oxygen is introduced, the surface is rapidly oxidized, resulting in a fast increase of TiO_2 thickness (stage 1 in Fig. 5.5 (a)). This rapid oxidation can be related to the electron tunneling phenomenon, which was suggested in the previous studies on oxidation of silicon [15-16]. The amorphous grain boundary material provides favorable conditions (compared to the grains) for oxygen to diffuse deeper into the film. This leads to the formation of an intermixed layer (Fig. 5.8 (b)). With increasing oxidation time, the top oxide and the intermixed layer will further proceed from the surface deeper into the bulk (stage 2 in Fig. 5.5 (a)). This process narrows the TiN grains and sharpens the TiN pillars (Fig. 5.8 (c)). At a certain moment, a rapid lateral oxidation of the narrowed TiN grains, enhanced by their sharpness, will occur. This results in a fast disappearance of the large part of the TiN grains (Fig. 5.8 (d)), accompanied by the rapid increase of TiO_2 thickness. This is represented as stage 3 in Fig. 5.5 (a). In our earlier experiments on oxidation of mono-Si pillars we also observed this enhancement of the oxidation rate while sharpening the pillars [17]. The slow diffusion of oxygen through the formed TiO_2 layer completes the oxidation process (Fig. 5.8 (e)). This coincides with stage 4 in Fig. 5.5 (a).

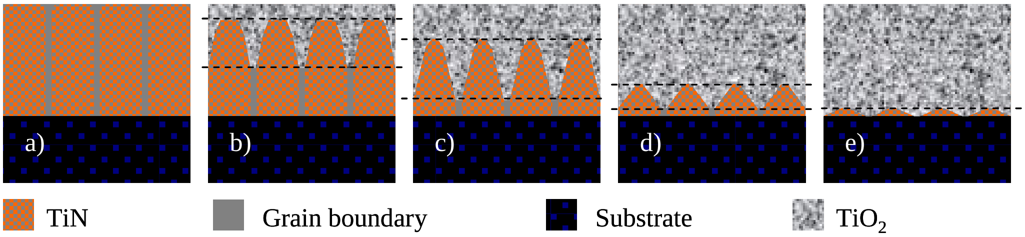

Figure 5.8. A schematic picture describing the proposed four regime oxidation of TiN: Initial TiN (a); stage 1: surface oxidation (b); stage 2: diffusion of oxygen along grain boundaries and later oxidation and sharpening of grains (c); stage 3: rapid oxidation of grains (d); and diffusion controlled oxidation (e).

The difference in oxidation behavior between the current work and the previous studies [2-5] can arise from the difference in grain size, as well as from the relative fraction of amorphous TiN between the grains. With a thickness of several hundred nanometers, the film is expected to have larger grains and therefore less amorphous TiN grain boundary material (this is due to the continuous lateral growth of grains during deposition). Therefore, after the first kinetics-limited stage (Fig. 5.8 (b)), the diffusion of oxygen via both grain boundaries and amorphous TiN does not play a significant role. The oxidation occurs mainly in the downwards direction and results in the diffusion-controlled parabolic regime.

In our study, we also observe different oxidation behavior for 15 nm and 5 nm TiN films. A two-regime behavior is observed for the 5 nm films. This is attributed to the fact that in this case stage 2 is not observed. Stage 1 and stage 2 coincide, then followed by stage 3.

5.4. Conclusions

In summary, we report on the influence of native oxidation on electrical properties of thin TiN films. For films thinner than 5 nm, this oxidation can irreversibly change the *I*-*V* behavior from linear to nonlinear and thus degrade the TiN. The native oxidation does not influence the linearity of *I*-*V* characteristics for films thicker than 5 nm. Nevertheless, it reduces the electrical thickness of TiN.

In the oxidation of thin TiN films at elevated temperatures, based on the XPS analyses for a partially oxidized TiN, we conclude the existence of an intermixed state between the oxide and nitride layers. By *in situ* spectroscopic ellipsometry using a three-layer optical model, we observed the real-time oxidation behavior of 15 nm and 5 nm TiN films in oxygen ambient in the temperature range 325–425 ^{o}C. The oxidation of the 15 nm TiN is described as a four-stage process: (1) surface oxidation, (2) diffusion of oxygen along grain boundaries and lateral oxidation and sharpening the grains, (3) rapid oxidation of the sharp grains, and (4) diffusion controlled oxidation. In the oxidation of 5 nm films, stage 1 and stage 2 coincide, followed by stage 3. The difference in the presented oxidation behavior compared to the commonly known two-stage oxidation for much thicker films is attributed to the difference in grain size, the relative fraction of the amorphous TiN between the grains, and the related diffusion of oxidants.

References

[1] W. Sinke, G. P. A. Frijlink, and F. W. Saris, *Appl. Phys. Lett.* **47**, 471 (1985).

[2] L. Soriano, M. Abbate, J. C. Fuggle, P, Prieto, C. Jimenez, J. M. Sanz, L. Galan, and S. Hofmann, *J. Vac. Sci. Technol. A* **11**, 47 (1993).

[3] N. C. Saha, and H. G. Tompkins, *J. Appl. Phys.* **72**, 3072 (1991).

[4] H. G. Tompkins, *J. Appl. Phys.* **70**, 3876 (1991).

[5] P. Hones, C. Zakri, P. E. Schmid, F. Levy, and O. R. Shojaei, *Appl. Phys. Lett.* **76**, 3194 (2000).

[6] F. Esaka, K. Furuya, H. Shimada, M. Imamura, N. Matsubayashi, H. Sato, A. Nishijima, A. Kawana, H. Ichimura, and T. Kikuchi, *J. Vac. Sci. Technol. A* **15**, 2521 (1997).

[7] H. Y. Chen, and F. H. Lu, *J. Vac. Sci. Technol. A* **23**, 1006 (2005).

[8] I. Suni, D. Sigurd, K. T. Ho, and M. A. Nicolet, *J. Electrochem. Soc.* **130**, 1210 (1983).

[9] H. G. Tompkins, and E. A. Irene, *Handbook of Ellipsometry*, William Andrew, New York (2005).

[10] G. E. Jellison, and F. A. Modine, *Appl. Phys. Lett.* **69**, 371 (1996).

[11] H. Fujiwara, *Spectroscopic Ellipsometry: Principles and Applications*, John Wiley & Sons, New York (2007).

[12] M. Zhang, G. Lin, C. Dong, and L. Wen, *Surf. Coat. Technol.* **201**, 7252 (2007).

[13] T. Nakamura, T. Ichitsubo, E. Matsubara, A. Muramatsu, N. Sato, and H. Takahashi, *Scripta Materialia* **53**, 1019 (2005).

[14] D. R. Lide, and W. M. Haynes, *CRC Handbook of Chemistry and Physics*, 90th Ed., CRC Press, Boca Raton, FL (2010).

[15] A. Kovalgin, A. Hof, and J. Schmitz, *Microelectron. Eng.* **80**, 432 (2005).

[16] R.B. Beck, and B. Majkusiak, *Electron Tech.* **21**, 65 (1988).

[17] A.Y. Kovalgin, J. Holleman, and G. Iordache, *IEEE Sensors Journal* **7**, 18 (2007).

6 Hot-wire generated atomic hydrogen and its impact on thermal ALD in $TiCl_4/NH_3$ system

In this chapter, we present the generation of atomic hydrogen made by the dissociation of molecular hydrogen upon collision with a tungsten (W) filament kept at a high temperature ($T \approx 1600–1900$ °C). By the experiments on etching of tellurium (Te) films, we demonstrate the ability to create atomic hydrogen and to introduce it in short pulses. We further utilize the generated atomic hydrogen (H) to explore its impact on surface reactions in the $TiCl_4/NH_3$ precursor system. Atomic hydrogen is introduced in pulses additionally to $TiCl_4$ and NH_3 with different pulse sequences. For the $TiCl_4/NH_3/H$ sequence, there is no influence on the process compared to the ALD without H-pulses. The growth rate remains at 0.02 nm/cycle and the oxygen content - at 3–5 at%. For the $TiCl_4/H/NH_3$ pulse sequence, the growth rate decreases to 0.01 nm/cycle and the oxygen content increases to 30–35 at%. This confirms the reduction of Ti-Cl surface groups by H and the creation of very reactive Ti surface. Only $TiCl_4/H$ pulses result in no growth after the formation of approximately one monolayer. Similar effect occurs after introducing NH_3 via the hot filament, pointing to the decomposition of NH_3 and the formation of atomic hydrogen.

6.1. Introduction

It has been projected in the International Technology Roadmap for Semiconductors (ITRS) that new materials will be intensively introduced, starting from 2018, to replace or to be integrated with silicon in integrated circuits [1]. The coming era of new materials naturally implies a development of new technologies, new processes, and new precursors. Atomic Layer Deposition (ALD) is an excellent example of a process to realize new materials.

ALD has a constantly growing market for deposition of dielectric, semiconductor and metallic layers of various functionalities where excellent optical, mechanical, electrical or chemical properties are required. The most important advantage of ALD over other deposition techniques is its capability to deposit films of uniform thickness on arbitrary surfaces, and to control the thickness with a very high precision. Thermal ALD processes are commonly used to deposit compounds. Single-element films of metals and semiconductors, which become increasingly important for industry, are however very difficult to deposit using thermal-only ALD processes [2]. A solution in this case is plasma-enhanced ALD (PEALD), also called radical-enhanced ALD (REALD). Hydrogen- or nitrogen-based plasmas are used for PEALD of Ta(N), Ti(N), Ru, Si and Ge [3-11], Al [12] as well as AlN [13] and GaN [14]. Pt can be grown using remote O_2 plasmas [15]; PEALD of Al_2O_3 demonstrates better film properties compared to the thermal process [16-17].

In this chapter, we explore an alternative technique to generate radicals *without* plasma. We choose processes where dissociation of a certain precursor to form radicals can be achieved due to collisions with a hot tungsten filament heated up to a temperature in the range of 1600−1900 ^{o}C. In this work, a plasma-based source of atomic hydrogen is substituted by the hot-wire source. This ensures that only molecular and atomic hydrogen are present in the gas phase, i.e. no ions, excited particles and UV photons.

We use *in situ* spectroscopic ellipsometry to characterize the generation of atomic hydrogen by real-time etching of tellurium films. We demonstrate that atomic hydrogen can be generated and introduced in pulses, which is required for ALD processes. We study the influence of adding atomic hydrogen pulses to $TiCl_4/NH_3$ ALD processes for further understanding the surface reaction mechanism in ALD of TiN.

6.2. Experimental

Atomic layer deposition of TiN. –The ALD of TiN is performed in our home-built ALD reactor described in Chapter 1. The reactor is equipped with a spectroscopic ellipsometer (Woollam M2000) for real-time process monitoring, as demonstrated in Chapters 2, 3, and 5.

Generation of atomic hydrogen. –To create atomic hydrogen, we integrate a hot-filament (W) to the ALD reactor (see Chapter 1). The filament is connected to a DC source to control the filament temperature. The filament temperature is determined from the *I-V* measurements and calculated using the tungsten-TCR value of $0.4403 \times 10^{-2}\ K^{-1}$ [18].

It is reported that molecular hydrogen can be dissociated upon collision with a W filament surface at high temperatures [19]. The dissociation probability p of H_2 increases with temperature and reaches saturation value of $p \approx 0.3$ at a temperature of about 2300 ^{o}C [20]. The value 0.3 represents the sticking probability of molecular hydrogen on W surface. In this work, the W filament is heated up to 1900 ^{o}C. To examine the presence of atomic hydrogen, we performed an intensive study on etching of thin Te films. For the experiments, Te thin films were deposited on 4-inch Si substrates (with native oxide) by sputtering from a 2-inch diameter Te target (99.999% purity, supplier Kurt J. Lesker). Prior to sputtering, the substrates were cleaned by a standard cleaning process including the immersion into fuming and boiling HNO_3. The Te layer thickness was measured by SE and verified by helium ion microscopy (HIM).

6.3. Results and discussion

6.3.1. Etching of tellurium films by atomic hydrogen

It is reported that volatile tellurium hydride (TeH_2) can be formed according to the reaction [21]

$$2H\ (gas) + Te\ (solid) = TeH_2\ (gas) \qquad (6.1)$$

The reaction can occur at room temperature and, according to Ref. [21], the reaction rate decreases with increasing temperature. It is further reported that the by-product of the etching reaction TeH_2 can be decomposed, even at room temperature [22]:

$$TeH_2\ (gas) = H_2\ (gas) + Te\ (solid) \qquad (6.2)$$

To note, Te does not react with molecular hydrogen. Therefore, a thickness decrease of the Te films while introducing hydrogen gas via the hot-wire setup can prove the generation of atomic hydrogen and characterize this process.

Fig. 6.1 shows the thickness evolution of a 26 nm Te film during the etching at room temperature. Three stages are presented in the figure. Stage 1 corresponds to the filament switched off while introducing molecular hydrogen via the filament. No change in the film thickness is observed, thereby pointing to no-TeH_2 formation. In stage 2, the molecular hydrogen flow is replaced by nitrogen flow and filament heating is started. Again, no thickness change is seen. In stage 3, the filament is kept at 1900 ^oC and molecular hydrogen is introduced via the filament. One can clearly see a sharp decrease of the film thickness due to Te etching, thereby confirming the thermal generation of atomic hydrogen upon collision with the hot filament surface.

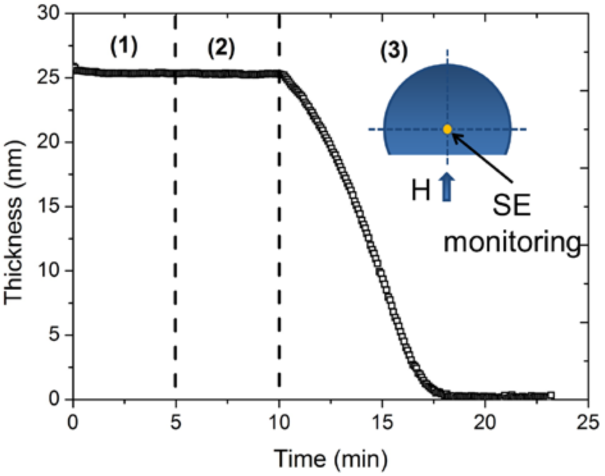

Figure 6.1. The real-time thickness evolution of an initial 26 nm Te film during the etching process at room temperature monitored by *in situ* SE. Three stages of the process are indicated by the dashed vertical lines: (1) introducing molecular hydrogen, filament off; (2) stopping introducing hydrogen, heating up the filament and (3) introducing hydrogen (H_2) via the filament kept at 1900 ^oC. The total pressure is 5.7×10^{-4} mbar. The flow direction of atomic hydrogen (H↑) is shown. Near-half of the wafer is used for the experiment. SE monitoring is performed at the center of the wafer, as indicated.

The influence of filament temperature on the etch rate is shown in Fig. 6.2. The film thickness decreases linearly with increasing etch time pointing to a constant H-generation rate at a given temperature. The etch rate increases from 1.2 nm/min at 1650 ^oC to 4.9 nm/min at 1900 ^oC, giving an increase of roughly 0.15 nm/min per 10 degrees of the filament temperature. This is attributed to the increase of dissociation of molecular hydrogen with increasing filament temperature [20].

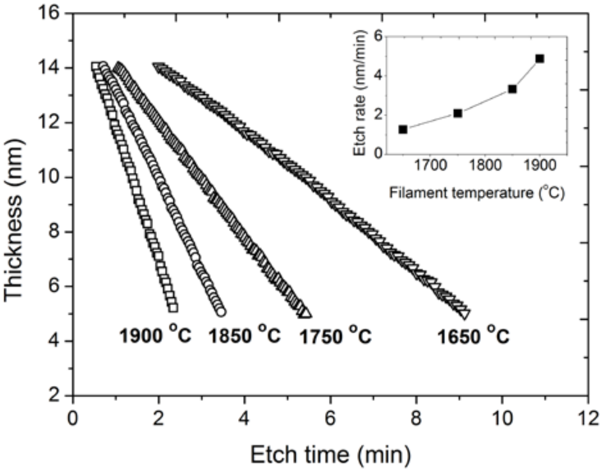

Figure 6.2. Etching of Te films at room temperature and different filament temperatures. The total pressure is kept at 5.7×10^{-4} mbar. The inset shows the filament-temperature dependence of etch rate.

The dependence of the etch rate on total pressure is described in Fig. 6.3 (a). Again a linear decrease of the thickness upon the etch time is observed. The etch rate decreases from 4.9 nm/min at a pressure of 5.7×10^{-4} mbar down to 1 nm/min at 3.3×10^{-3} mbar. At a higher pressure, the decrease is less dramatic compared to a lower pressure (see the inset in Fig. 6.3 (a)). Total pressure has a large influence on the gas-phase recombination of atomic hydrogen. The latter is a three-body process [23] and requires three particles to collide at the same time. Any surface inside the reactor can act as a third particle (body). From our modeling using gas phase recombination only (see Fig. 6.3 (b)), about 5% of H atoms will recombine in gas phase at a pressure of 1×10^{-2} mbar. The gas phase recombination increases to 80% when the pressure becomes one order higher. In the pressure range used in this work (i.e. 3.3×10^{-3}–5.7×10^{-4} mbar), the recombination is negligible. We attribute the decrease of etch rate with increasing total pressure to the increasing decomposition (reaction 6.2) and re-deposition of the etching product. The latter is demonstrated further in this section.

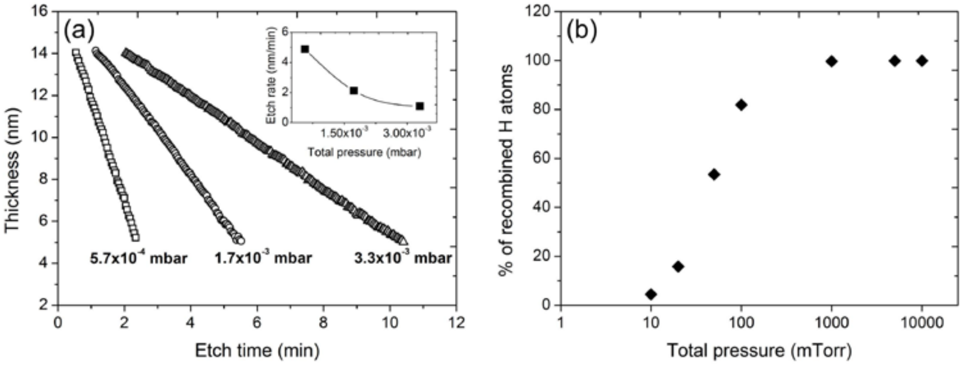

Figure 6.3. (a) - Etching of Te films at various total pressures. The wafer is at room temperature and the filament temperature is 1900 ^oC. The inset shows the total-pressure dependence of the etch rate. (b) – modeled percentage of H atoms, recombining in gas phase, versus total pressure.

Fig. 6.4 shows the influence of substrate temperature on etch rate. With increasing substrate temperature, the etch rate decreases (see the inset of Fig. 6.4). The lower etch rate at a higher substrate temperature is attributed to two concurrent processes: etching and re-deposition. The latter increases with temperature due to the increasing decomposition of the synthesized TeH_2 (reaction 6.2).

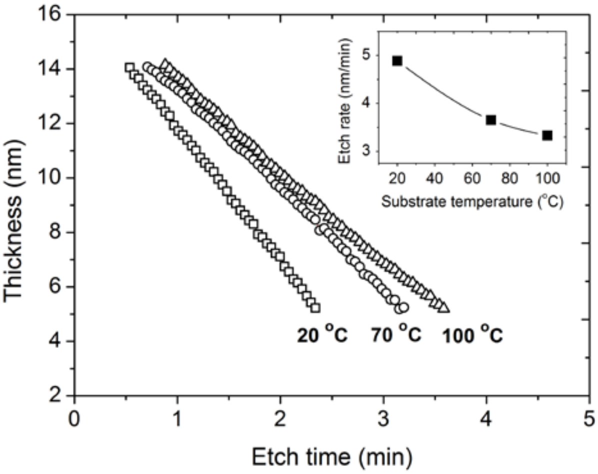

Figure 6.4. Etching of Te films at various substrate temperatures. The filament temperature is 1900 ^oC and the total pressure is 5.7×10^{-4} mbar. The inset shows the substrate-temperature dependence of etch rate.

Tellurium re-deposition is further explored, as shown in Fig. 6.5. At the time t_1, the filament is *on*, and hydrogen gas is introduced via the filament. Immediately after t_1, a small increase in thickness can be seen, which is not observed in Fig. 1. It is important to mention that in Fig. 6.1, near-half wafer is used for the experiment (see the inset) and the sample edge was close to the point where SE monitoring is performed. Atomic hydrogen is hence delivered at nearly the same time to the wafer edge and to the SE monitoring area. In the experiment in Fig. 6.5, atomic hydrogen is first delivered to the wafer edge where it reacted with Te to form TeH_2. This leads to a depletion of atomic hydrogen in the gas flow moving along the wafer surface. On the other hand, the formed TeH_2 is transported by the flow towards the wafer center where it will decompose. Based on the distance, gas flow and the pressure, lifetime of the synthesized TeH_2 seems to be quite short. After the film front has approached the wafer center (depicted as time t_2), the gradual thickness decrease proceeds. The re-deposition of Te confirms the *in situ* TeH_2 synthesis in the reactor.

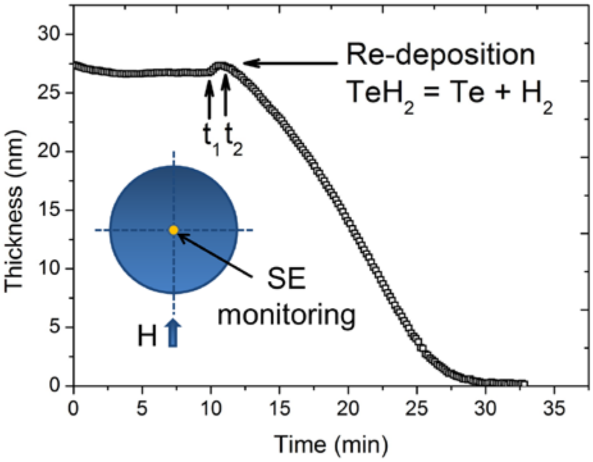

Figure 6.5. Re-deposition and etching of Te film. The filament temperature is 1750 °C, the total pressure is 5.7×10^{-4} mbar, and the substrate temperature is 25 °C. The flow direction of atomic hydrogen (H↑) is shown. In contrast with the experiment shown in Fig. 6.1, a whole wafer is used. SE monitoring is performed at the center of the wafer, as indicated.

To estimate the minimum dissociation probability of H_2, a simple calculation can be done. As the number of Te atoms per 1 nm film thickness and per 1 cm^2 of surface is approx. 1.5×10^{15}, two-times more H atoms are needed to form TeH_2. To achieve Te etch rate of 4.9 nm/min, a flux of atomic hydrogen of 1.5×10^{16} [atoms/(min×cm^2)] is required. Given the input H_2 flow of 10 sccm and 5.7×10^{-4} mbar pressure, the H_2-

surface flux can be estimated at 2.7 × 10^{19} [molecules/(min×cm^2)]. It is assumed that all incoming molecules will collide with the film surface. Comparing the H- and H_2-surface fluxes, the dissociation percentage of H_2 can be estimated at 1.7%. This represents the minimum amount of atomic hydrogen needed to maintain the required etch rate of Te. The actual amount can be higher, as recombination of H into H_2 is not taken into account. It is assumed that every H atom will collide with Te surface and all the collisions contribute to the reaction, meaning a sticking probability of 1.

6.3.2. Impact of atomic hydrogen on thermal ALD of TiN

Using real-time SE, we study deposition kinetics of TiN ALD with the sequence of $TiCl_4/NH_3$ pulses (N_2 purge is introduced in between the precursor pulses, see also Chapter 2). We introduce additional atomic hydrogen in the sequences $TiCl_4/NH_3/H$, $TiCl_4/H/NH_3$ and $TiCl_4/H$ only. Furthermore, we look at the effect of the NH_3 pulse introduced via the hot wire.

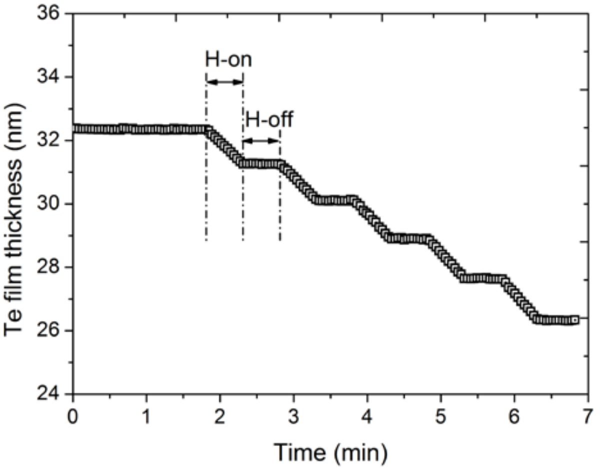

Figure 6.6. Etching of Te using H-pulses at a W-filament temperature of 1900 ^oC.

It is important to know whether atomic hydrogen can be introduced in short pulses to the reactor. Fig. 6.6 shows an example of etching Te films by 30 s pulses of atomic hydrogen. Obviously, etching starts and stops without a delay. In our experiments, pulse times down to 10 seconds cause no delay to the onset of etching, enabling atomic hydrogen pulses for ALD. Although shorter pulses were not examined, we expect shortening the pulse time down to a few seconds not to be the limiting factor.

The pulse sequence $TiCl_4/NH_3$

In Chapter 2, we describe the standard thermal ALD of TiN using the sequence of $TiCl_4/NH_3$ pulses. In the linear ALD regime, a growth rate of 0.02 nm/cycle is observed. The evolution of film thickness as a function of the number of cycles, including the thickness change within each cycle, is shown in Fig. 6.7 (a). During the deposition, two half-reactions occur:

$$-NH + TiCl_4 \rightarrow -NTiCl_3 + HCl \quad (6.3)$$

$$-NTiCl + NH_3 \rightarrow -TiNH_2 + HCl \quad (6.4)$$

The composition of TiN is analyzed using XPS depth profiling (see Fig. 6.7 (b)). In order to prevent oxidation during the exposure to air, the film has been covered by a 15 nm a-Si layer. The analyzed TiN film contains 3–5 at% of oxygen (residual gas) that is incorporated during the growth.

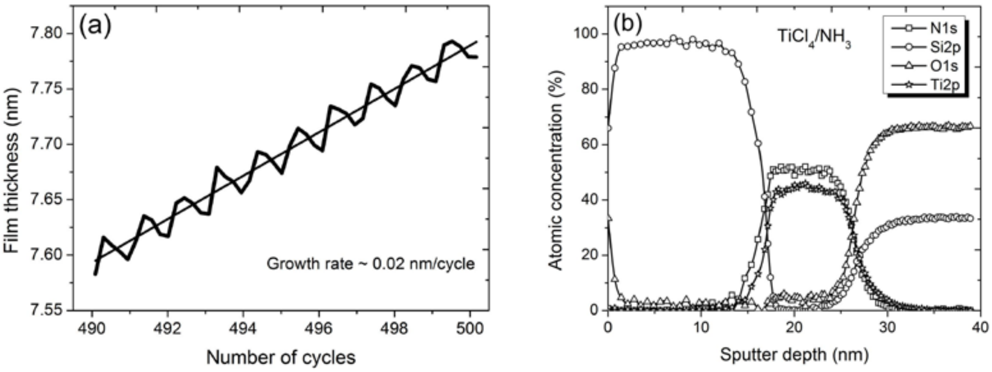

Figure 6.7. Growth of TiN during 10 ALD cycles at 350 °C with $TiCl_4/NH_3$ pulse sequence (a) and XPS depth profile (b) of the corresponding TiN film with a thickness of 10 nm passivated by a 15 nm amorphous Si layer.

The pulse sequence $TiCl_4/NH_3/H$

Atomic hydrogen is now introduced after each $TiCl_4/NH_3$ cycle, i.e., after half-reaction (6.4) where the surface is covered with NH-groups. The growth as measured by SE is shown in Fig. 6.8 and a growth rate of 0.019 nm/cycle is obtained.

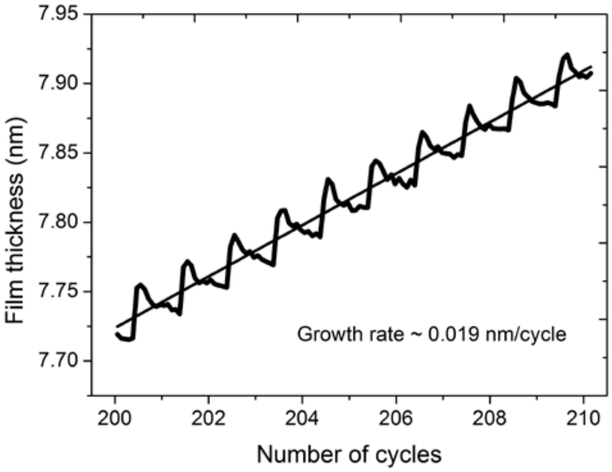

Figure 6.8. Growth of TiN in 10 ALD cycles with $TiCl_4/NH_3/H$ pulse sequence. The linear fit represents the linear growth of the film with a growth rate of 0.019 nm/cycle.

The atomic-hydrogen pulse duration is 15 seconds. There is no influence when the pulse time is shortened to 8 s. The relatively long pulse times of atomic hydrogen are chosen to ensure a sufficient distribution of the reactant over the wafer surface. The obtained growth rate is very close to the growth of TiN without atomic hydrogen pulses. The results show that atomic hydrogen has no influence on the TiN growth if introduced in this pulse sequence.

The pulse sequence $TiCl_4/H/NH_3$

In this experiment, the atomic hydrogen pulse is introduced between the $TiCl_4$ and NH_3 pulses, i.e., after half-reaction (6.3) where the surface is covered with TiCl-groups. The growth, as measured by SE, is shown in Fig. 6.9. A much lower growth rate of 0.01 nm/cycle is obtained. Also, the shape of a single ALD cycle is changed significantly compared to that in Figs. 6.7 and 6.8.

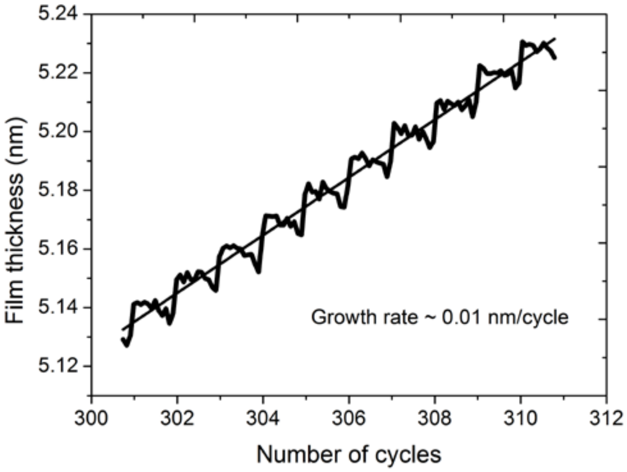

Figure 6.9. Growth during 10 ALD cycles with the pulse sequence $TiCl_4/H/NH_3$. The linear fit represents the linear growth with a growth rate of 0.01 nm/cycle.

The introduction of atomic hydrogen after half-reaction (6.3) will result in the reduction of the Ti–Cl surface and the release of HCl as the reaction product. In this case, the reduced surface will contain Ti– or/and possibly Ti–H terminations. The chemical reactivity of this surface will be much higher than of the one with Ti–Cl termination (formed after half-reaction (6.3), i.e. after $TiCl_4$ pulse). The newly-developed surface will be more reactive to residual oxidizing gases (e.g. H_2O, O_2) in the ALD system and process gases. At a partial pressure of 2×10^{-7} Torr of these gases (reactor base pressure), the arrival rate of molecules at a surface is approximated at 0.1 monolayer/sec. The mentioned higher surface reactivity will result in a higher degree of surface oxidation.

This is evident from the XPS depth profile shown in Fig. 6.10. The amount of oxygen incorporated in the film increased from 3–5 at% for the TiN in Fig. 6.7 (b) to 30–35 at% for the ALD with atomic hydrogen pulse after each $TiCl_4$ pulse. The higher oxygen content confirms the increased surface reactivity, thereby indeed indicating the reduction of Ti–Cl surface groups by atomic hydrogen.

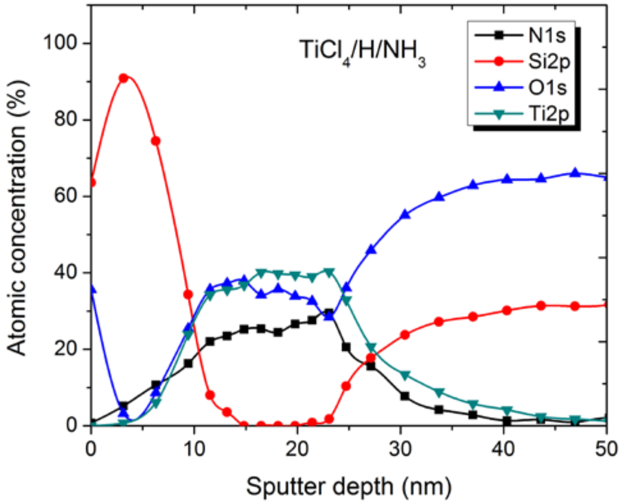

Figure 6.10. XPS depth profile of the sample with $TiCl_4/H/NH_3$ pulse sequence. The film is passivated by an a-Si layer to prevent oxidation.

The pulse sequence $TiCl_4/H$ only

To explore the feasibility to grow films without NH_3, we introduce $TiCl_4$ and atomic hydrogen pulses only (certainly with N_2 purge in between). Fig. 6.11 (a) shows the real-time evolution of film thickness. The vertical axis shows the (optically determined) thickness up to 0.35 nm, assuming the optical properties of Ti. However, without an N (NH_3) source, the layer will contain a considerable amount of oxygen.

It is important to note that in this pulse sequence, no growth was observed on SiO_2 substrate. Therefore, a 1.5 nm TiN film was deposited on SiO_2 as a seeding layer.

After the incubation time of several minutes, the layer starts to grow rapidly with an average growth rate of 0.013 nm/cycle up to 0.2 nm of layer thickness. This approximates one monolayer of thickness. Then, the deposition slows down to 0.0008 nm/cycle for the rest of the process.

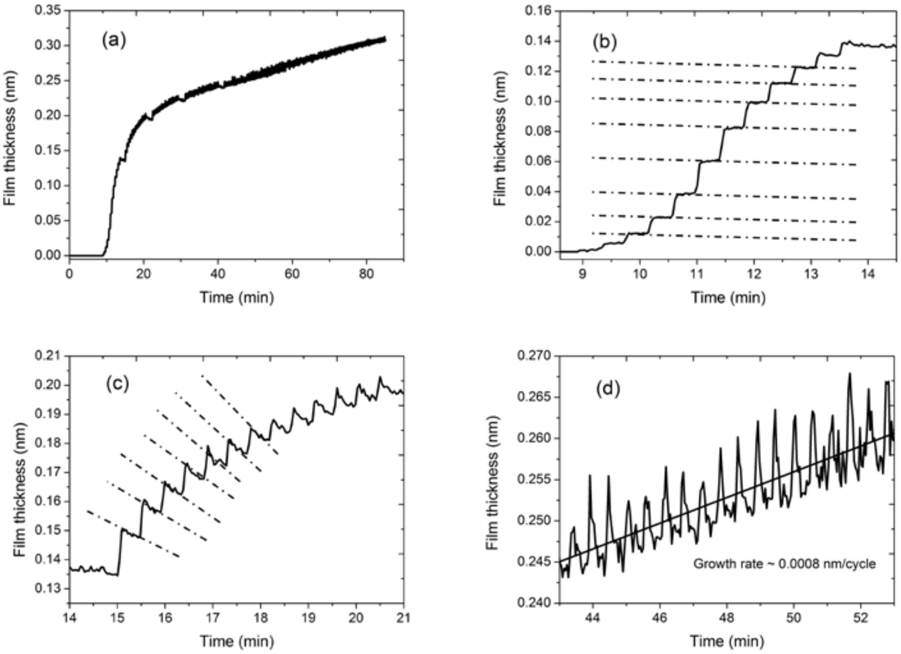

Figure 6.11. *In situ* SE monitoring for TiCl$_4$/H pulse sequence at different stages of the film growth on pre-deposited 1.5 nm TiN seeding layer. (a), (b), (c) and (d) refer to the subsequent stages in the deposition process (see the text). The film thickness is determined, assuming optical properties of Ti for the deposited layer.

In this process, each cycle consists of a sequence of TiCl$_4$/N$_2$/H/N$_2$ pulses with the corresponding pulse durations of 2/4/15/4 seconds. In the growth curve in Fig. 6.11, different stages (excluding the growth delay due to nucleation) of the deposition process can be discovered: the initial-rapid, intermediate-slow-down and final-saturation growth. In the rapid growth stage (9-14 min), the average deposition rate is approximately 0.013 nm/cycle. The individual deposition cycles are shown in Fig. 6.11 (b). A flat plateau in each step is observed, indicated by the dashed lines in the figure. In the stage of slowing down (15-20 min, Fig. 6.11 (c)), the thickness per cycle gradually decreases with time. In the stage of saturation (Fig. 6.11 (d)), a growth rate of 0.0008 nm/cycle is obtained.

The three stages observed for the TiCl$_4$/H pulse sequence can be attributed to the difference in chemical states of the surface in each stage. The rapid growth is caused by the adsorption of TiCl$_4$, reduction of Ti–Cl by atomic hydrogen, and the incorporation of residual oxygen. As the surface is gradually occupied by Ti–O groups, there are fewer sites available for the adsorption of TiCl$_4$ (which requires the availability of activated groups, e.g. –NH/–OH). This leads to the slow down stage of the growth.

When the surface is entirely covered by Ti–O groups, there is a lack of reactive sites for the reaction with $TiCl_4$ in the next cycle. When $TiCl_4$ is pulsed, it can physically adsorb on the surface and can be easily removed by a purge of inert gas (e.g. N_2). Therefore, the deposition will not proceed. The linear increase of film thickness in the saturation stage can be due to the deposition caused by the reaction between the incompletely removed precursors and the residual gas. This will lead to an extremely slow deposition since the number of reactions is virtually zero.

The pulse sequence $TiCl_4/NH_3$ (NH_3 via hot wire)

The standard ALD cycle for TiN is modified by changing the NH_3-pulse path via the normal gas line to the path over the hot W filament (T ~1900 °C). Fig. 6.12 (a) shows the TiN thickness as a function of the number of ALD cycles. One can see pulses of normal (gas line) NH_3 alternating with the pulses via hot filament. With no filament involved, the common linear growth of TiN is observed. However, when the NH_3-pulses are introduced via the hot filament, no TiN growth is found.

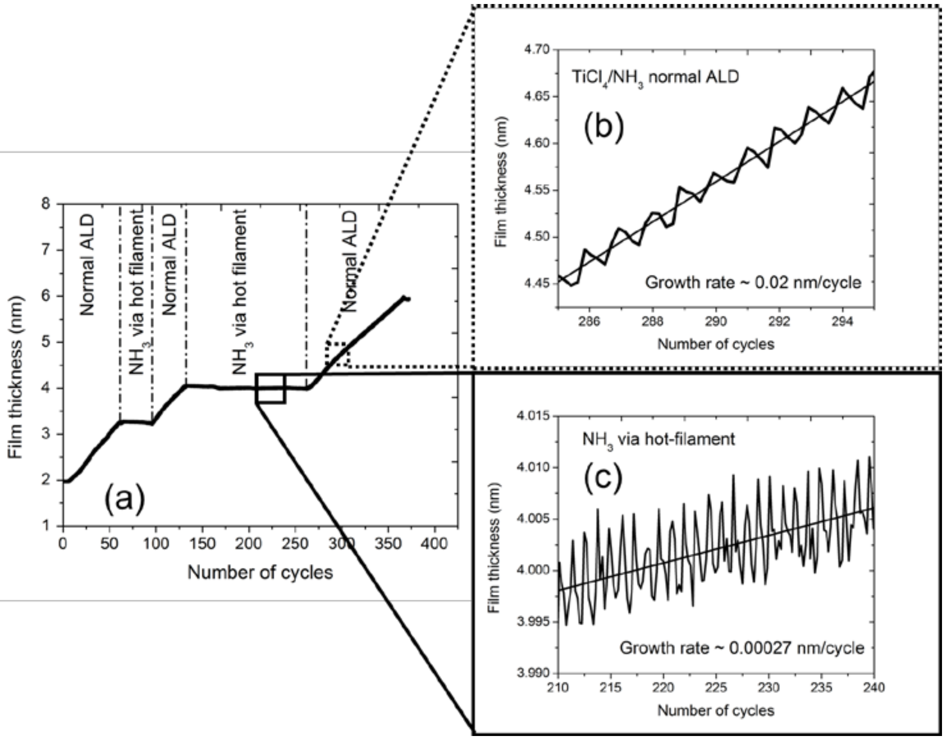

Figure 6.12. The growth of the film in $TiCl_4/NH_3$ pulse sequence where NH_3 is introduced either via the normal way (as in Fig. 6.7) or via the hot filament.

Details of the conventional ALD growth of TiN per deposition cycle are shown in Fig. 6.12 (b). At a pulse sequence duration of 2/4/2/4 seconds, the growth rate is 0.02 nm/cycle, as expected.

When ammonia is introduced via the hot filament with the same pulse duration, a 100 times lower growth rate of 0.00027 nm/cycle is observed. In this case, the film thickness is determined, assuming optical properties of TiN as the deposited layer. This is different from the $TiCl_4$/H case in the previous sub-section. Nevertheless, in both cases, the growth rates are extremely low, indicating the presence of atomic hydrogen from the dissociation of NH_3 on the hot filament, and the reduction of Ti–Cl bonds. The dissociation of NH_3 by hot wire has been reported in the literature [24]. In our system, the reduction process by atomic hydrogen after half-reaction (6.3) prevails over the Ti-NH formation during half-reaction (6.4).

6.4. Conclusions

In conclusion, we demonstrate the generation of atomic hydrogen by the etching of thin Te films and investigate the influence of experimental conditions (i.e. filament temperature, substrate temperature and total pressure) on the etch rate using real-time SE. Firstly, the etch rate increases with filament temperature as higher temperatures provide more atomic hydrogen. Secondly, the etch rate decreases with increasing total pressure due to recombination of H and re-deposition of Te. The re-deposition indicates the decomposition of TeH_2 being formed as the etching product.

We have utilized the generated atomic hydrogen to explore its impact on surface reactions in the $TiCl_4/NH_3$ precursor system. Atomic hydrogen is introduced in pulses additionally to $TiCl_4$ and NH_3, with different pulse sequences. For the $TiCl_4/NH_3$/H sequence, we observe no influence on the growth process compared to the conventional TiN ALD without H-pulses. When the sequence is changed to $TiCl_4$/H/NH_3, the growth rate decreases twice and the oxygen content in TiN increases by a factor of 7–10 compared to the conventional TiN ALD. This is attributed to the reduction of chlorine terminations at the surface by atomic hydrogen. This results in a surface highly reactive with residual oxidizing gases (e.g. H_2O, O_2) present in the chamber. For the $TiCl_4$/H pulse sequence, no further growth is seen after the formation of approximately one monolayer. We further modify the conventional TiN ALD by introducing NH_3 via the hot filament. The absence of growth in this case is attributed to the decomposition of NH_3 on the hot filament surface and the generation of atomic hydrogen.

References

[1] International Technology Roadmap for Semiconductors (ITRS) 2011, http://www.itrs.net

[2] S. M. George, *Chem. Rev.* **110**, 111 (2010).

[3] S. M. Rossnagel, A. Sherman, F. J. Turner, *J. Vac. Sci. Technol. B* **18**, 2016 (2000).

[4] H. Kim, C. Cabral, C. Lavoie, and S. M. Rossnagel, *J. Vac. Sci. Technol. B* **20**, 1321 (2002).

[5] P. A. Coon, P. Gupta, M. L. Wise, and S. M. George, *J. Vac. Sci. Technol. A* **10**, 324 (1992).

[6] B. G. Koehler, C. H. Mak, D. A. Arthur, P. A. Coon, and S. M. George, *J. Chem. Phys.* **89**, 1709 (1988).

[7] P. Gupta, P. A. Coon, B. G. Koehler, and S. M. George, *Surf. Sci.* **249**, 92 (1991).

[8] E. Hasunuma, S. Sugahara, S. Hoshino, S. Imai, K. Ikeda, and M. Matsumura, *J. Vac. Sci. Technol. A* **16**, 679 (1998).

[9] S. Imai, T. Iizuka, O. Sugiura, and M. Matsumura, *Thin Solid Films* **225**, 168 (1993).

[10] J. W. Elam, M. Schuisky, J. D. Ferguson, and S. M. George, *Thin Solid Films* **436**, 145 (2003).

[11] O. K. Kwon, S. H. Kwon, H. S. Park, and S. W. Kang, *Electrochem. Solid-State Lett.* **7**, C46 (2004).

[12] Y. J. Lee, and S.-W. Kang, *Electrochem. Solid-State Lett.* **6**, C70 (2003).

[13] M. Bosund, T, Sajavaara, M. Laitinen, T. Huhtio, M. Putkonen, V.-M. Airaksinen, and H. Lipsanen, *Appl. Surf. Sci.* **257**, 7827 (2011).

[14] C. Ozgit, I. Donmez, M. Alevli, and N. Biyikli, *J. Vac. Sci. Technol. A* **30**, 01A124 (2012).

[15] H. C. M. Knoops, A. J. M. Mackus, M. E. Donders, M. C. M. van de Sanden, P. H. L. Notten, and W. M. M. Kessels, *Electrochem. Solid-State Lett.* **12**, G34 (2009).

[16] J. W. Lim, and S. Yun, *J. Electrochem. Solid-State Lett.* **7**, F45 (2004).

[17] B. Hoex, S. B. S. Heil, E. Langereis, M. C. M. van de Sanden, and W. M. M. Kessels, *Appl. Phys. Lett.* **89**, 042112 (2006).

[18] D. R. Lide, and W. M. Haynes, *CRC Handbook of Chemistry and Physics*, 90th Ed., CRC Press, Boca Raton, FL (2010).

[19] I. Langmuir, *J. Am. Chem. Soc.* **34**, 860 (1912).

[20] J. N. Smith, and W. L. Fite, *J. Chem. Phys.* **37**, 10 (1962).

[21] D. A. Outka, *Surf. Sci.* **235**, L311 (1990).

[22] A. Kuhn, A. Chevy, and M.-J. Naud, *J. Cryst. Growth.* **9**, 263 (1971).

[23] H. Wise, and C. M. Ablow, *J. Chem. Phys.* **35**, 10 (1961).

[24] H. Shimizu, K. Sakoda, T. Momose, M. Koshi, and Y. Shimogaki, *J. Vac. Sci. Technol. A* **30**, 01A144 (2012).

7

Conclusions and recommendations

7.1. Conclusions

The purpose of this research is to bring new insights into the relation between properties of ultra-thin metallic films made by atomic layer deposition (ALD) and their possible industrial applications. Conductive titanium nitride is the material of choice. We have investigated the growth behavior of ALD TiN on thermal SiO_2 using $TiCl_4/NH_3$ chemistry. Spectroscopic ellipsometry (SE) was employed to observe the real-time growth of the film. The oxidation mechanism of ultra-thin TiN in dry oxygen and the impact of native oxidation on the electrical behavior of TiN were examined. The properties of TiN films in the thickness range of 0.65–20 nm with respect to their electrical resistivity, temperature coefficient of resistance and response to external electric field were studied. For better understanding of the ALD chemistry and exploring the perspective of going to pure metals in future, we have created atomic hydrogen by hot-wire assisted thermal dissociation and investigated its role in the $TiCl_4/NH_3$ precursor system.

Dielectric functions and thickness of TiN films. The Drude–Lorentz model was used to parameterize the dielectric functions of ALD TiN thin films measured by SE. The results show the thickness-dependence of the complex dielectric function. For films thicker than 5 nm, the dielectric function resembles that of the bulk material. Below 5 nm, it changes drastically. We compared the film thickness obtained by SE with other characterization techniques (TEM, SEM and XRF) in a wide thickness range. The results show good agreement, indicating reliable applicability of the Drude–Lorentz model to describe TiN optical and electronic properties, and the thickness.

Real-time growth of ALD TiN on thermal SiO_2. Spectroscopic ellipsometry was used to observe the real-time growth of ALD TiN at 350 and 425 ^{o}C, at low process pressures of 2.6–3.2 $\times 10^{-2}$ mbar. Atomic force microscopy (AFM) and electrical test structures were employed to characterize the films. We have demonstrated that the initial growth of ALD TiN follows the Stranski–Krastanov model. Accordingly, the entire growth can be divided into 3 stages: (i) 2D growth of a continuous wetting layer; (ii) 2D-3D transition at a thickness of about 0.69 nm followed by the formation and coalescence of 3D islands; (iii) constant rate ALD growth. Stage (i) is dominantly influenced by the underlying substrate and is temperature-independent. Stage (ii), including the coalescence, is strongly affected by temperature due to its influence on the surface nucleation. In stage (iii), the growth stabilizes at a constant growth rate of 0.02 nm/cycle and is temperature-independent. The results indicate that thin continuous TiN films down to sub-nanometer in thickness can be made by ALD on thermally grown SiO_2.

Resistivity of ultra-thin TiN films. The resistivity of TiN films down to 0.65 nm was determined by spectroscopic ellipsometry and electrical test structures. The results obtained from the two techniques show that for films thicker than 4 nm, the resistivity decreases slowly and flattens out with increasing film thickness. Below 4 nm, the resistivity increases steeply with decreasing thickness. We further compared the optically and electrically determined resistivity. For films thicker than 4 nm, the comparison shows good agreement between the two methods. For films thinner than 4 nm, a significant difference is found which increases with decreasing film thickness. We attribute the difference to the scattering effects at interfaces and grain boundaries for the electrical test structures, which cannot be fully taken into account by SE.

Temperature coefficient of resistance (TCR) of ultra-thin TiN films. The TCR of TiN films down to 0.65 nm in thickness was determined by electrical measurements in the temperature range 25–150 ^{o}C. For films thicker than 2.5 nm, the electrical resistance increases linearly with temperature. A TCR of 3.6×10^{-4} K^{-1} is obtained for an 8.3 nm film. At a thickness of about 2.5 nm, the resistance is nearly unchanged with temperature implying a virtually zero TCR. Below 2.5 nm, the resistance decreases linearly with increasing temperature (i.e. negative TCR). A TCR of -2.54×10^{-3} K^{-1} is obtained for a 0.65 nm film. We ascribe this effect to the metal–semimetal transition occurring at about 2.5 nm, which is mainly attributed to oxygen in the first monolayer. The MST is further supported by our results on the field effect.

Electric field effect in ultra-thin TiN films. We have observed the field effect for films in both metallic (TiN thicker than 2.5 nm) and semimetallic (TiN thinner than 2.2 nm) states. In the metallic state, the field effect is small (i.e. 0.069 % for a 2.5 nm TiN film and smaller for thicker films). This is attributed to possible changes in carrier concentration, effective film thickness, and electron mobility.

In the semimetallic state, a large (and temperature-independent) field effect is observed. It increases drastically with decreasing film thickness and reached 22% for a 0.65 nm thick TiN in the gate voltage range (–50; 50) V. We qualitatively attribute this field effect to the change of carrier concentration and carrier types in the films which accordingly shifts the Fermi level with respect to the band edges. The observed temperature-independence of the field effect indicated no thermal activation of the conduction and additionally confirmed the formation of continuous TiN films from the very beginning of the ALD process.

Impact of native oxidation on electrical properties of TiN films. The influence of native oxidation on electrical properties of thin TiN films was examined. For films thinner than 5 nm, this oxidation changes the *I-V* characteristics from linear to nonlinear. The oxidation causes the aging effect and irreversible degradation of TiN. The native oxidation does not influence the ohmic behavior of the films thicker than 5 nm. The need of applying a suitable passivation layer (amorphous silicon appeared to be the best choice) is demonstrated. The passivation has no influence on the electrical properties of underlying TiN.

Real-time dry oxidation of TiN films at elevated temperatures. Based on the XPS analyses for a partially oxidized TiN film, the existence of an intermixed state between the oxide and nitride layers is concluded. By *in situ* SE, applying a three-layer model, we have observed the real-time oxidation behavior of 15 nm and 5 nm TiN films in oxygen ambient in the temperature range 325–425 ^{o}C. The oxidation of the 15 nm TiN is described as a four-stage process: (1) surface oxidation, (2) diffusion of oxygen along grain boundaries and lateral oxidation and sharpening the grains, (3) rapid oxidation of the sharp grains, and (4) diffusion controlled oxidation. In the oxidation of 5 nm films, stages 1 and 2 coincide, followed by stage 3.

Hot-wire generated atomic hydrogen and its impact on ALD. We have confirmed the successful generation of atomic hydrogen from the dissociation of hydrogen on a hot W filament and the ability to introduce it in short pulses. This is demonstrated by a series of the experiments on etching of Te films. We have investigated the influence of experimental conditions (i.e. filament temperature, substrate temperature and reactor pressure) on the etch rate.

The generated atomic hydrogen was utilized for further investigation of the surface reactions in $TiCl_4/NH_3$ precursor system. Atomic hydrogen was introduced in pulses, additionally to $TiCl_4$ and NH_3, with different pulse sequences. For the $TiCl_4/NH_3/H$ sequence, there is no influence on the growth process compared to the ALD without H-pulses. For the $TiCl_4/H/NH_3$ pulse sequence, the growth rate decreases from 0.02 nm/cycle to 0.01 nm/cycle and the oxygen content increases from 3–5 at% to 30–35 at%. This is attributed to the reduction of chlorine terminations at the surface by atomic hydrogen and the formation of a chemically reactive surface. Only $TiCl_4/H$ pulses result in no growth after the formation of approximately one monolayer. Similar effect occurs when introducing NH_3 via the hot filament, pointing to the decomposition of NH_3 and the formation of atomic hydrogen by the hot filament.

7.2. Recommendations

Based on the results of this study we can now examine the films for the targeted potential applications in nano-crystalline non-volatile memories (NCNV), physical unclonable functions (PUF) and field effect devices.

The applications in NCNV memories require discontinuous films containing discrete islands. Films just above their percolation threshold are favorable for PUF applications. However, we have observed the formation of *continuous* TiN films on thermal SiO_2 from the very beginning of the ALD process. For the first three monolayers of TiN, the growth is mostly in 2D mode (lateral) and no discrete islands can be formed. The island formation starts at the later stage where the growth transforms from the 2D to 3D regime. The existence of the initial continuous monolayers rules out the applications in NCNV memories and PUF devices, at least for the combination of the conditions and the materials studied. We recommend exploring other dielectric substrates and other deposition parameters (gas pressure, temperature, precursor) to influence the continuity of the first monolayers of TiN.

In opposite, the applications in field effect devices require atomically thin continuous films since the electric field can be screened at extremely short distances. In this light, the initial 2D growth regime is favorable. Our experiments on the electric field effect in ultra-thin TiN films demonstrate promising results. A possible explanation is given, suggesting the metal-semimetal transition. However, the mechanism behind this is not fully understood. We recommend to continue this study, focusing on the band structure, interface state, and quantum confinement effects in ultra-thin TiN films as well as to explore field effect in other metallic materials.

In Chapter 6, we have demonstrated that atomic hydrogen can be successfully generated and introduced in pulses suitable for ALD. We recommend further exploring the role of atomic hydrogen as a reducing agent in ALD processes, for deposition of a number of selected materials. We additionally recommend looking into specific interactions between atomic hydrogen and other materials, for example for substrate etching or cleaning purposes.

Summary

During the last several decades, titanium nitride (TiN) has gained much interest because of its low resistivity, chemical inertness and compatibility with complementary metal-oxide-semiconductor (CMOS) technology. Thin films of TiN are commonly used as diffusion barrier and gate material for CMOS devices. Mostly sputtering and chemical vapor deposition (CVD) techniques were employed to deposit the TiN films. However, to achieve thin conformal films with accurate thickness control and excellent step coverage, atomic layer deposition (ALD) has become an ideal choice for making such high quality films in the thickness range of a few tens of nanometers.

In this work, the growth mechanism and electrical properties of ALD TiN films are investigated. The films are grown on SiO_2 substrate using the $TiCl_4/NH_3$ chemistry in the pressure range of $2.6-3.2 \times 10^{-2}$ mbar and temperature range of $350-425$ ^{o}C. The growth of the films is monitored by *in situ* spectroscopic ellipsometry (SE). The films are characterized by other complementary analysis techniques, including atomic force microscopy (AFM), high-resolution scanning/transmission electron microscopy (HR-SEM/TEM), X-ray fluorescence (XRF) and X-ray photoluminescence spectroscopy (XPS). We fabricated test structures to characterize electrical properties of the thin films. The main results of this research are presented in this thesis.

In Chapter 2, the application of SE in studying the optical functions and measuring film thickness of TiN thin films is presented. We apply the Drude–Lorentz model to parameterize the dielectric functions of TiN. The film thickness obtained by SE is compared with the results obtained from HR-TEM/SEM and XRF measurements. The results show good agreement in a wide thickness range (up to 40 nm), indicating the reliable applicability of the SE technique and the Drude–Lorentz model. SE is employed to *in situ* study the growth (Chapter 3), the resistivity (Chapter 4) and the real-time oxidation of ALD TiN films (Chapter 5).

In Chapter 3, the growth mechanism of ALD TiN films on SiO_2 substrate is investigated. We have observed that the growth obeys Stranski–Krastanov model. The growth starts with a 2D mode (continuous layers) followed by a 2D-3D transition (onset of islanding). This transition is temperature independent and occurs at a film thickness of about 0.7 nm. This equals 3 monolayers of TiN. The growth of the 3D islands (on the continuous layers) eventually leads to their coalescence which occurs at 2.5 nm and 3.5 nm for the growth at 350 ^{o}C and 425 ^{o}C, respectively. Before the coalescence, new

nuclei are constantly formed during the growth. Hereafter, the film grows with a constant (ALD) growth rate of 0.02 nm/cycle at both temperatures.

In Chapter 4, the resistivity, temperature coefficient of resistance (TCR) and field effect in thin TiN films down to sub-nanometer scale are presented. The resistivity of TiN is determined by both spectroscopic ellipsometry (SE) and electrical test structures. The latter includes circular transfer length method (CTLM) and linear test structures. The results show that the resistivity increases significantly with decreasing film thickness. We compared the resistivity values obtained by the optical and electrical techniques. For films thicker than 4 nm, the values show good agreement. However, for films thinner than 4 nm, much higher values are found from the electrical measurements. This is attributed to the scattering effects at interfaces and grain boundaries that cannot be fully taken into account by the optical measurements. The TCR of TiN is determined from the electrical measurements in temperature range of 25−150 ^{o}C for different film thicknesses (0.65– 8.3 nm). With decreasing film thickness, the TCR values change sign from positive to negative. This change occurs at a thickness of about 2.5 nm. This effect is attributed to the metal-semimetal transition in these films. In the last part of this chapter, the electric field effect in ultra-thin TiN films in the metallic and the semimetallic states is presented. Upon electrical field, a change of the conduction current up to 22% is found for the films in the semimetallic state.

In Chapter 5, the influence of native oxidation on electrical behavior of thin ALD TiN films is reported. For films thinner than 5 nm, this oxidation changes the *I-V* behavior from linear to non-linear. It shows an *aging effect* that causes an irreversible degradation of TiN. The native oxidation does not influence the linearity of the *I-V* characteristics for films thicker than 5 nm. Nevertheless, it reduces the electrical thickness of TiN. The kinetics and mechanism of thermal oxidation in the temperature range of 325−425 ^{o}C of films with a thickness of 5 and 15 nm are intensively studied. The oxidation in oxygen ambient was carried out directly after the TiN deposition in the same reactor (without vacuum break) and *in situ* spectroscopic ellipsometry monitoring was used. The oxidation of the films can be described as a four-stage process: (1) surface oxidation, (2) diffusion of oxygen along grain boundaries and lateral oxidation and sharpening the grains, (3) rapid oxidation of the sharp grains, and (4) diffusion controlled oxidation.

Finally, in Chapter 6, the generation of atomic hydrogen (H) is presented. Atomic hydrogen is made by the dissociation of molecular hydrogen (H_2) upon collision with a tungsten (W) filament kept at a high temperature ($T \approx 1600–1900$ ^{o}C). We have demonstrated the ability to create atomic hydrogen and to introduce it in short pulses by experiments on etching of tellurium (Te) films in the reactor chamber. The generated atomic hydrogen (H) is further utilized to explore its impact on surface reactions in the $TiCl_4/NH_3$ precursor system. Atomic hydrogen is introduced in pulses additionally to $TiCl_4$ and NH_3 with different pulse sequences. The results show that for the $TiCl_4/NH_3/H$ sequence, there is no influence on the process compared to the ALD without H-pulses. The growth rate remains at 0.02 nm/cycle and the oxygen content - at 3–5 at%. For the $TiCl_4/H/NH_3$ pulse sequence, the growth rate decreases to 0.01 nm/cycle and the oxygen content increases to 30–35 at%. This indicates the reduction of Ti-Cl surface groups by H and the creation of very reactive Ti surface. This surface can be easily oxidized by residual gases from the reactor and process gases. $TiCl_4/H$ pulses only result in no growth after the formation of approximately one monolayer.

Samenvatting

De afgelopen decennia is de belangstelling voor titanium nitride (TiN) sterk toegenomen omdat dit materiaal een lage elektrische weerstand en een lage chemische reactiviteit heeft. Het is bovendien geschikt voor de toepassing in geïntegreerde schakelingen (IC's). Dunne lagen van TiN worden hierin gebruikt als diffusie barrière en als metallische gate in metaal-oxide-silicium (MOS) structuren. De depositie van TiN lagen wordt veelal gedaan met sputteren of depositie uit de dampfase (CVD). Teneinde dunne lagen te maken met een goede bedekking en een precieze beheersing van de laagdikte wordt de laatste tijd atomaire laag depositie (ALD) gebruikt. Hiermee worden dunne lagen tot enkele tientallen nanometers met een hoge kwaliteit verkregen.

In dit onderzoek hebben we de vorming en de elektrische eigenschappen van ALD TiN lagen bestudeerd. De lagen zijn gedeponeerd op SiO_2 substraten met een chemie van $TiCl_4$ en NH_3 bij een druk van 2,6–3,2 x 10^{-2} mbar en een temperatuur van 350–425 ^oC. De groei van de lagen is gevolgd met in-situ spectroscopische ellipsometrie (SE). De lagen zijn mede gekarakteriseerd met analysetechnieken als atomic force microscopie (AFM), hoge resolutie elektronen microscopie (HR-TEM/SEM), Röntgen fluorescentie (XRF) en Röntgen fotoluminescentie spectroscopie (XPS). Er zijn teststructuren gemaakt om de elektrische eigenschappen van de dunne lagen te meten. De resultaten van dit onderzoek zijn samengevat in dit proefschrift.

In hoofdstuk 2 wordt de spectroscopische ellipsometrie beschreven om de optische functies van de TiN lagen te bepalen en de laagdikte te kunnen meten. We gebruiken het Drude-Lorentz model om de diëlektrische functies van TiN te verkrijgen. De laagdikte die met deze SE methode is bepaald wordt vergeleken met de resultaten uit HR-TEM/SEM en XRF analyses. Ze vertonen een goede overeenkomst over een groot laagdikte bereik (0,6–40 nm), waarmee de toepasbaarheid van SE en het Drude-Lorentz model is aangetoond. SE is gebruikt voor de in-situ bestudering van de groei (hoofdstuk 3), de elektrische weerstand (hoofdstuk 4) en de oxidatie van de ALD TiN lagen (hoofdstuk 5).

In hoofdstuk 3 wordt het groeimechanisme van ALD TiN lagen op SiO_2 substraten beschreven. De groei voldoet aan het Stranski–Krastanov model. Het begint met een 2D groei (in continue lagen) gevolgd door een 2D-3D overgang (begin van eiland vorming). Deze overgang is onafhankelijk van de depositietemperatuur en vindt plaats bij een laagdikte van 0,7 nm; dat zijn 3 monolagen TiN. De groei van 3D eilanden op de continue laag leidt uiteindelijk tot samenvoeging bij een laagdikte van 2,5 nm of 3,5 nm als de groeitemperatuur 350^{o}C of 425^{o}C is. Vóór deze samenvoeging worden er voortdurend nieuwe kiemen gevormd en uiteindelijk groeit de laag met een constante (ALD) snelheid van 0,02 nm/cyclus voor beide temperaturen.

In hoofdstuk 4 worden de elektrische weerstand, de temperatuurafhankelijkheid van de weerstand en het elektrische veldeffect in de dunne TiN lagen beschreven. De elektrische weerstand is bepaald met SE en uit de elektrische teststructuren. Deze structuren omvatten de cirkelvormige transfer lengte methode (CTLM) en lineaire structuren. De resultaten laten een aanmerkelijk toename van de elektrische weerstand zien met afnemende laagdikte. De waarden van de elektrische weerstand verkregen door middel van SE en de elektrische metingen zijn vergeleken. Er wordt een goede overeenkomst gevonden voor laagdiktes groter dan 4 nm. Voor laagdiktes kleiner dan 4 nm worden veel hogere waarden met de elektrische metingen gevonden. Dit wordt toegeschreven aan verstrooiingseffecten aan grensvlakken en korrelgrenzen. Deze effecten worden niet volledig meegenomen in de SE bepalingen. De temperatuurafhankelijkheid van de weerstand is bepaald in een temperatuurbereik van 25–150 ^{o}C voor laagdiktes van 0,65–8,3 nm. Voor afnemende laagdikte verandert de temperatuurafhankelijkheid van teken: van positief naar negatief. De omslag vindt plaats bij een laagdikte van ongeveer 2,5 nm. Dit wordt toegeschreven aan de metaal – semi-metaal overgang bij die laagdikte. In het laatste deel van dit hoofdstuk wordt het elektrische veldeffect beschreven voor TiN lagen in de metallische – en in de semi-metallische toestand. Bij de aanleg van een elektrisch veld is een verandering in de elektrische geleiding tot 22% waargenomen in dunne lagen in de semi-metallische toestand.

In hoofdstuk 5 wordt de invloed van de natuurlijke oxidatie van TiN lagen op het elektrische gedrag beschreven. Deze oxidatie verandert de stroom-spanning (I-V) karakteristiek van lineair naar niet-lineair voor de lagen dunner dan 5 nm. Er treedt dan een verloop op dat een onomkeerbare ontaarding van de TiN laag inluidt. Dit effect treedt niet op voor lagen dikker dan 5 nm, maar de elektrische laagdikte neemt dan wel af. De kinetiek en het mechanisme van de oxidatie van 5 en 15 nm lagen in een temperatuurbereik van 325– 425 ^{o}C is uitgebreid bestudeerd. Deze oxidatie in zuurstof is uitgevoerd direct na de depositie in dezelfde reactorkamer. Het is gevolgd met in-situ SE. De oxidatie van de lagen kan worden beschreven met vier stadia: (1) de oxidatie van het oppervlak, (2) de versnelde diffusie van zuurstof langs korrelgrenzen met zijwaartse oxidatie en de vorming van spits toelopende korrels, (3) de snelle oxidatie van deze korrels en (4) de diffusie bepaalde oxidatie.

Tenslotte wordt in hoofdstuk 6 de vorming van atomaire waterstof (H) beschreven door de ontleding van moleculaire waterstof (H_2) aan een hete wolfraamdraad bij een temperatuur van 1600–1900 ^{o}C. De vorming van H en het doseren in korte pulsen is aangetoond met het etsen van tellurium lagen in de reactorkamer. Dit atomaire waterstof is vervolgens gebruikt om de invloed ervan op de oppervlaktereacties van $TiCl_4$ en NH_3 te onderzoeken. Het atomaire waterstof is in verschillende puls-volgordes toegevoegd aan $TiCl_4$ en NH_3 pulsen. Er is geen invloed te zien van een H puls na de opeenvolgende $TiCl_4$ en NH_3 pulsen. Een H dosering na de $TiCl_4$ puls (voor NH_3) geeft een halvering van de depositiesnelheid van de TiN laag. Bovendien wordt een hoog zuurstofgehalte (30–35 at%) in deze laag gevonden. De reductie van $TiCl_4$ door atomaire waterstof is in dit experiment bevestigd. Dit resulteert in een zeer reactief Ti-bevattend oppervlak dat gemakkelijk geoxideerd wordt door oxiderende restgassen in de reactorkamer en de procesgassen. Een puls-volgorde van alleen $TiCl_4$ en H levert geen groei van een laag op.

List of publications

Journal publications related to this work

1. **H. Van Bui**, A.Y. Kovalgin, and R.A.M. Wolters, "Growth of sub-nanometer thin continuous TiN films by atomic layer deposition", *ECS J. Solid State Sci. Technol.* 1, P285-P290, (2012) ***(Chapter 3)***.
   DOI: http://dx.doi.org/10.1149/2.020206jss.
2. **H. Van Bui**, A.Y. Kovalgin, and R.A.M. Wolters, "On the difference between optically and electrically determined resistivity of ultrathin TiN films", Article in Press, *Appl. Surf. Sci.* (2012) ***(Chapter 2&4)***.
   DOI: http://dx.doi.org/10.1016/j.apsusc.2012.09.074.
3. **H. Van Bui**, A.A.I. Aarnink, A.Y. Kovalgin, and R.A.M. Wolters, "Ultra-thin atomic layer deposited TiN films: non-linear I-V behavior and the importance of surface passivation", *J. Nanosci. Nanotechnol.* 11, 8120–8125 (2011) ***(Chapter 4)***.
   DOI: http://dx.doi.org/10.1166/jnn.2011.5069.
4. **H. Van Bui**, A.W. Groenland, A.A.I. Aarnink, R.A.M. Wolters, J. Schmitz, and A.Y. Kovalgin, "Growth kinetics and oxidation mechanism of ALD TiN thin films monitored by *in situ* spectroscopic ellipsometry", *J. Electrochem. Soc.* 158, H214-220 (2011) ***(Chapter 5)***.
   DOI: http://dx.doi.org/10.1149/1.3530090.
5. **H. Van Bui**, A.Y. Kovalgin, A.A.I. Aarnink, and R.A.M. Wolters, "Hot-wire generated atomic hydrogen and its impact on thermal ALD in TiCl4/NH3 system", submitted to *ECS J. Solid State Sci. Technol.* in November, revised in December 2012 ***(Chapter 6)***.
6. **H. Van Bui**, A.Y. Kovalgin, J. Schmitz, and R.A.M. Wolters, "Electrical properties of ALD TiN films down to sub-nanometer scale", to be submitted ***(Chapter 4)***.

Other publications

7. **Bui Van Hao**, Pham Thanh Huy, Tran Ngoc Khiem, Nguyen Thi Thanh Ngan and Pham Hong Duong, "Synthesis of Y_2O_3:Eu^{3+} micro- and nanophosphors by sol-gel process", *J. Phys.: Conf. Ser.* 187, 012074 (2009).

8. **H. Van Bui**, A.Y. Kovalgin, A.A.I. Aarnink, and R.A.M. Wolters, "Atomic layer deposition of aluminum carbide using hot-wire generated atomic hydrogen and trimethylaluminum", in preparation.

Conference presentations

1. **The 12th International Conference on Atomic Layer Deposition**, June 17-20, 2012, Dresden, Germany, *Oral presentation*.
2. **Progress in Applied Surface, Interface and Thin Film Science**, May 14-19, 2012, Florence, Italy, *Poster presentation*.
3. **Annual Conference on Thin Film Nanomanufacturing** (TFN Conference), December 15, 2011, Delft, The Netherlands, *Oral and Poster presentations.*
4. **ITC.OPEN Conference**, November 14-15, 2011, Veldhoven, The Netherlands, *Oral presentation*.
5. **EuroCVD 18 Conference**, September 4-9, 2011, Kinsale, Cork, Ireland, *Poster presentation*.
6. **Annual Conference on Thin Film Nanomanufacturing** (TFN Conference), December 7, 2010, FOM Rijhuizen, Nieuwegein, The Netherlands, *Oral presentation*.
7. **The Annual Workshop on Semiconductor Advances for Future Electronics and Sensors at STW.ICT Conference**, November 18-19, 2010, Veldhoven, The Netherlands, *Poster presentation.*
8. **The Annual Workshop on Semiconductor Advances for Future Electronics and Sensors**, November 26-27, 2009, Veldhoven, The Netherlands, *Poster presentation*.
9. **Annual Conference on Thin Film Nanomanufacturing** (TFN Conference), November 25, 2009, Veldhoven, The Netherlands, *Oral presentation.*
10. **The 9th International Conference on Atomic Layer Deposition**, July 19-22, 2009, Monterey, California, USA, *Oral presentation*.
11. **The APCTP-ASEAN Workshop on Advanced Materials Science and Nanotechnology**, September 15-21, 2008, Nha Trang, Vietnam, *Oral presentation*.
12. **The 5th National Conference on Optics and Spectroscopy and International Workshop on Photonics and Applications**, September 10-14, 2008, Nha Trang, Vietnam, *Oral presentation.*

Acknowledgements

With great pleasure, I would like to send my acknowledgements to those who have helped and supported me throughout my PhD study.

First and foremost, I would like to express my sincere gratitude to Professor Jurriaan Schmitz for accepting me as a PhD student, giving me great opportunities to do research at Semiconductor Components (SC) group. Jurriaan, thank you very much for your kind support, advices and encouragement during the last four years. I specially thank you for your great English when you talk to me: slowly, clearly and intelligibly. This has helped me to overcome the difficulties in communication and to improve my English. Thanks to your words of encouragement and corrections I have become more confident. Nevertheless, I always lose it when I talk to you. That pushes me to go further for the improvement.

I gratefully acknowledge Professor Rob Wolters for being my promoter, and for his immense knowledge, thoughtful guidance, relaxed demeanor and warm encouragement. Rob, it is really hard for me to say thanks to you because it can never end. However, I would like to send you my heartiest acknowledgements. Firstly, I am thankful for your patience with me and my English. I forgot how it was going with our first discussions, but I guess there was quite a lot of misunderstanding. It could be the fact that I always replied *YES* when you asked me, and you were so confused to say *YES* or *NO* when I asked. Fortunately, we only met at most once a week! However, as time went by, our communication went better and better and I started to understand you without your further explanation. Without your consistent encouragement and patience, I would not be able to go further with my PhD. Secondly, I would like to thank you for guiding me towards the right direction in doing experiments, analyzing, interpreting and publishing the results. I realize that following your and Alexey's suggestions is really the easiest way and the short-cut to reach the final destination, and to see the difference between the *line* and the *curve*. Lastly, thank you very much for your intensive reading, your comments and corrections during the last some months on this thesis. Without your help, I would not be able to finish the work in time.

I will forever be thankful to my daily supervisor and my assistant promoter, Dr. Alexey Kovalgin, for the continuous scientific support and guidance of my PhD research, for his patience, motivation, enthusiasm, and concern. Alexey, working with you has been a great pleasure to me. As a PhD student, I have got all what I need from you. In addition, your hobby of drinking tea gives me great opportunities to discuss with you frequently and to keep the work going continuously. Thank you very much for

having spent enormous time guiding me during the last for years, for the open discussions, for your critical reading and comments on the manuscripts and thesis, and for improving my scientific writing skill. Furthermore, I would like to thank you for giving me the opportunity to work with you in the next project.

I would like to acknowledge my dear (former and present) colleagues at SC group. First of all, I am thankful to Annemiek for the help with organizing all kinds of paper work throughout my PhD and for creating excellent working atmosphere. I am also thankful to Remke for the help in the last some months of my PhD. Ray and Cora are acknowledged for helping me to find the good answers for many questions, especially regarding spectroscopic ellipsometry and field effect measurements, and for encouraging me after every presentation I gave at SC. I am also thankful to Sander for the help with the measurement setups and solving computer problems. My special thanks are to Tom (TOM). Tom, thank you so much for your technical supports, for your help, and for your advices and concern in both scientific and personal life from the beginning when I was still in Vietnam until now. I am thankful to my officemates in Hogekamp: Arjen, Balaji and Bijoy for helping me to overcome the difficulties in communication, especially to Bijoy for improving my English vocabulary and grammar. I would like to thank to my officemates in Carré for their willingness to help me and for all the fun we have had: Alessandro, Boni, Balaji (again) Buket, Giulia, Jiahui, and Sumy. Special thanks to Kazmi for helping me with the SEM measurements; to Tom (tom) for helping me with improving my English pronunciation, for the translation of all kinds of Dutch letters and for being a paranymph of my defense. I owe my deepest gratitude to Vidhu for being a wonderful friend and for the kindest help throughout my PhD, and especially for being my good English teacher. I would like to extend my thanks to my latest and former colleagues: Marcin, Pietro, Deepu, Alfons, Jiwu, Jan-Laurens, Victor, Natalie, Mark, Rodolf, and Erik. Special thanks to Joost for helping me with the Dutch documents and to Ihor for guiding me the first *in situ* spectroscopic ellipsometry measurements and the a-Si deposition.

Besides my supervisors, I would like to acknowledge the other members of my promotion committee: Professor Guido Janssen (Technical University of Delft); special thanks to Professor Hans Hilgenkamp (UT) and Dr. Wim Besling (NXP Semiconductors) for the fruitful discussions on the field effect and on the growth characteristics of ALD TiN, respectively. I gratefully acknowledge Professor Dirk Gravesteijn for his critical reading, insightful comments and corrections to strengthen my thesis.

I take this opportunity to sincerely acknowledge some special individuals at MESA+ for the technical supports and training: Hans Mertens (sputtering), Gerard Kip (XPS and SEM), Peter Linders (mask fabrication), Rene Wolf (vacuum systems and dicing), Robert Wijn (oxidation), Mark Smithers (HR-SEM), Eddy Ruiter (XRD), Ton Jenneboer and Huib van Vossen (MTE), Peter Scheeren (cluster system) and Dr. Gregor Hlawacek (HIM). I would like to thank to Prof. Wilfred van der Wiel and Dr. Elia Strambini for the help and the nice discussions on the low temperature measurements. I am also thankful to Dr. Michel de Jong and Gerard Roelofs for giving me the opportunities to continue working here in the next two years.

I would like to thank my Vietnamese friends in Twente. First and foremost, I am thankful to Dr. Minh Nguyen for the kindest help with the *hot* AFM and XRD measurements. Whenever I needed either an AFM or an XRD measurement, I could always get it done within a day. Apart from that, he is also my friend, and my *older brother* who has helped me a lot in my scientific and my daily life. Thanks to Chi Giang for picking up and taking good care of my daughter when I cannot come to pick her up in time. I am deeply indebted to Dao-Tan (the other paranymph), Lan Anh-Hanh and Hieu-Tuan and Duc families for taking good care of my daughter when I am busy, and for the delicious foods, BBQs, and a lot of fun we have had. Thanks to my (*eating*) friend So for the *unconditional support*, for helping me with the mask design of my test structures, for the delicious foods, cakes, and for sharing me all the good news as well as not-good news. Thanks to my ex-housemate, Son, for the wonderful time we had; to Nhi, Chau, and Huong for the delicious foods and cakes. Many thanks to Anh Ha-Chi Hanh and Anh Hien for the very first real dinner I had in the Netherlands, for the advices and encouragements in the beginning of my PhD. Thanks to all other Vietnamese friends in Twente for the warm friendship, the help and the enjoyable parties we have had: Phong, Tuan, Trang, Hieu, Viet Anh, Quyen, Hang, Tuan, Bach, Tram, Yen, Ly, Dung, Giang, Van, Hanh, Tri, Duc.

I would like to extend my thanks to other Vietnamese friends in the Netherlands and in Europe for the kind help, and for either visiting or hosting me or both in the last four years: Tam-Thuan (Groningen), Ha-An, Dung (Delft), Ha, Bay, Vinh, Chinh (Amsterdam), Ngan-Trung (Leuven), Trung-Hai (Bonn), Hien (Koelon), Thuong (Rome), Trinh and Tan (Kaiserslautern), and Nhan (Paris).

I would like to thank my floor-mates and friends from Hogekamp to Carre for the warm friendship during the years. Special thanks to Mark, Fleur, Michiel, Bram, David the delicious foods at the SC dinners; to Imran for the nice words of encouragement.

I am thankful to my previous supervisors, teachers and colleagues at ITIMS, Hanoi University of Technology, and at Faculty of Physics, Quy Nhon University (QNU) for the kindest help and support throughout my PhD. Special thanks to Assoc. Prof. Nguyen Van Hieu (ITIMS) for having recommended me to SC group and to Dr.

Nguyen Thi Minh Phuong (QNU) for the continuous help, guidance and encouragement since I was a student.

I would like to express my deepest gratitude to big-family members: my grandmothers, my uncles, my aunts and especially my parents, Bùi Thái Hùng and Đỗ Thị Mỹ Dung, and my parents in law, Lê Văn Huấn and Võ Thị Mai, for their endless love, encouragement and support.

Kính gửi ba má,

Con xin cảm ơn ba má đã yêu thương, chăm sóc và động viên con trong suốt thời gian qua. Bốn năm là khoảng thời gian con xa ba má dài nhất và cũng làm cho ba má lo lắng nhiều nhất. Tuy nhiên, đó cũng là khoảng thời gian con đã học được nhiều hơn, đã trưởng thành hơn và đã mang lại cho ba má thêm niềm tự hào về sự thành đạt của con. Với tất cả sự yêu thương và kính trọng, con xin kính tặng ba má tất cả những dòng chữ con viết trong quyển luận án này.

For more than four years being in the Netherlands, I have missed the many important life events of my family members, specially the weddings of my sisters and sisters in law. I have not drunk a cup of wine with my brothers in law; I have not seen the smiles of my newly born nieces and nephews, or heard them crying. Every single word of this thesis is dedicated to them.

Last but not least, I am eternally grateful to my wife, Ngoc Loan, who has been working *behind the scene*, for sharing all the moments we have had, for her faithful love, for her consistent encouragement and her quiet sacrifices. Thanks to my lovely daughter, Phuong Anh, for the endless source of motivation and driving force for me to finish my PhD. It is the greatest and happiest thing I can have in my life when I am with her every day, listening to her speaking from Vietnamese to English, and seeing her growing up day by day. I realized that it was the most difficult time for my wife and my daughter to live far away from me. I love you both so much!

I would like to thank to all of my friends, who I might have forgotten to mention in this thesis.

Enschede, December 2012

Hao Van Bui

Author biography

Hao Van Bui (in western style; in Vietnamese: Bùi Văn Hào) was born on March 7th, 1980 in Phuoc Quang village, Tuy Phuoc district, Binh Dinh province, Vietnam. He received his BSc. degree in Physics at Quy Nhon University, Vietnam in September 2002. After his graduation, he was appointed to work as a teaching assistant at the Faculty of Physics, Quy Nhon University, where he was involved in teaching several courses on mathematical and theoretical physics. In October 2006, he went to Hanoi to study at International Training Institute for Materials Science (ITIMS), Hanoi University of Technology and obtained his MSc. in Materials science in October 2008.

Between November 2008 and November 2012, he was employed by MESA+ Institute for Nanotechnology, chair of Semiconductor Components, University of Twente, the Netherlands, to work on the project *Conductivity control in metallic nanolayers* funded by the Dutch Technology Foundation (STW). In this project, under the supervision of Prof. Rob Wolters and Dr. Alexey Kovalgin, he worked on the fabrication and studied properties of thin titanium nitride films down to sub-nanometer scale made by atomic layer deposition (ALD). This thesis presents the main results obtained from that work.

Since November 2012, he has been working as a researcher at MESA+. His current research interests include the fabrication and characterization of ultra-thin films made by ALD techniques and hot-wire generated atomic hydrogen for ALD applications.

Propositions

Accompanying the thesis

Atomic layer deposition of TiN films: Growth and electrical behavior down to sub-nanometer scale

Hao Van Bui

---

1. The growth mode of ALD TiN on SiO_2 can be Volmer-Weber or Stranski-Krastanov depending on processes on the surface (Satta et al., *J. Appl. Phys.* 92, 7641 (2002), and Chapter 3 of this thesis).

2. Spectroscopic ellipsometry is not suitable for determining the electrical resistivity of ultra-thin TiN films (Chapter 4 of this thesis).

3. Ultra-thin ALD TiN films can exhibit semimetallic behavior (Chapter 4 of this thesis) similar to thin carbon films (K.S. Novoselov et al., *Science* 306, 666 (2004)).

4. The oxidation kinetics of thin ALD TiN films can be studied appropriately by in situ real time monitoring (Chapter 5 of this thesis).

5. The etching of tellurium by atomic hydrogen cannot be fully described by one chemical reaction only (Chapter 6 of this thesis).

6. A real time *in situ* characterization technique can significantly reduce the number of experiments and increase the value.

7. A difficult task can be completed in short time when it meets the deadline, but a piece of work can last for weeks, even months until the deadline is close.

8. For a PhD student, working hard is very important. But having good plans and setting the priorities are more important.

9. Social networks (e.g. Facebook, Twitter) can efficiently waste your time.

10. You will become like the people you associate with.
